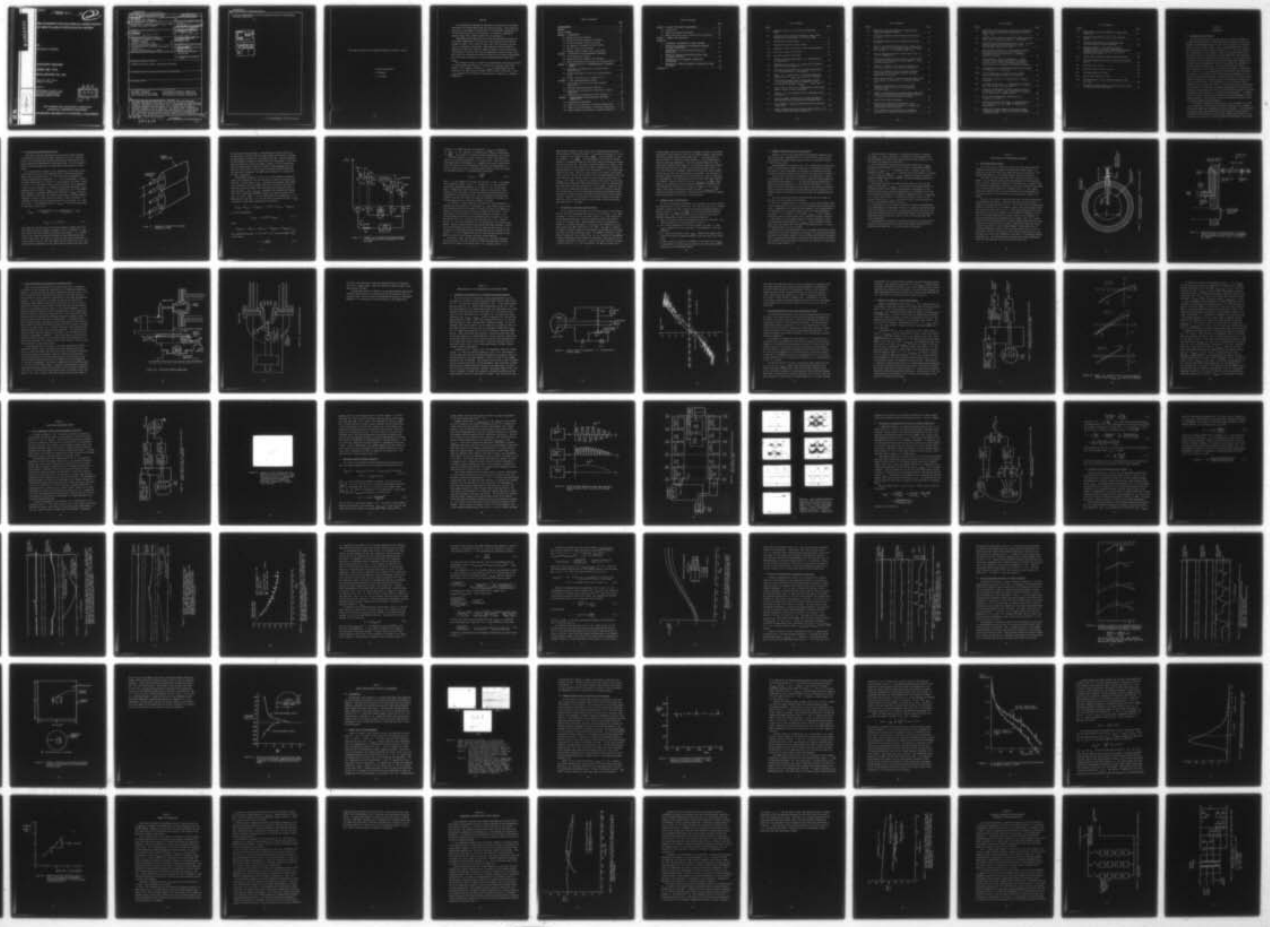
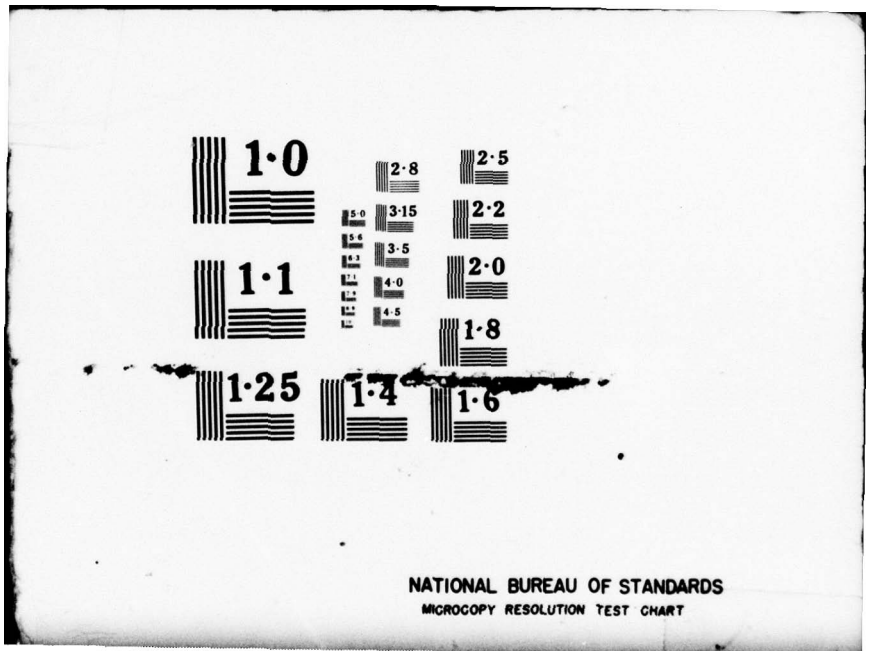
AD-A055 392 STANFORD UNIV CALIF HIGH TEMPERATURE GASDYNAMICS LAB F/G 20/9
MEASUREMENTS OF ELECTRICAL CONDUCTIVITY OF MHD PLASMAS WITH FOU--ETC(U)
FEB 78 N L HOWER F44620-76-C-0024
UNCLASSIFIED HIGL-108 AFOSR-TR-78-0847 NL

1 OF 2
ADA
055392




1·0
1·1
1·25
1·4
1·6
1·8
2·0
2·2
2·5
2·8
3·15
3·5
4·0
4·5
5·0
5·6
NATIONAL BUREAU OF STANDARDS
MICROCOPY RESOLUTION TEST CHART

AD A055392

0847

FOR FURTHER TRAN

MEASUREMENTS OF ELECTRICAL CONDUCTIVITY OF MHD PLASMAS WITH FOUR-PIN PROBES

BY

NELSON L. HOWER

SCIENTIFIC REPORT

FEBRUARY 1978

HTGL REPORT NO. 108

Approved for public release;
distribution unlimited.

Prepared for

AFOSR Contract F44620-76-C-0024
Air Force Office of Scientific Research
Directorate of Aerospace Sciences
Bolling Air Force Base, D.C. 0 20332

DDC
RECEIVED
JUN 19 1978
D

HIGH TEMPERATURE GASDYNAMICS LABORATORY
MECHANICAL ENGINEERING DEPARTMENT

STANFORD UNIVERSITY ■ STANFORD, CALIFORNIA

AD No.

UNCLASSIFIED

SECURITY CLASSIFICATION OF THIS PAGE (When Data Entered)

REPORT DOCUMENTATION PAGE

READ INSTRUCTIONS BEFORE COMPLETING FORM

1. REPORT NUMBER: AFOSR-TR-78-0847
2. GOVT ACCESSION NO.
3. RECIPIENT'S CATALOG NUMBER

4. TITLE (and Subtitle): MEASUREMENTS OF ELECTRICAL CONDUCTIVITY OF MHD PLASMAS WITH FOUR-PIN PROBES.

5. TYPE OF REPORT & PERIOD COVERED: INTERIM rept. 15 FEB 1976 - 14 FEB 1978

6. PERFORMING ORG. REPORT NUMBER: HTGL - 108

7. AUTHOR(s): ~~N. L. HOWER~~ NELSON L. HOWER

8. CONTRACT OR GRANT NUMBER(s): F44620-76-C-0024

9. PERFORMING ORGANIZATION NAME AND ADDRESS
DEPARTMENT OF MECHANICAL ENGINEERING
STANFORD UNIVERSITY
STANFORD, CALIFORNIA 94305

10. PROGRAM ELEMENT, PROJECT, TASK AREA & WORK UNIT NUMBERS: 2308 C1, 61102 F

11. CONTROLLING OFFICE NAME AND ADDRESS
AIR FORCE OFFICE OF SCIENTIFIC RESEARCH/NA
BUILDING 410
BOLLING AIR FORCE BASE, D.C. 20332

12. REPORT DATE: ~~FEB. 15, 1978~~ 15 Feb 78

13. NUMBER OF PAGES: ~~120~~ 131 P.

14. MONITORING AGENCY NAME & ADDRESS (if different from Controlling Office)

15. SECURITY CLASS. (of this report): UNCLASSIFIED

15a. DECLASSIFICATION/DOWNGRADING SCHEDULE

16. DISTRIBUTION STATEMENT (of this Report)

APPROVED FOR PUBLIC RELEASE: DISTRIBUTION UNLIMITED.

17. DISTRIBUTION STATEMENT (of the abstract entered in Block 20, if different from Report)

18. SUPPLEMENTARY NOTES

19. KEY WORDS (Continue on reverse side if necessary and identify by block number)

MHD ENERGY CONVERSION
ELECTRICAL CONDUCTIVITY PROBE
FOUR-PIN PROBE FOR MHD PLASMAS
TIME-RESOLVED ELECTRICAL CONDUCTIVITY
SPACE-RESOLVED ELECTRICAL CONDUCTIVITY
FLUCTUATIONS OF ELECTRICAL CONDUCTIVITY

20. ABSTRACT (Continue on reverse side if necessary and identify by block number)

THIS WORK DESCRIBES THE DEVELOPMENT OF A FOUR-PIN PROBE AND ASSOCIATED ELECTRONIC INSTRUMENTATION FOR MAKING TIME AND SPACE RESOLVED MEASUREMENTS OF ELECTRICAL CONDUCTIVITY IN MHD PLASMA FLOWS. MEASUREMENTS WERE MADE IN 2000°K ATMOSPHERIC-PRESSURE POTASSIUM-SEEDED (0.1% BY WEIGHT) ARGON FLOWING AT VELOCITIES BETWEEN 10 AND 100 METERS/SEC. THE RESULTS SHOW A DEPENDENCE OF INDICATED CONDUCTIVITY ON FLOW SPEED AND PROBE ORIENTATION, SO THAT CALIBRATION IS NECESSARY FOR HIGH ACCURACY ABSOLUTE CONDUCTIVITY DETERMINATIONS. THE PROBE IS WELL SUITED FOR TIME AND SPACE RESOLVED RELATIVE CONDUCTIVITY →

next Page

DD FORM 1 JAN 73 1473 EDITION OF 1 NOV 65 IS OBSOLETE

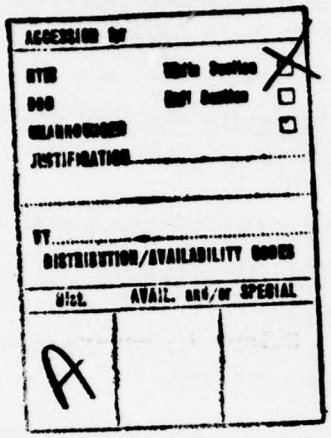
UNCLASSIFIED

SECURITY CLASSIFICATION OF THIS PAGE (When Data Entered)

407078

ha

FLUCTUATION MEASUREMENTS, AND FOR CONTINUOUS DISPLAY OF TIME-AVERAGED INDICATED CONDUCTIVITY.



This report is based on the Engineers Research of Nelson L. Hower.

Research Supervisors

M. Mitchner

C. H. Kruger

Abstract

An instrumentation package was developed for measuring the electrical conductivity of flowing MHD plasmas with four-pin probes. This system was then used to investigate the sensitivity of the indicated conductivity to the flow velocity and the pin orientation in a subsonic, atmospheric-pressure argon flow at 2000 K seeded with 0.1% potassium.

Experimental investigation of the current-voltage characteristics of such probes demonstrated the linearity of the charactistics for applied voltages of about 1 volt across the outer pins, and pointed out the need for a.c. excitation of the probes. When excited at audio frequencies (typically 20 Khz) well above the highest frequencies of the conductivity fluctuations in the flow, the final instrumentation system was found to be well suited for time-resolved relative conductivity fluctuation measurements and for continuous display of the time-averaged indicated conductivity, $\overline{\sigma}_{indic}$.

The absolute accuracy of conductivity measurements using four-pin probes in practical MHD flows appears to be limited by relatively large "flow effects." For example, a decrease in σ_{indic} of approximately 50% was observed as the flow velocity increased from 10 m/sec to 100 m/sec. Also, σ_{indic} decreased as the pins were rotated from the "end-on" to a sidewise orientation.

Table of Contents

	Page
ACKNOWLEDGMENTS	iii
ABSTRACT	iv
LIST OF FIGURES	vii
CHAPTER 1 - INTRODUCTION	1
1.1 Motivation for the Research	1
1.2 Review of Possible Diagnostic Techniques	2
1.3 The Four-Electrode Conductivity Probe	4
1.4 The Question of Accuracy and Flow Effects	9
1.5 Specific Goals of the Research	10
1.6 Summary of What Follows, and of Conclusions	11
CHAPTER 2 - DESCRIPTION OF THE EXPERIMENTAL APPARATUS	13
2.1 Probe Construction Details	13
2.2 Plasma-Production Apparatus and Flow-Path	16
2.3 Mobile Probe Mount and Technique for Varying Velocity	18
CHAPTER 3 - INVESTIGATION OF i-δV CHARACTERISTICS OF FOUR-PIN PROBES	22
3.1 Preliminary Instrumentation for Studying Probe Characteristics	22
3.2 Revised Measurement Circuitry and Instrumentation Setup	25
3.3 Results of Studies of i-δV Characteristics	26
CHAPTER 4 - FINAL SIGNAL-PROCESSING SYSTEM	32
4.1 Use of High-pass Filters and Audio-Frequency Excitation	32
4.2 Remaining Signal-Processing Components	35
4.3 Procedure for Calibrating the Electronics, Using a Dummy Probe	40
4.4 Procedure for Determining the Probe Constant, k_p	42
CHAPTER 5 - INVESTIGATIONS OF FLOW EFFECTS ON INDICATED CONDUCTIVITY	44
5.1 Description of Experiments	44
5.2 Effects of Flow Velocity on Indicated Conductivity	45
5.3 Effects of Pin Orientation on Inducated Conductivity	53
5.4 Spatial Resolution and Effects of Nearby Conductors	55

Table of Contents

		Page
CHAPTER 6 - SAMPLE TIME-RESOLVED MEASUREMENTS.		63
6.1	Introduction	63
6.2	Sample Oscilloscope Photographs.	63
6.3	Sample Statistical Data on Conductivity Fluctuations . . .	65
CHAPTER 7 - SUMMARY AND CONCLUSIONS.		75
APPENDICES		
A	EXPERIMENTAL DETERMINATION OF PROBE CONSTANT	78
B	REDUCTION OF CONDUCTIVITY FLUCTUATIONS INTRODUCED BY ARCJET POWER SOURCE	83
C	DETERMINATION OF THE FLOW VELOCITY ALONG THE NOZZLE AXIS.	91
D	DETAILS OF FOUR-PIN PROBE EXCITATION AND SIGNAL PROCESSING CIRCUITRY	98
E	PRESERVATION OF LOW-FREQUENCY CONDUCTIVITY FLUCTUATIONS	109
F	ESTIMATION OF POSSIBLE DECREASES IN CONDUCTIVITY ALONG THE NOZZLE	112
REFERENCES		119

List of Figures

Figure		Page
1.1	Schematic of the tip of a four-pin conductivity probe.	5
1.2	Schematic of the potential distribution along a line joining the four electrodes of a four-pin probe.	7
2.1	Construction of fixed probes	14
2.2	Construction details of mobile probes.	15
2.3	Schematic of flow train used in 4-pin probe experiment	17
2.4a	Side view of mobile probe mount.	19
2.4b	Top view of mobile probe mount	20
3.1	Initial circuit for generating i-δV characteristics of 4-pin probes.	23
3.2	Reproduction of typical i-δV characteristic obtained with the circuit of Figure 3.1	24
3.3	Electronics configuration for obtaining "high-quality" i-δV characteristics of 4-pin probes.	27
3.4	Sample i-δV characteristics of four-pin probes for several values of $V_{outer,\ max}$, from test of 10/29/76	28
3.5	Illustrating possible error in obtaining true slope of I-δV characteristics as the quotient $I_{max}/\delta V_{max}$ in the presence of non-zero δV_{offset}	31
4.1	Circuit used to study i-δV characteristics while 4-pin probe is driven at audio frequencies	33
4.2	Typical i-δV plot obtained with the measuring circuit of Figure 4.1.	34
4.3	Sketch of sample waveforms at the output terminals of the high-pass filter, rectifier, and low-pass filter	37
4.4	Block diagram of signal processing electroncis used with 4-pin probe.	38
4.5	Sample waveforms obtained at various points (A,B,C, etc.) in signal proce-sing chain of Figure 4.4	39

List of Figures

Figure		Page
4.6	Dummy probe circuitry employed in calibrating the signal processing electronics.	41
5.1	Portion of stripchart record showing Run 300 series of 5/27/77	46
5.2	Portion of stripchart record showing Run 200 series of 5/27/77	47
5.3	Ratio of the indicated conductivity of a mobile 4-pin probe to that of a fixed position probe, as a function of flow velocity u at the mobile probe tip	48
5.4	f(u) vs. u/u_{max} for the mobile probe used 5/27/77 in "end-on" configuration	52
5.5	Portion of Stripchart Record of 6/1/77, showing effects of variation of the probe orientation angle θ on the indicated conductivity	54
5.6	Results of θ-scans of 6/1/77 showing variation of indicated conductivity with angle of orientation, θ . . .	56
5.7	Portion of Stripchart of 6/1/77 showing how mobile probe output is only slightly affected by radial transverses of the probe	57
5.8	Sample radial profile of relative indicated conductivity in the nozzle, as measured by a traversing four-pin probe.	59
5.9	Geometry of modelling of the effects of nearby conductors and insulators with two-dimensional resistance paper	60
5.10	Results of two-dimensional resistance paper study of the effects of nearby conducting and insulating boundaries on indicated conductivity from 4-pin probes.	62
6.1	Sample Oscilloscope Photographs.	64
6.2	Ratio of rms conductivity fluctuations to mean conductivity in arcjet exit nozzle vs. u/u_{max}, from time-resolved 4-pin probe data	66
6.3	Log of spectral density function of conductivity fluctuations vs. frequency from data of 5/2/77	69

List of Figures

Figure		Page
6.4	Probability density function for electrical conductivity, mobile probe in high velocity region Run 102, 5/27/77, $u/u_{max} \simeq 0.94$.	71
6.5	Computed cross correlation coefficient between fixed and mobile probe conductivity signals, vs. delay time.	73
6.6	Separation of fixed and mobile probes, S (cm) vs. delay time for maximum cross correlation coefficient, τ_s (milliseconds), from data of 3/15/77	74
A-1	Probe constant measured in 1 N KCL solution of mobile probe used in test of 3/15/77, before and after platinization of the electrodes, as a function of excitation frequency	79
A-2	Probe constants $k_p(m^{-1})$ as measured in 1 N KCL solution, for the fixed probe (upper curve) and for the mobile probe, before and after use on 5/27/77 (lower curves), as a function of excitation frequency. . .	82
B-1a	Configuration of dc welding power supplies constituting the laboratory d.c. power source	84
B-1b	Circuit diagram for A.O. Smith Co. Model 10000A Welding Power Supply (80 VDC at open circuit).	85
B-2	Connection of Arcject to DC supply used in original experiments.	86
B-3	(a) Setup for measuring L of MHD magnet, (b) Approximate time response of voltage across R	88
B-4	Connection of MHD magnet in series with the arcjet as an inductor to reduce current fluctuations introduced by the laboratory d.c. supply system	89
C-1	Sketch defining geometrical variables in the vicinity of the nozzle	92
C-2	Centerline velocity ratio u/u_{max} vs. axial distance, z, into nozzle from the exit plane, as determined by three methods.	93
C-3	Domain used in AXLAX computer calculations showing streamlines obtained using uniform velocity profiles at entry and exit.	95

List of Figures

Figures		Page
C-4	Experimental setup for determining $u(z)u_{max}$ along nozzle axis	97
D-1	Floating Power Amplifier used to excite four-pin probes.	99
D-2	Floating Signal Generator for providing probe excitation waveform to power amplifier	100
D-3	Schematic drawing of final hookup of Signal Conditioning Unit and external commercial differential amplifiers and filters, to form the electronics configuration of Figure 4.4	101
D-4	Chassis Wiring Diagram of Signal Conditioning Unit.	102
D-5	High Input Impedance Unity-Gain Differential Amplifier Circuit	103
D-6	Low-Pass Filter Circuit	104
D-7	Precision linear rectifier circuit.	105
D-8	Fixed-gain amplifier circuit.	106
D-9	Variable-gain amplifier circuit	107
D-10	Polarity inverter circuit (inverting amplifier with unity gain)	108
E-1	Approximate transfer function of high pass filters used in 4-pin probe signal processing.	111

Chapter 1

INTRODUCTION

1.1 Motivation for the Research

The work described in this report stems from a broader interest in studying how the performance of MHD generators is affected by spatial and temporal nonuniformities which exist, for various reasons and to varying degrees, in all real MHD plasmas. Some of the mechanisms which may produce nonuniformities in the plasma properties (e.g., electrical conductivity, temperature, electron density, velocity) are plasma instabilities, poor mixing, imperfect combustion, and three-dimensional fluid mechanical flow effects such as turbulence and boundary layers. At the present time, an important goal for researchers in the field of MHD power generation is to develop accurate mathematical models for predicting the performance of proposed large-sized generators. As such models grow more refined, it will be necessary that they take into account the presence of nonuniformities in some way, via the parameters which characterize these nonuniformities (such as, for example, statistical measures including mean and rms values of fluctuating conductivity, probability density functions, characteristic frequencies or frequency spectra of fluctuations in plasma properties, and many others). Such information will be required as input information to the theoretical models. For this basic reason, MHD researchers will benefit by being able to measure experimentally the plasma's nonuniform and fluctuating properties, with three-dimensional spatial resolution and adequate time resolution, in laboratory-scale experiments. In summary, there is a need for spatially and temporally resolved measurements of MHD plasma properties to help formulate and provide quantitative input to more accurate performance-predicting models.

Of particular importance in this regard is the development of a diagnostic technique for measuring the electrical conductivity (or, somewhat equivalently under most conditions, the electron density). The desirability of a method having three-dimensional spatial resolution stems from the essentially three-dimensional nature of many plasma nonuniformities, from the near-total lack of any actual published three-dimensional fluctuations

data (e.g., measured values of conductivity fluctuations at, or in a small region surrounding, a point in the flow field) up to the present time, as well as from the need to assess the validity of more traditional optical diagnostics which give only two-dimensional resolution and fail to resolve nonuniformities along the optical path. In addition to spatial resolution, time-resolved measurement techniques are valuable because they permit frequency spectral analyses of fluctuations to be made (which often illuminate the nature and origin of the nonuniformities), and offer the possibility (when coupled with suitable data-processing equipment) of generating any sort of quantitative statistical information which might be required by theoretical models, such as the theory of Reference [1].

1.2 Review of Possible Diagnostic Techniques

Measuring techniques for electrical conductivity or electron density which fulfill the requirements for both three-dimensional spatial resolution and temporal resolution appear, at the present time, to be restricted to probe methods, viz, the four-electrode (conductive type) conductivity probe, the inductive RF probes (several different designs exist), and Langmuir probes. These probes are described in Reference [2] and will be discussed briefly here. First, however, we mention that, while there are standard spectroscopic techniques (such as the absolute continuum intensity method and the absolute line intensity method for N_e) which do provide suitable time response, their spatial resolution is inherently limited to two dimensions. Also, there are laser scattering methods (in particular, Thomson scattering from free electrons for determining N_e) which are capable of 3-D spatial resolution; such techniques are only poorly developed at the present time, however, and for MHD plasmas the time resolution is likely to be inadequate, due to the very low scattering cross sections and consequent long times required for photon counting.

The four-electrode probe (or four-pin probe) is the subject of this report and will be thoroughly described later; it is perhaps the most "direct" technique, in that it is based on actually passing current through the plasma, obtaining measurements of both the current density J and electric field E, and deducing the conductivity σ directly from Ohm's Law, $J = \sigma E$.

The several types of inductive (RF) probes which have been used to measure σ [2,3,4] rely on the fact that the impedance (or Q) of a small RF coil immersed in a plasma, or the trans-impedance between two or more such coils, changes when the conductivity of the surrounding medium changes. The coils are usually enclosed in an insulating ceramic tube and swept through a plasma stream quickly enough to avoid melting. The effects of nearby metallic conductors tend to "swamp out" the effects of the plasma, whose conductivity is orders of magnitude lower; in addition, to interpret the data obtained with these inductive probes requires assumptions about the fluid mechanical perturbations caused by the presence of the probe. These facts tend to limit the accuracy and the spatial resolution of inductive probes, although it appears difficult to characterize this limitation quantitatively.

The electron concentration, N_e, can be determined under MHD conditions by suitably designed and calibrated Langmuir probes. Since $\sigma = e^2 N_e / m_e \bar{\nu}_{eH}$ and the collision frequency $\bar{\nu}_{eH}$ can be calculated fairly accurately if the temperature is known to only modest accuracy, the Langmuir probe N_e measurement together with a rough temperature measurement will yield the electrical conductivity. The theoretical and experimental work of Clements [5] has demonstrated the feasibility of N_e measurements by Langmuir probes operated in the highly negatively-biased ion-collecting mode. However, the theory which relates the calculated N_e to the measured probe bias voltage and collected ion current is only approximate at the present time. Thus, in order to obtain accurate N_e measurements, one will be forced to calibrate the Langmuir probe's response by immersing the probe in plasmas in which N_e is accurately known by some other means. Aside from this difficulty vis-à-vis calibration, the Langmuir probe appears to offer the possibility of excellent spatial and temporal resolution. There are practical problems with such probes, however, among which are the cooling of the probe and the deposition of seed materials or other substances in the flow onto the cold probe.

1.3 The Four-Electrode Conductivity Probe

This report describes experimental work directed towards assessing the suitability of the four-electrode conductivity probe (or "four-pin probe") for three-dimensional spatially-resolved and time-resolved electrical conductivity measurements in MHD plasma flows. In this section we present a brief description of the construction and operation of these probes.

The four-pin probe consists of four exposed metal electrodes in the form of short tips of bare wire emerging from two parallel double-bore ceramic tubes, as shown in Fig. 1.1. The probe tips are immersed in a conducting medium whose conductivity, σ, is to be determined. An external power supply (such as a battery or a more elaborate oscillator) causes a current i to flow between the two outer electrodes, and the magnitude of this current is measured, for example, by measuring the voltage V_{shunt} appearing across a resistor R_{shunt} in series with the outer electrodes. Simultaneously, one measures the potential difference δV_{inner} which appears between the two inner pins; this is done using a very high impedance voltmeter so that no current flows into either of these electrodes. If conditions are such that the probe characteristics are linear, i.e., that the current i and voltage difference δV_{inner} are directly proportional to each other, we may write

$$\delta V_{inner} = \begin{pmatrix}\text{proportionality} \\ \text{constant}\end{pmatrix} (i) \begin{pmatrix}\text{resistivity of} \\ \text{the medium}\end{pmatrix} + \text{const.}$$

or

$$\delta V_{inner} = k_p \, i \left(\frac{1}{\sigma}\right) + C \quad . \tag{1.1}$$

The theoretical justification for this relationship is simply that in an ohmic medium, such as we assume the plasma to be in the absence of a magnetic field, the current density (and hence total current, i) is proportional to the potential difference between two measuring stations (viz, the two inner pins). The reason for using the inner pins (which draw no current) rather than the outer pins (which do draw current) for this potential difference measurement is that plasma sheath voltage drops occur near

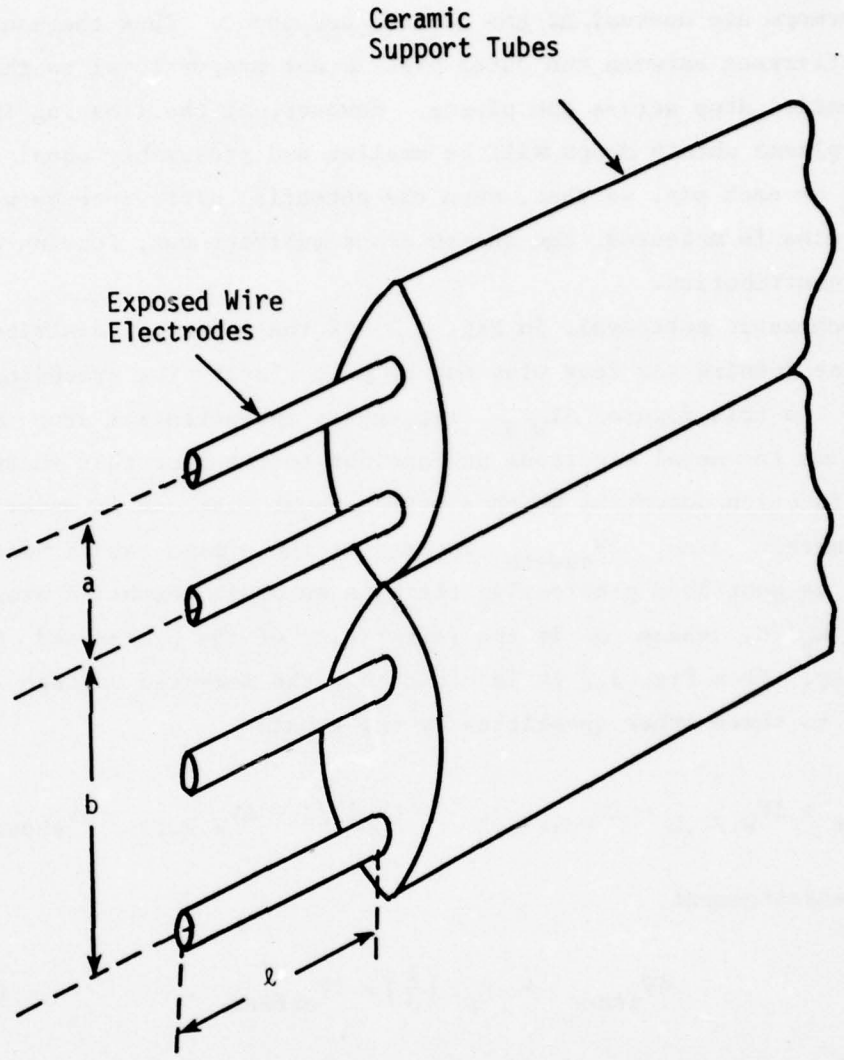


Figure 1.1. Schematic of the tip of a four-pin conductivity probe.

the current-carrying electrodes. The magnitudes of these drops are of the same order or greater than the ohmic voltage drop through the plasma, and furthermore are unequal at the cathode and anode. Thus the measured voltage difference between the outer pins is not proportional to the true ohmic potential drop across the plasma. However, at the floating inner pins, the plasma sheath drops will be smaller and presumably equal (or nearly so) at each pin, so that, when the potential difference between the inner pins is measured, the sheath drops subtract out, leaving only the ohmic contribution.

The schematic portrayal, in Fig. 1.2, of the potential distribution along a line joining the four pins may help to clarify the preceding explanation. In this figure $\Delta V_{W.F.}$ represents the potential drop immediately outside the metal electrode surface due to the fact that there is some work function potential which electrons must overcome in order to leave the metal. Also, ΔV_{sheath} represents the plasma sheath voltage drop, and, as mentioned previously, there is an ohmic potential drop of $k_p \rho i$, or $k_p i/\sigma$, where ρ is the resistivity of the plasma and σ its conductivity. From Fig. 1.2 it is clear that the measured voltage δV_{inner} is related to these other quantities by the equation

$$\delta V_{inner} + \Delta V_{W.F.,2} - \Delta V_{sheath,2} = (k_p i)/\sigma + \Delta V_{W.F.,1} - \Delta V_{sheath,1} ,$$

or, upon rearrangement,

$$\delta V_{inner} = k_p i \left(\frac{1}{\sigma}\right) + \delta V_{offset} , \qquad (1.3)$$

where

$$\delta V_{offset} \equiv (\Delta V_{W.F.,1} - \Delta V_{W.F.,2}) - (\Delta V_{sheath,1} - \Delta V_{sheath,2}) . \qquad (1.4)$$

Now, differentiating Eqn. (1.2) (or Eqn. (1.3)) and rearrangement leads to the result

$$\sigma = k_p \frac{di}{d(\delta V)} , \qquad (1.5)$$

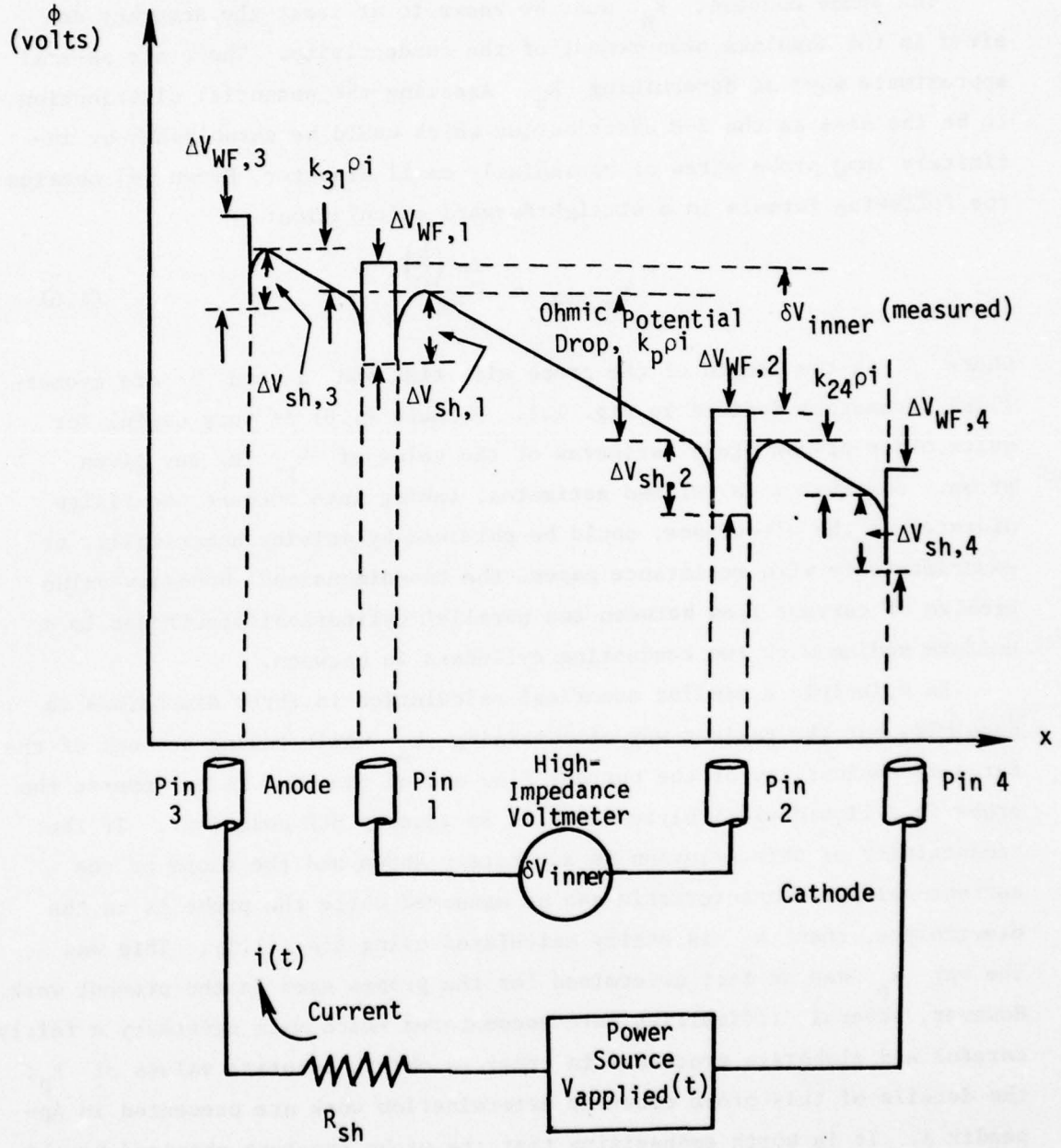


Figure 1.2. Schematic of the potential distribution along a line joining the four electrodes of a four-pin probe.

in which it is understood that for simplicity δV_{inner} is denoted by δV. Since k_p is a constant, the conductivity is directly proportional to $\frac{di}{d(\delta V)}$, the slope of the current-voltage characteristic of the probe.

The probe constant k_p must be known to at least the accuracy desired in the absolute measurement of the conductivity. There are several approximate ways of determining k_p. Assuming the potential distribution to be the same as the 2-D distribution which would be established by infinitely long probe wires of vanishingly small diameter, Brown [6] obtains the following formula in a straightforward calculation:

$$k_{p,2\text{-}D} = \frac{\ell n \left(\frac{b}{a}\right)}{\pi \ell} \tag{1.6}$$

where ℓ is the length of the probe wire tips and a and b are geometrical parameters defined in Fig. 1.1. Formula (1.6) is very useful for quick order-of-magnitude estimates of the value of k_p for any given probe. Somewhat more refined estimates, taking into account the finite diameter of the electrodes, could be obtained by solving numerically, or experimentally with resistance paper, the two-dimensional boundary-value problem of current flow between two parallel cylindrical electrodes in a uniform medium with two conducting cylinders in between.

In principle a similar numerical calculation in three dimensions is possible, but the easiest way of obtaining k_p while taking account of the three-dimensionality of the current flow around the pins is to immerse the probe in a liquid electrolyte (such as an aqueous KCℓ solution). If the conductivity of this solution is accurately known and the slope of the current-voltage characteristic can be measured while the probe is in the electrolyte, then k_p is easily calculated using Eqn. (1.5). This was the way k_p was in fact determined for the probes used in the present work. However, several difficulties were encountered which made necessary a fairly careful and elaborate procedure in order to obtain accurate values of k_p; the details of this probe constant determination work are presented in Appendix A. It is worth emphasizing that the probe constant obtained by this method is valid for non-flowing, stationary conducting media.

In practice, then, once the probe constant k_p has been determined, the conductivity of the test plasma may be found by immersing a four-pin probe into the plasma, exciting the probe (i.e., passing current i at

some suitable frequency) with a power source, simultaneously measuring i and the inner-pin voltage difference δV, suitably processing the i and δV signals so as to obtain the slope $\frac{di}{d(\delta V)}$, and calculating σ from the relation $\sigma = k_p \frac{di}{d(\delta V)}$. The time-response of the probe is limited mainly by the speed with which the electronic signal processing and recording can be carried out. The spatial resolution depends, of course, on the size of the actual probe, which can be made reasonably small (typical dimensions might be 0.5 mm diameter wire electrodes of 2 or 3 mm length separated by, say 1 mm). There is a lower limit to the possible probe dimensions, however, which is due to the fact that the plasma sheaths around the inner and outer pins must not overlap or else erroneous measurements of δV_{inner} will result. In addition, it should be noted that the electrodes may operate at sufficiently high temperatures that they are thermionically emitting without affecting adversely the probe reading. Thermionic emission, in fact, simplifies the operation of the probe by greatly reducing the voltage drops at the electrode-plasma interface and permitting large currents to be passed through the plasma with comparatively small applied voltages. Operation at temperatures of thermionic emission also eliminates the need for elaborate probe-cooling systems, thereby simplifying the construction of the probes.

1.4 The Question of Accuracy and Flow Effects

In the introductory discussion of the four-pin probe in the previous section, the major assumptions have been that (a) the probe's i-δV characteristic is linear, and (b) the probe constant k_p, found empirically in non-flowing electrolyte solutions, remains valid when the probe is placed in a flowing plasma. These assumptions must be experimentally studied if a reliable assessment of the accuracy and suitability of this probe method under MHD conditions is to be made. The range of currents for which the desired linearity holds should be determined, and care taken to operate the probe within this range. The possible influence of "flow effects" arises when one considers that k_p is a function of the complete current distribution pattern around the electrodes. When the probe is in a uniform, stationary electrolyte, a particular current pattern, and hence a certain value for k_p, will be obtained. But when the probe is in a

flowing plasma, there are several effects tending to produce a non-uniform conductivity field around the pins, such as thermal boundary layers around the pins and ceramic support which might lower σ in regions near the cooler surfaces, or convection effects tending (in loose terminology) to "blow the discharge downstream". Such "flow effects" might well lead to significantly altered (with respect to the stationary medium case) current patterns around the pins, and thus to an effective altered value of k_p, or in other words to an indicated conductivity which could differ significantly from the true local conductivity of the plasma. Just how much the indicated conductivity depends on such flow effects is open to experimental investigation. For convenience, the flow effects have been classified into possible "velocity effects", in which $\sigma_{indicated} = k_p \frac{di}{d(\delta V)}$ might change as the magnitude of the flow velocity changes for some particular fixed geometrical orientation of the pins with respect to the velocity vector, and possible "orientation effects" in which $\sigma_{indicated}$ might change as the angular orientation of the probe relative to the flow changes while the magnitude of the velocity remains constant.

1.5 Specific Goals of the Research

In view of the previous discussion, it is possible now to state briefly the specific goals of the present work. The first major goal was to develop a suitable electronics probe excitation and signal-processing package to measure accurately $\sigma_{indic} = k_p \frac{di}{d(\delta V)}$ on both a time-resolved and time-averaged basis. The other main goals are to provide at least partial, hopefully quantitative answers to the following questions.

- What is the range of operating parameters (if any) for which the i-δV characteristics of the four-pin probe is linear?
- For a fixed orientation of the four-pin probe, and fixed σ, does σ_{indic} depend, and if so by how much, on the magnitude of the flow velocity?
- For a fixed flow velocity, does σ_{indic} change as the angular orientation of the pins is changed relative to the flow, and if so, by how much?
- To what accuracy or degree of confidence can one assert that σ_{indic} as measured by a four-pin probe is equal to the true local electrical conductivity in flowing MHD plasmas?

1.6 Summary of What Follows, and of Conclusions

Chapter 2 of this report describes the experimental apparatus other than the electronic instrumentation: the arcjet facility and flow train for generating the seeded argon plasma, as well as construction details of the four-pin probes.

The experiments to investigate the i-δV characteristics of four-pin probes, and establish the range of linearity, are discussed in Chapter 3. The results of these experiments were important in motivating the final electronics signal-processing system, which is the main topic of Chapter 4.

Once the final electronics configuration was implemented, a number of experiments were done using this system to make both time-averaged and time-resolved measurements of σ. The time-averaged measurements were mainly to test the sensitivity of the indicated conductivity to flow effects (velocity and orientation); these results are presented in Chapter 5. Chapter 6 presents some sample time-resolved data and the statistical information about the conductivity fluctuations which was deduced from such data.

The main conclusions which we have drawn about four-pin probes in the course of this research are as follows:

- The i-δV characteristics of the four-pin probes used remained linear if the voltage applied to the outer pins was maintained below approximately 1 volt. Depending on the particular probe geometry, the corresponding current densities at the outer pin surfaces were less than approximately 0.1 amp/cm^2 to 0.2 amp/cm^2. The criterion $V_{outer} \lesssim 1$ volt seemed to be the most practical and reliable rule of thumb for ensuring linearity.
- Even when no current passes between the outer electrodes, a finite and fluctuating voltage difference δV_{offset} appears between the inner pins; this fact requires that the probe not be operated with d.c. current if erroneous results are to be avoided.
- When excited at frequencies well above the highest naturally-occurring conductivity fluctuation frequencies in the flow, the four-pin probe system described in this report appears to yield reliable and accurate time-resolved data on conductivity fluctuations (accurate in the sense that all statistical parameters characterizing the fluctuations are accurate, with the exception of the mean value of σ).

- With the method of immersion in electrolyte solutions to calibrate the probes, k_p can be found only to a precision of approximately 5% to 10% (depending on the probe used), which limits the probe's absolute accuracy even in the absence of flow effects.
- For a fixed probe orientation, the indicated conductivity σ_{indic} decreases as the magnitude of the flow velocity of the plasma increases. The curve of σ_{indic} vs. u presented in Fig. 5.3 shows a drop of approximately 50% in σ_{indic} as u increases from about 10 m/sec to 100 m/sec.
- For a fixed flow velocity, σ_{indic} appears to decrease as the flow direction changes from "end-on" towards a sidewise orientation relative to the pins (cf. Fig. 5.6).
- The present work has not studied possible effects of the size and geometry of the probe on σ_{indic}, but has restricted attention mainly to a particular probe in the "end-on" configuration; nevertheless, it has shown that with careful, detailed measurements it is possible, for any particular probe and orientation, to produce an empirical curve of $\sigma_{indic}/\sigma_{u=o}$ vs. u which can be used as a flow-effect calibration curve, i.e., to provide a correction to σ_{indic} which would yield an accurate measure of the true local conductivity at any velocity.
- In the absence of such detailed flow-effect calibration measurements as are mentioned in the preceding conclusion, it would be unwarranted (based on the data obtained in this work) to claim high absolute accuracy for any particular four-pin probe used in flowing MHD plasmas, since the indicated conductivity may be as much as a factor of two or three lower than the actual conductivity.
- Care should be exercised in interpreting conductivity profile data obtained by four-pin probes (such as some of the results of Brown [6]) in boundary layers where both σ and the velocity are varying.

Chapter 2

DESCRIPTION OF THE EXPERIMENTAL APPARATUS

2.1 Probe Construction Details

All of the four-pin probes used in this work were constructed with tungsten wire electrodes supported by double-bore alumina tubing. No artificial cooling was used, since these materials can survive the NaK-seeded argon plasma at around 2000°K without melting or oxydizing.

There were two basic variations in the actual construction of the probes. In the simplest version, which was employed as a fixed-position probe to monitor conductivity changes in the plenum, the two ceramic tubes were inserted through holes drilled into a brass pipe plug which was screwed into the water-cooled plenum wall, as shown in Fig. 2.1. The tungsten wires were typically 0.020 or 0.030 inch diameter, and the exposed tips were located close to the centerline in the low-velocity region in the plenum.

The other type of probe construction was used for mobile probes which were mounted on a mechanical traversing mechanism situated outside the plenum of the plasma generator facility. The ceramic tubes for these mobile probes were inserted into 5/8" diameter graphite rods appropriately drilled and slotted, as indicated in Fig. 2.2. The alumina tubes were potted into the holes and slots in the graphite with Ceramabond 503 adhesive. In the case of long probes employing thin ceramic tubing, it was necessary to wrap the tubing with thin molybdenum wire, as shown in Fig. 2.2, to keep the two tubes from separating due to thermal warping; some probes were also reinforced by securing 1/16 inch diameter tungsten rods along the outside of the alumina tubes to reduce lateral warping. While liberal use of Ceramabond adhesive was made to hold the tubes together and coat the exposed metal surfaces of the moly wire and tungsten reinforcing rods, care was taken not to place any Ceramabond in the region of the exposed tungsten electrode pins. The exposed pins were cleaned with a dental sandblaster before use, and appeared clean and bright after each test.

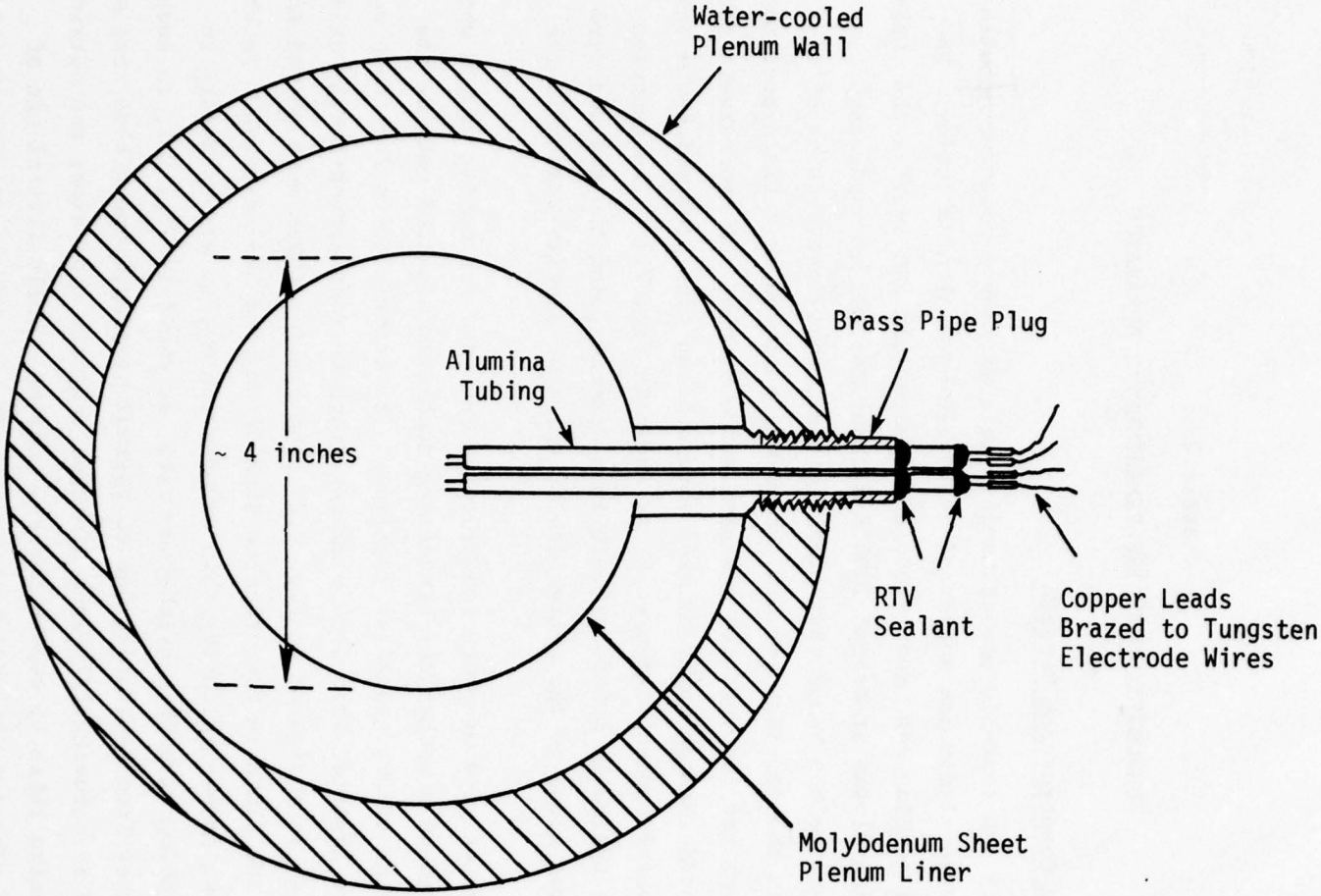


Figure 2.1. Construction of fixed probes. Flow direction is normal to the plane of the page.

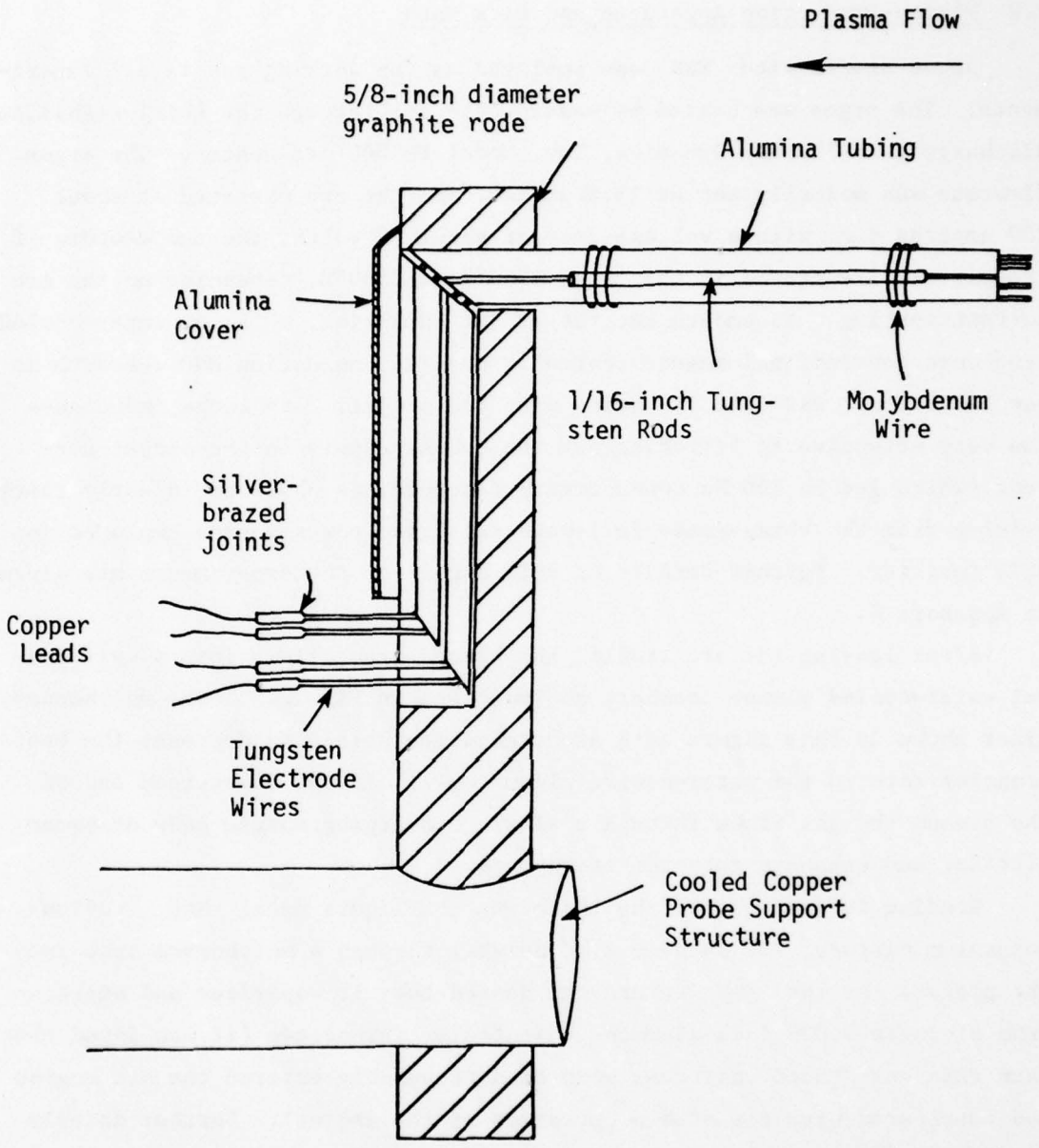


Figure 2.2. Construction details of mobile probes. The alumina tubing was potted into the graphite with Ceramabond 503 high-temperature cement, which is not shown in this sketch.

2.2 Plasma-Production Apparatus and Flow Path

Argon seeded with NaK was employed as the working gas in all experiments. The argon was heated by passing the gas through the swirl-stabilized discharge in a Thermal Dynamics, Inc. Model F-5000 arc heater. The argon flowrate was normally set at 13.6 gm/sec, and the are operated at about 700 amperes d.c. with a voltage drop of about 90 volts; the temperature of the gas usually stayed in the range 1700°K to 2300°K, depending on the arc current setting. To smooth out the arcjet operation, a large, water-cooled, iron-core conventional magnet (normally used in combustion MHD research in our laboratory) was used in series with the arcjet. Its large inductance was very effective in filtering out the 360 Hz ripple in the arcjet current (which led to 360 Hz conductivity fluctuations observed in early tests) arising from the three-phase full-wave rectified power source employed in this facility. Further details of this aspect of the experiments are given in Appendix B.

After leaving the arc itself, the heated argon flows into a cylindrical water-cooled plenum chamber, as indicated in Fig. 2.3. The molybdenum liner shown in this figure acts as a radiation shield to decrease the heat transfer rate to the water-cooled plenum wall. At the downstream end of the plenum the gas flows through a slowly converging nozzle made of boron nitride, and exhausts into the atmosphere.

Seeding is accomplished by injecting the liquid metal NaK (sodium-potassium mixture, 78% potassium by weight) through a molybdenum tube into the plenum. As the NaK enters the heated tube it vaporizes and emerges from a single 0.020 inch diameter hole facing downstream (it was found that when this hole faced upstream, some seed presumably entered the arc region and interfered with the stable operation of the arcjet). Further details on this seed-injection system may be found in Reference [7]. To avoid the condensation of liquid sodium and potassium metal on the boron nitride nozzle walls, a stainless steel insert was placed between the nozzle and the cooled copper end flange. This insert was designed with large thermal resistance and allowed the nozzle to run at temperatures above 1000°K, thus avoiding NaK condensation.

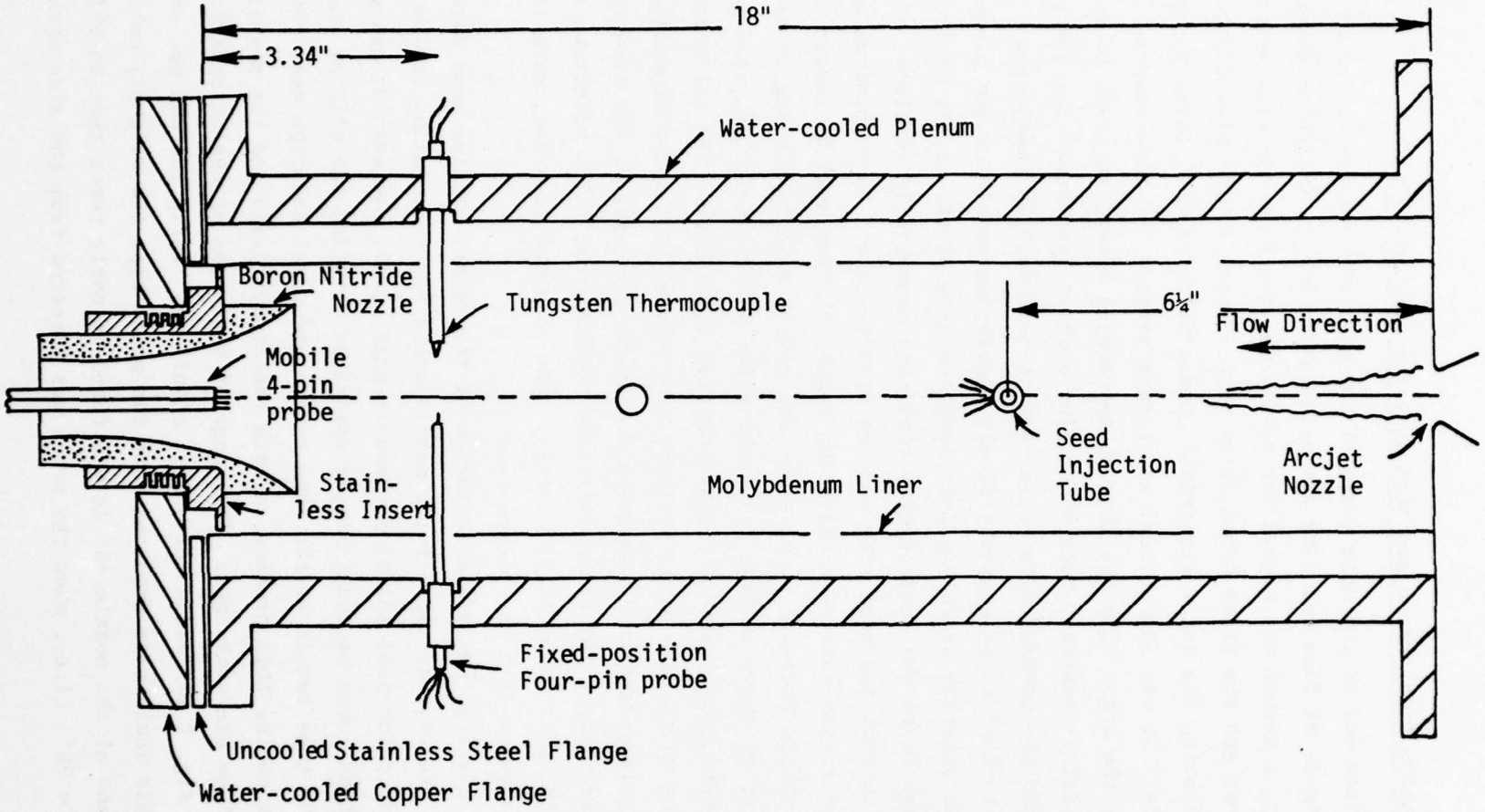


Figure 2.3. Schematic of flow train used in 4-pin probe experiments.

2.3 Mobile Probe Mount and Technique for Varying Velocity

Since one of the main goals of the present work was to investigate the effects of flow velocity and orientation on the indicated conductivity reading, a method was needed for easily varying both the flow velocity over the probe and the probe orientation with respect to the flow direction, while leaving the local electrical conductivity of the plasma approximately constant. It was impractical to attempt varying the flow velocity by varying the argon flowrate through the arcjet since, in order to keep the conductivity constant, both the arcjet current (and hence the gas temperature) and the seeding rate would have to be carefully readjusted. It was therefore decided to employ a slowly converging nozzle at the plenum exit; the flow velocity at each point along the axis of the nozzle would then be different (with the conductivity remaining essentially constant, since the arcjet current and seed rate were in steady state). A mechanical mount was constructed using a translating rotary milling head to insert and withdraw a mobile four-pin probe along the nozzle axis in the region of varying velocity, as shown in Fig. 2.4. The axial position of this probe was monitored continuously with a linear position transducer. The calibration procedure by which this axial position was related to the corresponding flow velocity is discussed in Appendix C. Using this system, the flow velocity varied from about 100 m/sec, with the mobile probe fully withdrawn out to nearly the exit plane of the nozzle, down to about 10 m/sec, with the probe fully inserted into the plenum region.

By placing the axis of rotation of the rotary milling head directly beneath the exposed tips of the mobile probe and translating the probe tips to a point just inside the nozzle exit plane, the angular orientation of the pins could be continuously varied by rotating the milling head. The probe tips remain at the same radial and axial location near the nozzoe exit during this process so both the conductivity and the magnitude of the flow are unchanged. The range of variation of the orientation angle θ (see Fig. 2.4b) was about $\pm 60°$; a full $\pm 90°$ variation was not possible, since this would have required that the probe tips lie slightly outside the exit plane of the nozzle and it was found in early tests that in this case when $\theta = 90°$ (i.e., when the probe was inserted from the side normal to

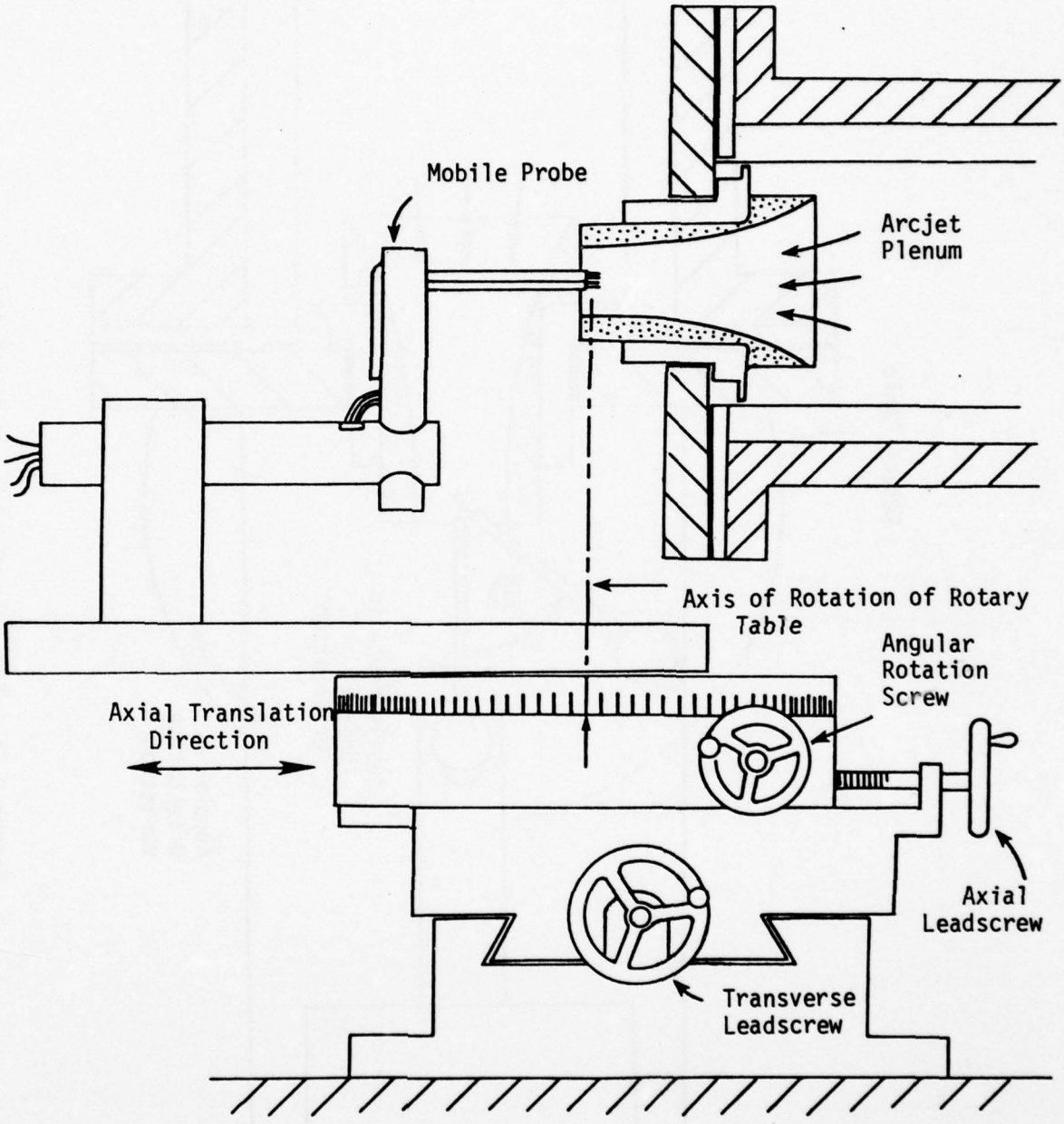


Figure 2.4a. Side view of mobile probe mount.

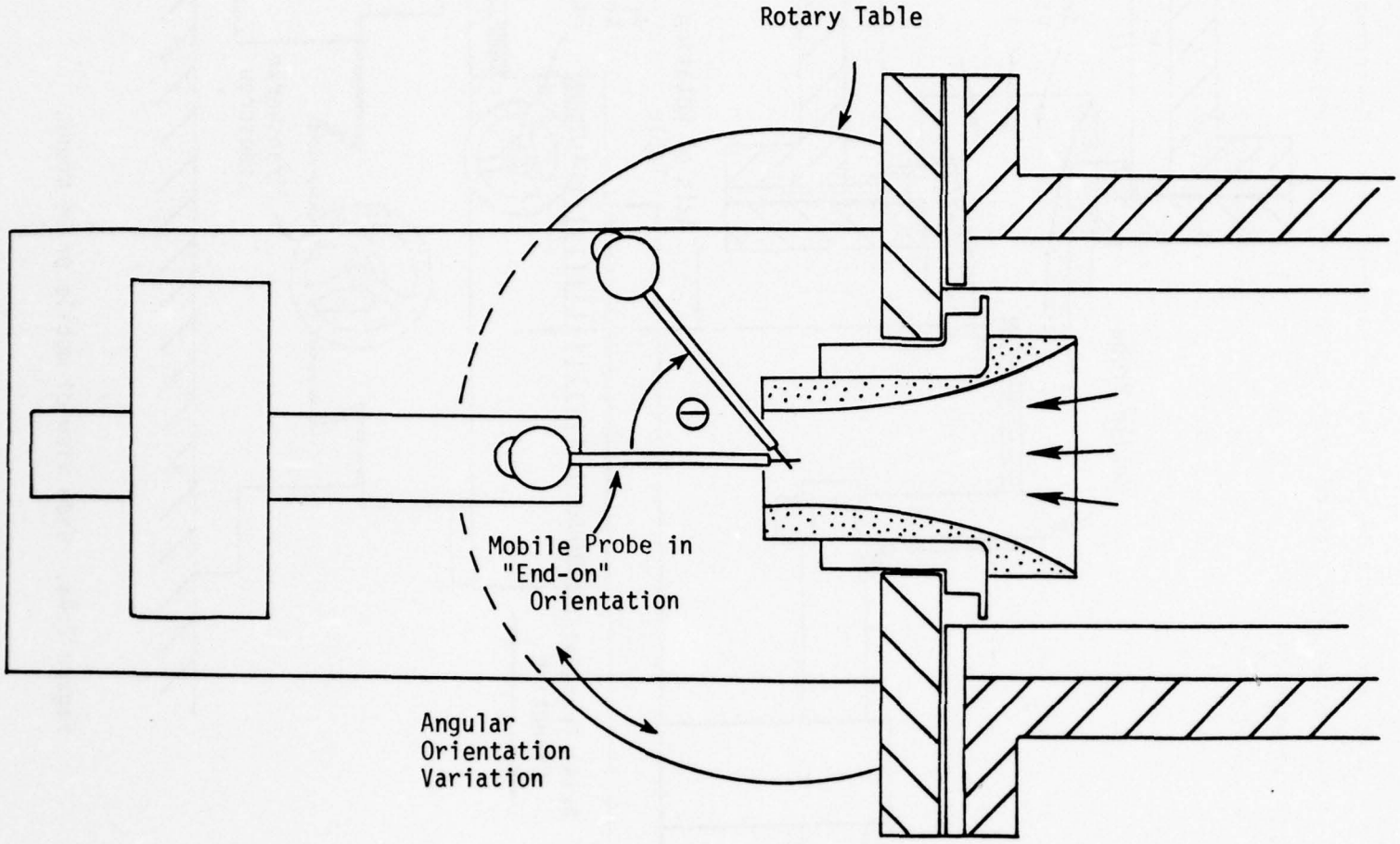


Figure 2.4b. Top view of mobile probe mount.

the flow), some atmospheric oxygen was entrained along the downstream side of the ceramic support tubes and reached the exposed tungsten pins, which quickly oxidized.

An additional degree of freedom in the translating mobile probe mount permitted traversing the probe radially across the stream and into the boundary layers. This was useful in measuring the severity of the radial gradients (or in measuring the radial profiles) of the conductivity.

Chapter 3

INVESTIGATION OF i-δV CHARACTERISTICS OF FOUR-PIN PROBES

3.1 Preliminary Instrumentation for Studying Probe Characteristics

The first system for varying the current passing between the outer electrodes of the probe, and for generating directly plots of this current (i) vs. the inner pin potential difference (δV), is the simple battery-driven circuit and x-y plotter shown schematically in Fig. 3.1. With the probe immersed in the seeded argon plasma, the potentiometer was slowly turned by hand from one extreme to the other over a time period of the order of one or two minutes, and the signals δV, the inner pin voltage difference, and $V_{shunt} = iR_{shunt}$ (used as a measure of the current) were applied directly to the x- and y-axes, respectively of the x-y plotter, whose differential input terminals were floating off ground. (In all experiments with four-pin probes, care was taken not to ground any point in the probe-excitation circuitry, and all instruments to which the V_{shunt} and δV signals were applied had to be true floating, differential-input devices. These precautions were necessary, because the probe pins themselves were immersed in a plasma which was in good electrical contact with the grounded anode of the arcjet facility; thus any other grounded point in the probe power supply would provide a possible alternative path for the probe current, part or all of which might bypass the shunt resistor, causing erroneous measurements.)

A reproduction of a typical i-δV plot obtained in this way is shown in Fig. 3.2. While the general appearance of this i-δV characteristic indicates that the probe is operating approximately as expected, there are several deviations from ideal behavior. First, the trace is very jagged, especially near the extremes. This behavior could be due in part to unevenness in the manual rotation of the potentiometer, and in part due to either fluctuations in plasma properties during the long sweep time or to some sort of arcing at the probe pins. Secondly, the overall shape of the i-δV trace is slightly "S-shaped" and nonlinear, although the portion near the origin appears linear over some range of currents. The slope of the trace

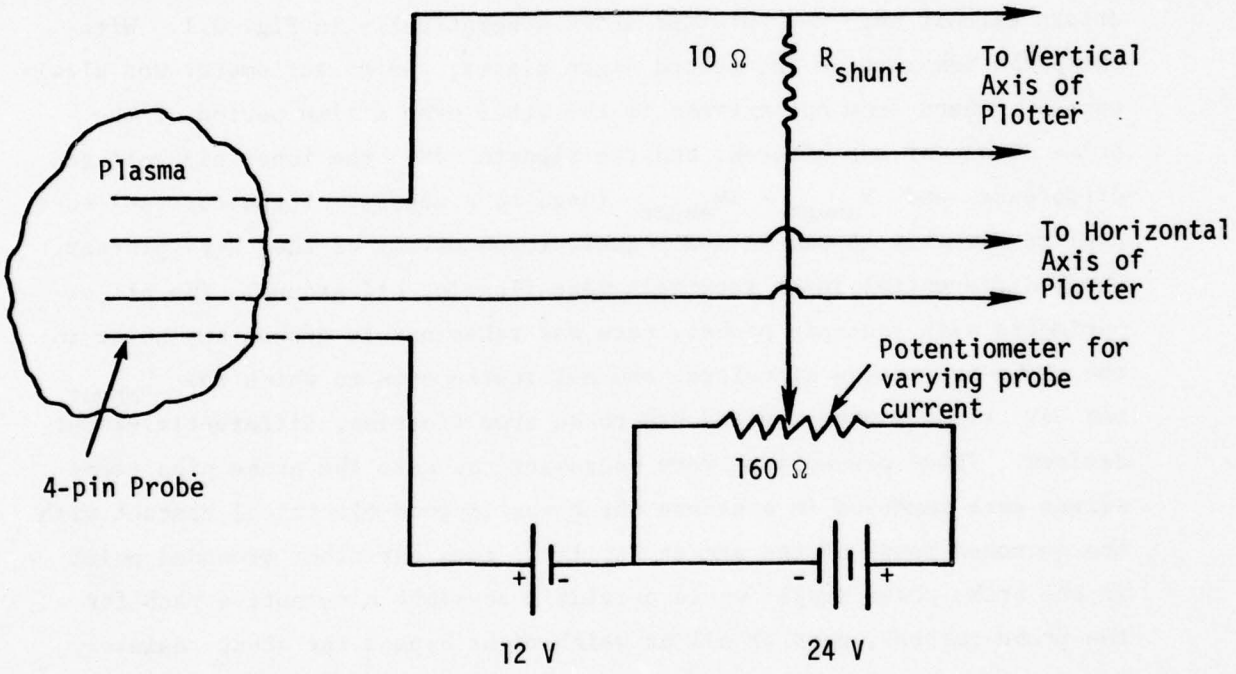


Figure 3.1. Initial circuit for generating i-δV characteristics of 4-pin probes.

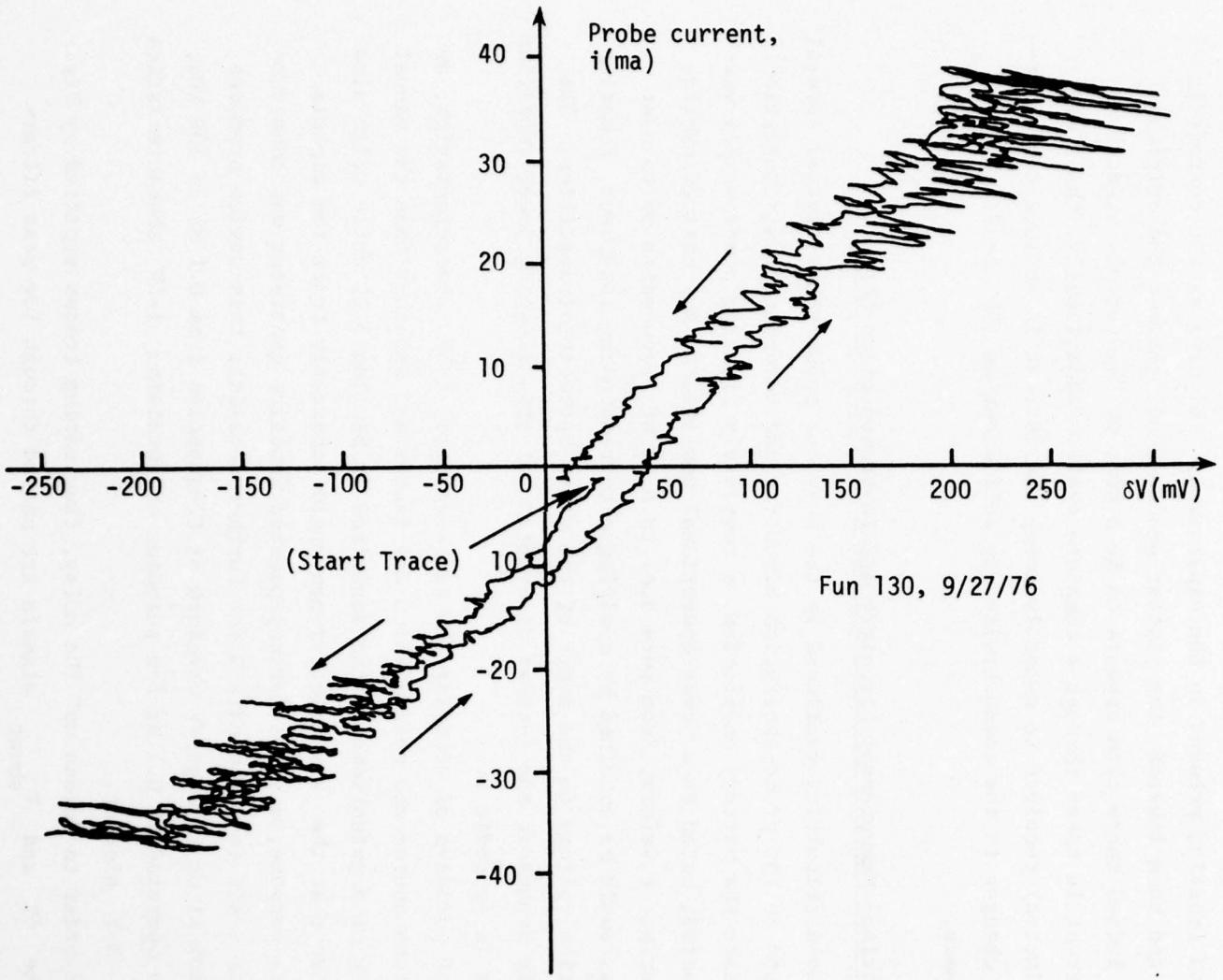


Figure 3.2. Reproduction of typical i-δV characteristic obtained with the circuit of Figure 3.1.

taken near the origin does lead to a value of conductivity consistent with the plasma temperature (as measured only approximately by thermocouples) and seed fraction present in the experiment. Thirdly, as the current is raised and then lowered, the plotter pen does not retrace the original curve; indeed there even appears to be a sort of "hysteresis effect" as the current is taken through a complete cycle. Additionally, the time (1-2 minutes) required to manually sweep the current is so long that appreciable changes in the conductivity may well occur as the i-δV plot is being made.

3.2 Revised Measurement Circuitry and Instrumentation Setup

The difficulties mentioned in the previous paragraph motivated several revisions in the probe-excitation circuitry and recording instrumentation. To replace the battery excitation, a completely floating power supply was constructed, based on a power operational amplifier. Any desired excitation current waveform, from pure d.c. to a.c. at frequencies up to near 100 kHz, could be obtained by applying a corresponding low-power, floating excitation voltage to the input of the power operational amplifier. The complete schematic and further description of this floating power amplifier appears in Appendix D.

For purposes of studying the time-averaged i-δV characteristics, an excitation source was needed which was faster and smoother than the manual sweeping of a potentiometer (as described in Section 3.1) while still slow enough so that the x-y plotter pen could accurately track the signals. For this purpose, a small battery-powered function generator was constructed from a kit (see Appendix D for further details); this device produces a sinusoidal or triangular waveform at frequencies from 0.1 Hz to 100 kHz, and was operated at 0.1 Hz for purposes of obtaining i-δV characteristics on the X-Y plotter.

In order to "clean up" the noisy, fluctuating traces typified by Fig. 3.2, the δV and V_{shunt} signals are passed through low-pass filters before being sent to the plotter. With the excitation frequency set at 0.1 Hz, the cutoff frequency of these commercial filters (Rockland Systems Corp. Model 452 Dual Hi/Lo Filters) was typically set at 0.2 Hz. Since the input terminals on these filters are single-ended (i.e., one input terminal

is grounded), and it was desired to maintain the entire measuring circuit floating, it was necessary to pass the δV and V_{shunt} signals through unity-gain differential amplifiers, which act as isolation stages, before inputting these signals into the filters. With all of these changes, the final experimental electronics configuration for obtaining "high quality" i-δV plots from the four-pin probe is as shown in Fig. 3.3.

3.3 Results of Studies of i-δV Characteristics

Using the experimental setup of Fig. 3.3, i-δV characteristics of two different probes were recorded after varying (and recording) the amplitude of the 0.1 Hz voltage applied to the outer pins of the probe, $V_{outer,max}$, and varying the plasma temperature (and thus the magnitude of the conductivity). In several of the runs, the seeded argon was diluted with 3% by volume of nitrogen to reduce the possibility of electron temperature nonequilibrium in regions of locally high current density. For the various run conditions, simultaneous plots of i vs. V_{outer} and of i vs. δV were recorded. The main results of these experiments will now be discussed.

It was found that the i-δV characteristics were always linear so long as $V_{outer,max}$ was kept below about 1.0 volts. Also, for values of $V_{outer,max}$ less than roughly 0.5 volts, the quality of the i-δV plots seemed to deteriorate, presumably due to decreased signal-to-noise ratios. Sample i-δV plots for varying $V_{outer,max}$ are reproduced in Figs. 3.4a, 3.4b, and 3.4c, in which $V_{outer,max}$ had values of 6 volts, 0.17 volts, and 0.71 volts, respectively. The best quality, most linear i-δV characteristics were obtained, no matter which probe was used and no matter what the numerical value of σ, for $V_{outer,max} \simeq 0.75$ volts, and Fig. 3.4c is a typical sample characteristic. It is clear that the low-pass filters smooth out the small fluctuations such as those in Fig. 3.2, and the "hysteresis effect" is minimized or absent entirely. The values of σ obtained by measuring the slopes of the characteristics and multiplying by the probe constant obtained using the formula (1.6) always lie within the (rather wide) range of expected values of σ based on the relatively inaccurate thermocouple-determined temperature. The behavior of the i-δV characteristics was unchanged, so far as we were able to judge, by the presence of nitrogen in the plasma.

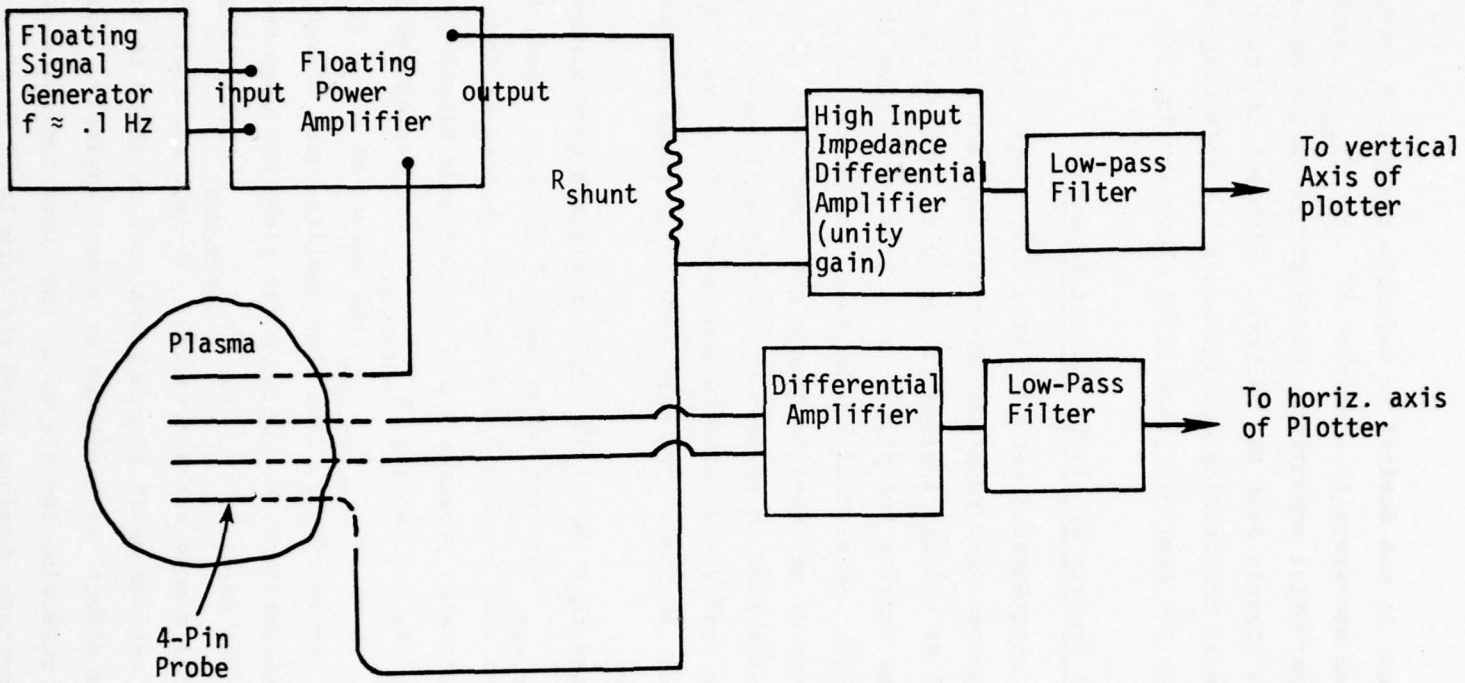


Figure 3.3. Electronics configuration for obtaining "high-quality" i-δV characteristics of 4-pin probes.

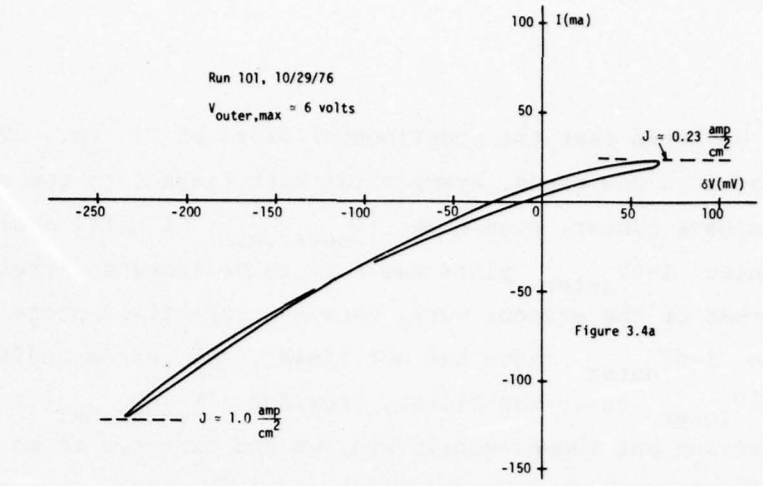


Figure 3.4a

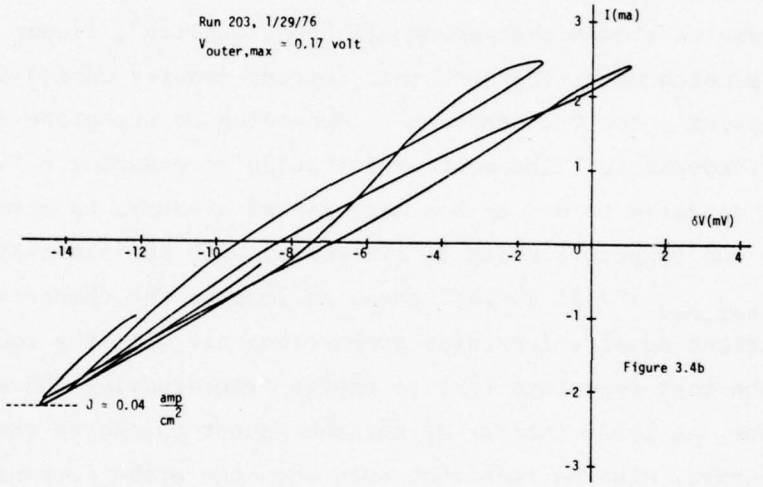


Figure 3.4b

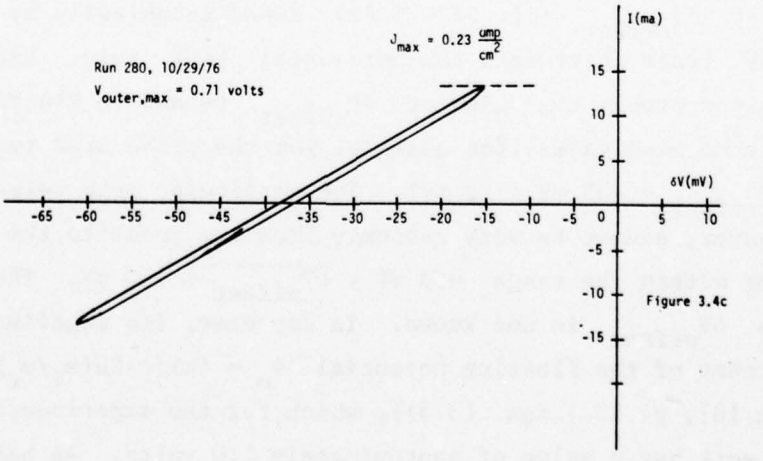


Figure 3.4c

Figure 3.4. Sample i-δV characteristics of four-pin probes for several values of $V_{outer, max}$, from test of 10/29/76.

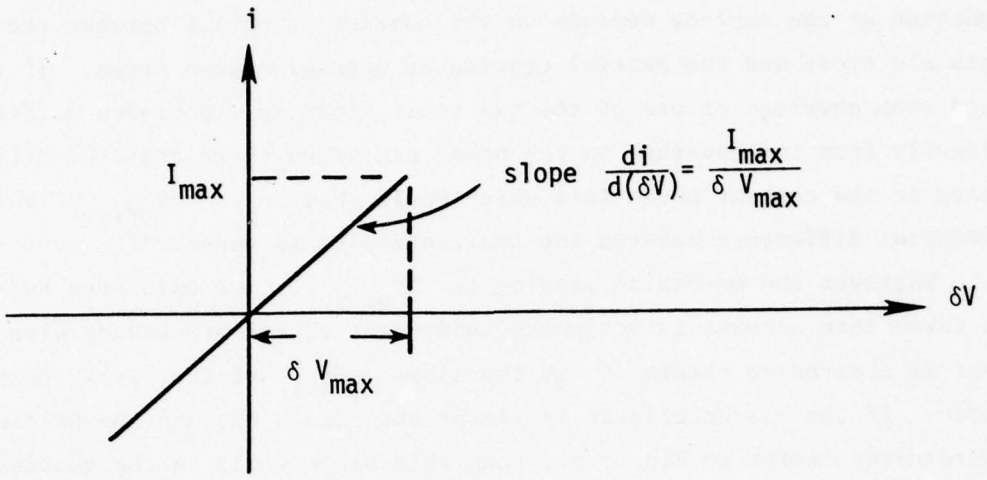
It should be noted that the experimental plots of i vs. δV_{outer} were not, except in a few cases, symmetrical with respect to the origin, nor were they always linear, even when $|V_{outer,max}| \simeq 1$ volt. The interpretation of these i-δV_{outer} plots was felt to be somewhat irrelevant to the main thrust of the present work, however, especially since even in cases where the i-δV_{outer} curve was not linear, the corresponding "more important" i-δV_{inner} curve was linear, provided $|V_{outer,max}| \simeq 1$ volt.

Before carrying out these experiments, we had expected to be able to formulate a rule-of-thumb for obtaining linear i-δV characteristics in terms of the current density at the surface of the outer probe electrodes. However, the results showed that among all "good quality", linear i-δV characteristics which were recorded, this current density varied over the range 0.05 amps/cm^2 to 0.25 amps/cm^2, depending on the probe size and on the plasma temperature. The most useful guide to ensuring a linear characteristic appeared to be, as has been stated already, to maintain $V_{outer,max}$ in the range 0.5 volts to 1.0 volts, with the cleanest data found for $V_{outer,max} \simeq 0.75$ volts; then, so long as the characteristic was linear, the current density increased proportionately with the conductivity.

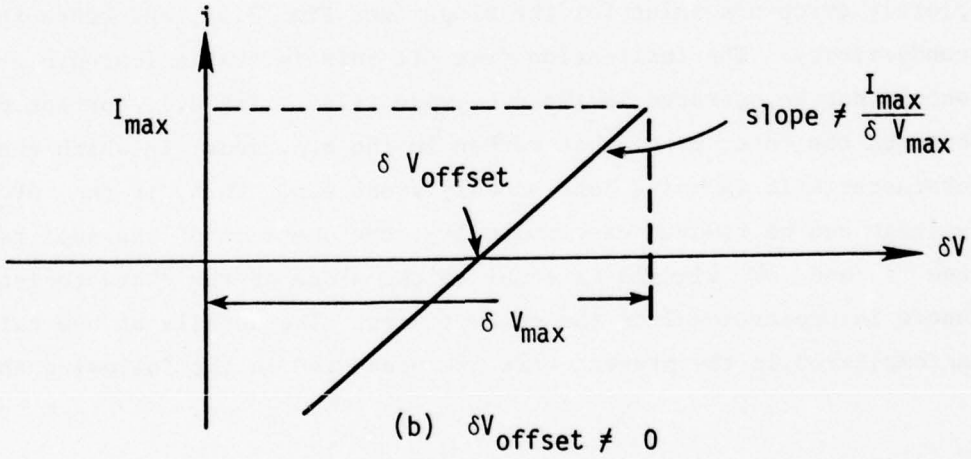
Perhaps the most important fact to emerge from studying the experimental i-δV plots, at least insofar as the subsequent course of the experiments was concerned, was the fact that even when the probe current i goes to zero, there is still a fairly large voltage difference between the inner pins, denoted by δV_{offset} (cf. Fig. 3.4c), found graphically by locating where the i-δV trace intercepts the horizontal (δV) axis. Experimentally, for a given probe, the value of δV_{offset} tended to fluctuate slowly around some mean value (for example, for the probe used to obtain Fig. 3.4c, $\delta V_{offset} \simeq -35$ mV $\pm$ 10 mV). The particular mean value, $\overline{\delta V_{offset}}$, however, seemed to vary randomly from one probe to the next, usually falling within the range -50 mV $\lesssim \overline{\delta V_{offset}} \lesssim +50$ mV. The precise origin of this δV_{offset} is not known. In any case, its magnitude is at most a few percent of the floating potential $\phi_o = (kT/e)\ell n(m_i/m_e)^{1/2}$ (cf. Reference [8], p. 132, Eqn. (3.5)), which for the experimental conditions of this work has a value of approximately 1.0 volts. As has been suggested in Section 1.3 (cf. Fig. 1.2 and Eqn. (1.4)), some plausible mechanisms giving rise to a nonzero δV_{offset} are differences in sheath

voltage drops (due perhsps to slight differences in probe tip temperatures) and/or differences in the work function voltage drops. The effective work function at the surface depends on the contact potential between the tungsten electrode and the partial coating of potassium seed atoms. If the seed atom coverage of one of the two inner floating electrodes differs slightly from the coverage on the other pin, then there could be differences in the contact potentials which would show up as δV_{offset} when the potential difference between the two inner pins is measured.

Whatever the mechanism leading to δV_{offset}, its existence had to be taken into account in designing subsequent signal-processing electronics. What is desired to obtain σ is the slope $\frac{di}{d(\delta V)}$ of the i-δV characteristic. If the characteristic is linear and passes through the origin of coordinates (refer to Fig. 3.5), then this slope would be the quotient of the amplitudes of the two a.c. signals, which is easy to obtain continuously using an electronic analog divider. However, if (as is in fact the case) the characteristic is linear but does not pass through the origin, then the simple quotient of the maximum i and δV signals gives a completely erroneous value for the slope (see Fig. 3.5), and hence for the conductivity. The implication from all this is that a four-pin probe should not be operated in the d.c. mode (i.e., with d.c. current passing between the outer pins), but rather in the a.c. mode, in which the i-δV characteristic is being continuously swept out. Then, if the δV_{offset} voltage can be removed electronically, the quotient of the amplitudes of the i and δV signals is equal to the slope of the characteristic, and hence is proportional to the conductivity. The details of how this was accomplished in the present work are presented in the following chapter.



(a) $\delta V_{offset} = 0$ or removed electronically by signal processing



(b) $\delta V_{offset} \neq 0$

Figure 3.5. Illustrating possible error in obtaining true slope of I-δV characteristics as the quotient $I_{max}/\delta V_{max}$ in the presence of non-zero δV_{offset}.

Chapter 4

FINAL SIGNAL-PROCESSING SYSTEM

4.1 Use of High-Pass Filters and Audio-Frequency Excitation

In order to obtain an i-δV characteristic which was linear and always passed through the origin, it was necessary to filter electronically the i and δV signals. Since the offset signals were observed to vary at frequencies less than one or two kilohertz, it was decided to power the outer pins of the probe at a much higher frequency (well into the audio-frequency range) and to employ a high-pass filter adjusted to attenuate the offset signal, but to pass the excitation signal. A typical value used for the excitation frequency was 20 kHz, in which case the high-pass filter's cutoff frequency would be set around 15 kHz.

The instrumentation setup, shown below in Fig. 4.1, is similar in appearance to the low-frequency setup of Fig. 3.3 previously described, except that now the source frequency was raised from 0.1 Hz to around 20 kHz, and the low-pass filters with cutoff frequencies around 0.2 Hz were switched to high-pass filters with cutoffs of 10 kHz to 15 kHz. (Actually the same instruments, Rockland Model 452 Dual Hi/Lo Filters, which can be operated in either the high-pass or low-pass mode and have adjustable cutoff frequencies, were used in both setups.) The differential amplifiers again play the role of isolating the two signals from ground, and were now operated with sufficient gain to raise the signal levels from a few tens of millivolts to a few volts before inputting them into the high-pass filters. Since the X-Y plotter clearly cannot plot out characteristics at 20 kHz, an oscilloscope was used as the X-Y plotting device, with the amplified and filtered current signal applied to its vertical deflection plates and the corresponding δV signal applied to the horizontal deflection plates.

A typical photograph of the resulting i-δV characteristics is reproduced in Fig. 4.2. Note that the plots are all very linear and do pass through the origin. Also, there is no noticeable phase shift between i and δV, since the plots are linear and not elliptical. During the

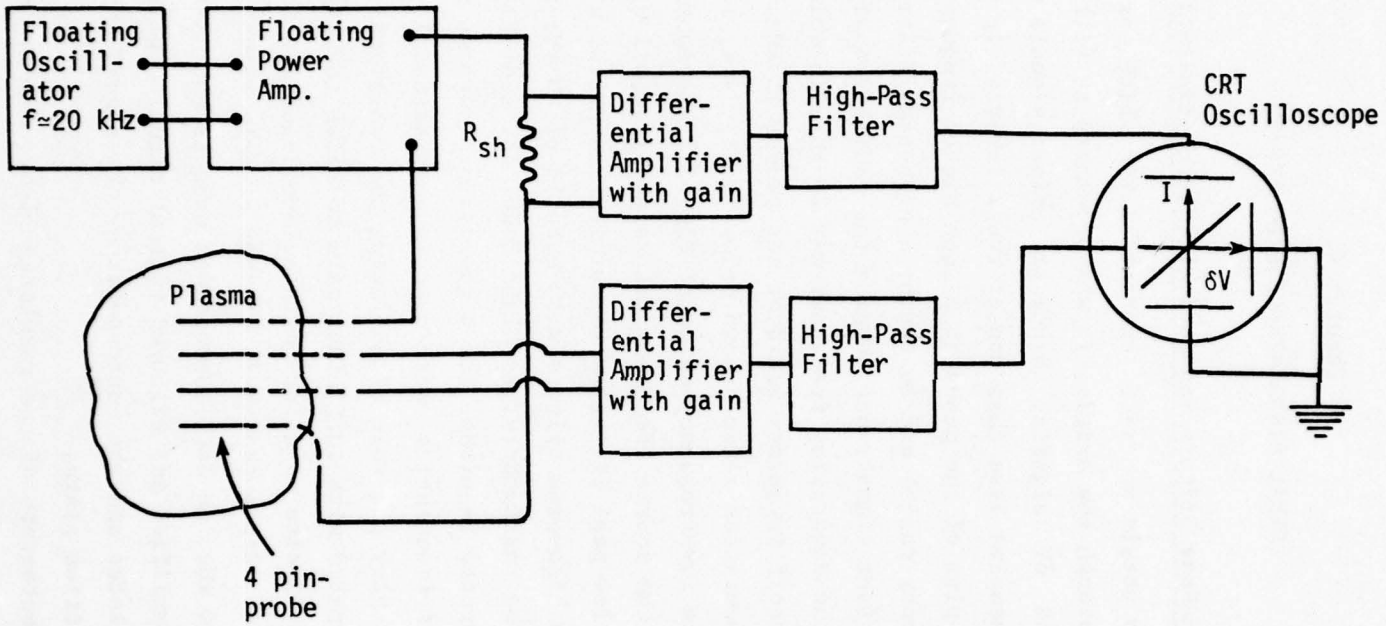


Figure 4.1. Circuit used to study i-δV characteristics while 4-pin probe is driven at audio frequencies.



Figure 4.2. Typical i-δV plot obtained with the measuring circuit of Figure 4.1. Data from run 133 of 2/11/77. The minimum and maximum slopes correspond to conductivities of 10.0 mho/m and 26.8 mho/m, respectively. Exposure time = 1/60 sec.

exposure time for this photograph (1/60 sec), many complete i-δV plots were swept out, and, while the individual plots are linear, their slopes vary over some range. As is shown in more mathematical detail in Appendix E, these variations in slope actually represent and are proportional to the fluctuations in the electrical conductivity in the plasma, even though such fluctuations may have frequencies well below the cutoff frequencies of the high-pass filters. The basic reason for this at-first-confusing result (viz, how low-frequency conductivity fluctuations can "get through" the high-pass filters) is that the conductivity fluctuations affect only the amplitudes of the high-frequency "carrier signals" i and δV, which pass unaltered (in either frequency or amplitude) through the filters. Thus the amplitudes of the signals emerging from the filters can and do still vary at the frequencies of the (slower) conductivity variations, which consequently are seen as changes in the slope of the i-δV characteristics, such as those of Fig. 4.2.

4.2 Remaining Signal-Processing Components

As a result of the signal processing described in the previous section, the signals emerging from the two high-pass filters have the form

$$\left.\begin{aligned} V_{shunt}(t) &= V_{shunt,max}(t) \sin \omega_s t = R_{shunt}\, I_{max}(t) \sin \omega_s t \\ \delta V(t) &= \delta V_{max}(t) \sin \omega_s t \ , \end{aligned}\right\} \quad (4.1)$$

where ω_s is the excitation frequency ($\simeq$ 20 kHz). Since the plot of $V_{shunt}(t)$ vs. $\delta V(t)$ has the form of straight lines passing through the origin of coordinates (see Fig. 4.2), the slope of the characteristic V_{shunt} vs. δV, which is proportional to the conductivity, is just equal to the quotient $V_{shunt,max}(t)/\delta V_{max}(t)$, so we may write

$$\sigma(t) = (\text{const.}) \frac{V_{shunt,max}(t)}{\delta V_{max}(t)} \quad (4.2)$$

Thus, in order to continuously monitor $\sigma(t)$, one needs to obtain signals directly proportional to the amplitudes $V_{shunt,max}(t)$ and $\delta V_{max}(t)$ and input these into the numerator and denominator input terminals of an

analog divider circuit, whose output will then be a signal proportional to the time-varying conductivity, $\sigma(t)$.

Signals proportional to $V_{shunt,max}(t)$ and $\delta V_{max}(t)$ were obtained by first passing both the signals represented by Eqn. (4.1) through precision linear full-wave rectifier circuits (see Appendix D for circuit details), and then sending the rectified signals into low-pass filters with cutoff frequencies well below the excitation frequency ω_s but above the highest expected frequency of the conductivity fluctuations. The outputs of these latter low-pass filters consisted of time-varying positive-valued voltages proportional to the amplitudes $V_{shunt,max}(t)$ and $\delta V_{max}(t)$. These latter signals were subsequently amplified by variable-gain amplifiers whose gains were selected for each experiment to give optimum input values for the numerator and denominator of an Analog Devices Model 436A analog divider. (This particular device requires that at all times the numerator input signal be less than or equal to the denominator input signal, and that the denominator signal lie within the range 0.1 volt to 10 volts. The variable-gain amplifiers allowed the operator to adjust the signal levels to comply with these conditions before taking data.) A schematic diagram showing the effects of the rectifiers, low-pass filters, and variable-gain amplifiers on a sample waveform emerging from the high-pass filter is shown in Fig. 4.3 below.

The voltage emerging from the analog divider is directly proportional to the electrical conductivity of the plasma as a function of time, and provides a time-resolved measurement of $\sigma(t)$. To record this time-resolved conductivity data, the signal was sent directly to an analog tape recorder, and also to an oscilloscope for visual monitoring. For experiments in which the time-averaged conductivity was the variable of interest, this same signal was sent to a final low-pass filter which smoothed out the fluctuations, and thereafter to a stripchart recorder which gave a continuous visual display of the mean conductivity. The procedure for calibrating this system, taking into account the gain factors of the several electronic signal-processing components and the probe calibration constant k_p (cf. Section 1.3) is discussed in the following two sections of this chapter. First, however, we present in Fig. 4.4 a block diagram of the entire signal-processing system, and in Fig. 4.5 a set of sample waveforms

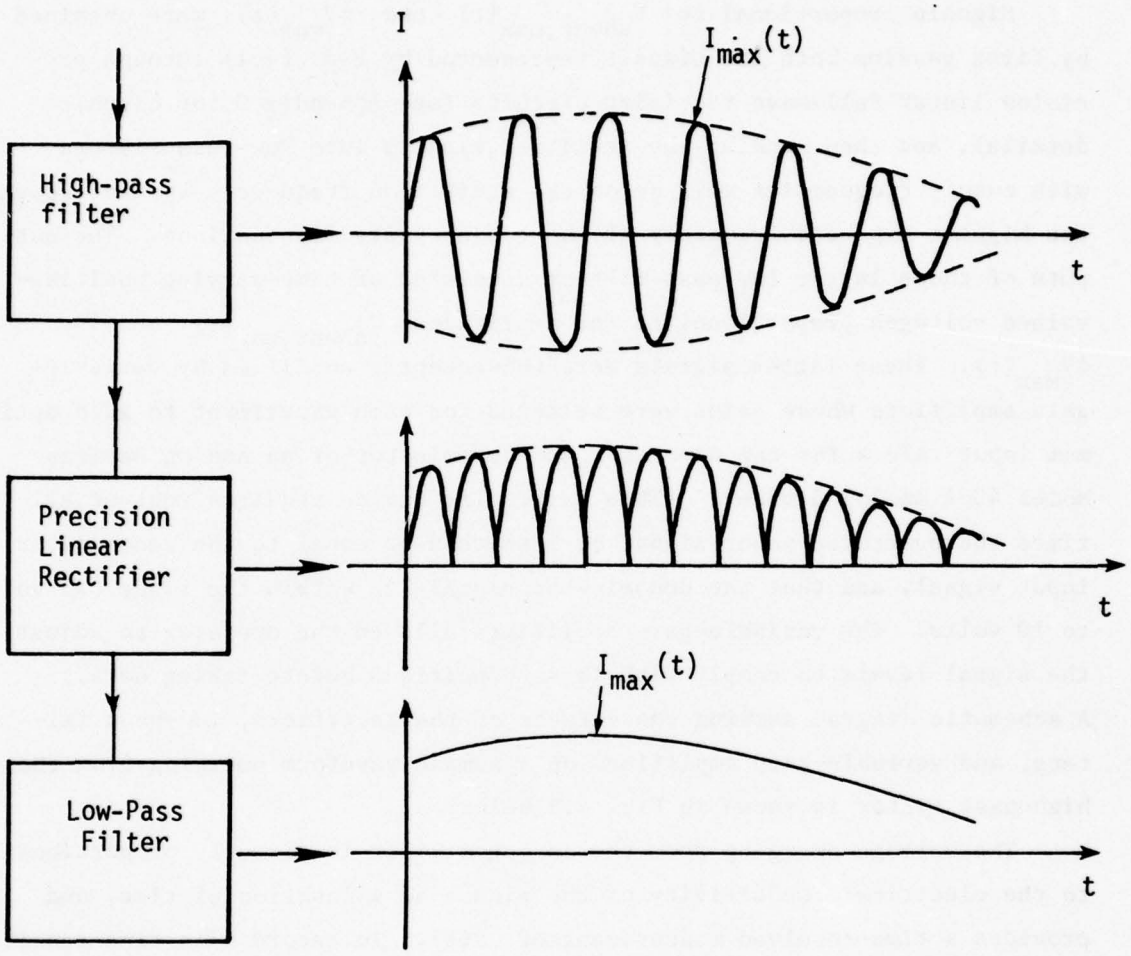


Figure 4.3. Sketch of sample waveforms at the output terminals of the high-pass filter, rectifier, and low-pass filter.

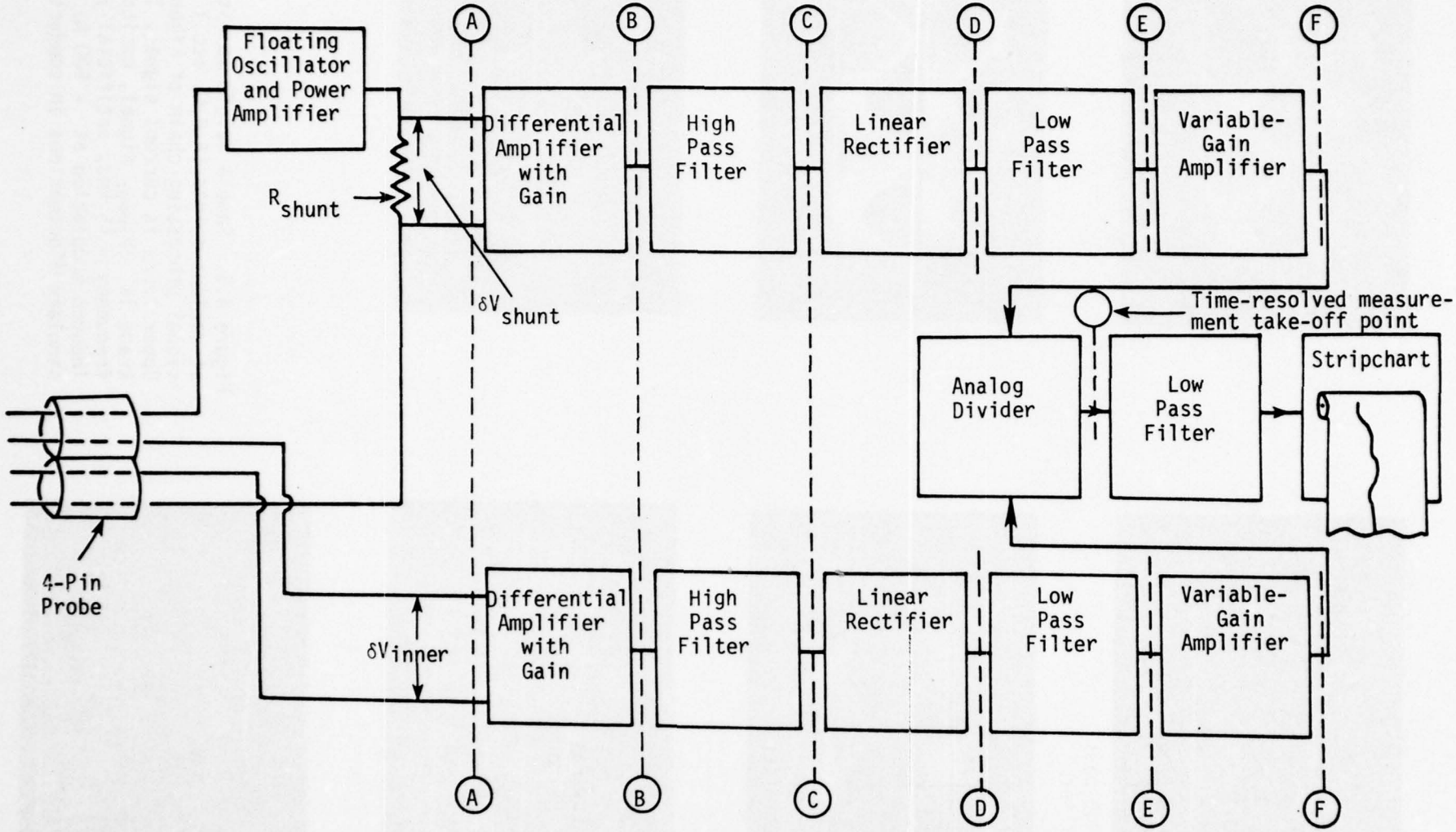
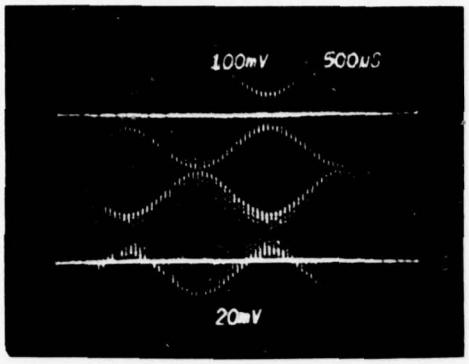
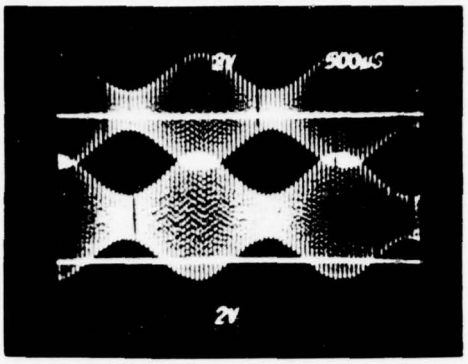


Figure 4.4. Block Diagram of Signal Processing Electronics Used with 4-Pin Probe.

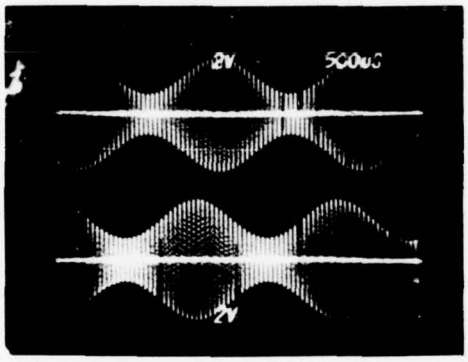
A



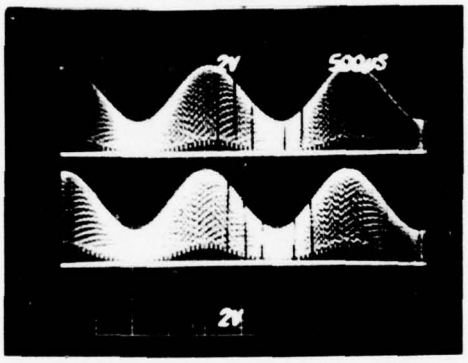
B



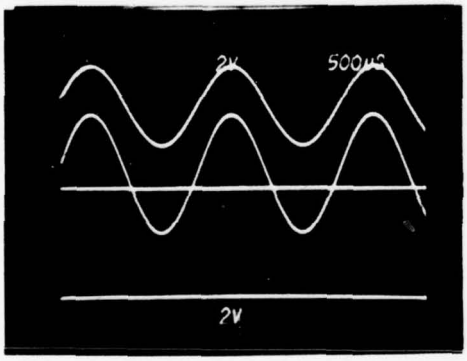
C



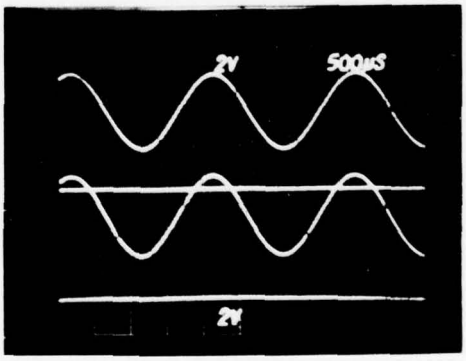
D



E



F



G

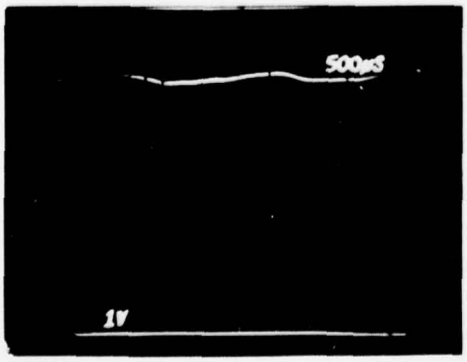


Figure 4.5. Sample waveforms obtained at various points (A,B,C, etc.) in signal processing chain of Figure 4.4. Upper trace is current signal, lower trace is δV_{inner} signal, excitation frequency ≃ 15 khz, artificially-induced modulation at ≃ 500 hz to simulate fluctuations in conductivity.

obtained at each station in the signal-processing chain, using a dummy probe with artificially induced fluctuations in the i and δV signals.

4.3 Procedure for Calibrating the Electronics, Using a Dummy Probe

A simplified diagram of the signal-processing system of Fig. 4.4 is shown in Fig. 4.6, in which the differential amplifier, high-pass filter, rectifier, low-pass filter, and variable-gain amplifier for each of the numerator and denominator chains have been "lumped" into a single component having some net gain factor, g_{net}, which equals the product of the individual gain factors of its constituent components. In addition, Fig. 4.6 shows switches which allow the operator to switch the current supplied by the probe power supply back and forth from the "real" four-pin probe (which may be immersed in either the plasma or in the calibrating electrolyte solution) to a set of three fixed resistors (R_3,R_4, and R_{12}) which constitute what we refer to as a "dummy probe".

The operator adjusts all the gain factors of the electronic components such that, when the switches connect, alternately, the real and the dummy probes into the circuit, all the signals remain within their allowable ranges. Once this is done, the operator switches to the dummy probe and reads the corresponding constant divider output, Q_{dummy}, with an accurate voltmeter. Then he switches over to the real probe and reads (or records on tape or a stripchart) the corresponding (possibly time-varying) divider output, Q_{real}. From these two measurements, plus a knowledge of the probe constant k_p and the value of the resistor R_{12}, the conductivity of the fluid in which the real probe is immersed can be determined, as explained below.

When the dummy probe is in the circuit, a divider output is given by the relation

$$Q_{dummy} = 10 \frac{V_{N,dummy}}{V_{D,dummy}} = 10 \frac{g_{net,num}}{g_{net,denom}} \frac{V_{shunt,dummy}}{V_{R_{12}}}$$

$$= 10 \frac{R_{sh} I_{dummy} g_{net,num}}{R_{12} I_{dummy} g_{net,denom}} ,$$

from which it follows that

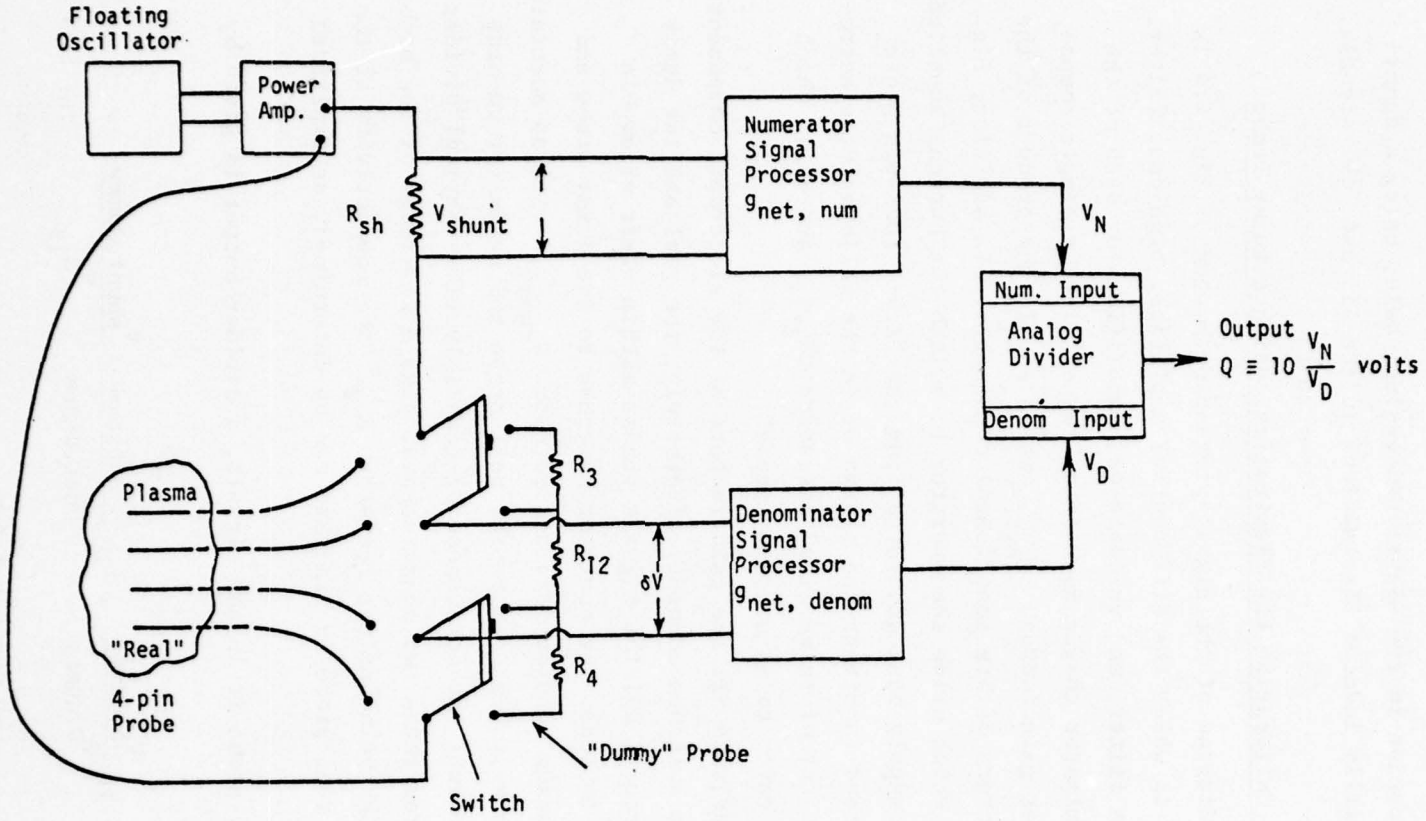


Figure 4.6. Dummy probe circuitry employed in calibrating the signal processing electronics.

$$\frac{g_{net,denom}}{g_{net,num}} = \frac{10\ R_{sh}}{Q_{dummy} R_{12}} \tag{4.3}$$

From Eqn. (1.5), $\sigma = k_p \frac{di}{d(\delta V)}$. Also, after suitable signal processing, as discussed above, the i-δV characteristics are linear and pass through the origin of coordinates, so we have that $\sigma = k_p\ (I_{max}/\delta V_{max})$, which may be written in terms of the notation of Fig. 4.6 as follows:

$$\sigma = k_p \frac{I_{max}}{\delta V_{max}} = k_p \frac{V_{shunt,max}}{R_{sh} \delta V_{max}} = \frac{k_p}{R_{sh}} \frac{V_{N,real}/g_{net,num}}{V_{D,real}/g_{net,denom}}$$

$$= \frac{k_p}{10\ R_{sh}} \left(\frac{g_{net,denom}}{g_{net,num}} \right) \left(10 \frac{V_{N,real}}{V_{D,real}} \right) . \tag{4.4}$$

Substituting (4.3) into (4.4) and identifying the last term in brackets in (4.4) as the divider output Q_{real}, we obtain

$$\sigma(t) = \frac{k_p}{R_{12}} \frac{Q_{real}(t)}{Q_{dummy}} , \tag{4.5}$$

which is the working equation for determining the electrical conductivity with the four-pin probe and electronics setup already described.

4.4 Procedure for Determining the Probe Constant, k_p

The probe constant k_p in Eqn. (4.5) was determined experimentally using the identical electronics setup shown in Figs. 4.4 and 4.6. The only differences in procedure were that (a) the probe being calibrated was immersed in a carefully prepared aqueous $KC\ell$ solution whose conductivity, $\sigma_{KC\ell}$, is accurately known from handbooks, and (b) the excitation frequency and cutoff frequencies of the filters were different when using the probe in the electrolyte solution than when using the probe in the plasma. For measurements in the electrolyte, excitation frequencies around 1 kHz were found to be most suitable, and measurements of k_p were in fact taken over a range of frequencies (typically 100 Hz to 10 kHz). The high-pass filter cutoff was lowered to around 10 Hz for these measurements.

For each excitation frequency, the following quantities were measured: the $KC\ell$ solution temperature (which was needed to accurately determine the conductivity $\sigma_{KC\ell}$ from tabulated tata), the divider output Q_{dummy}

when the dummy probe was switched into the circuit, and the divider output $Q_{real,KC\ell}$ obtained when the real probe being calibrated is immersed in the standard $KC\ell$ solution. Substituting these quantities into the working equation (4.5) and solving for k_p yields

$$k_p = R_{12}\, \delta_{KC\ell}\, \frac{Q_{dummy}}{Q_{real,KC\ell}} \quad , \tag{4.6}$$

which is the working relation used to determine k_p. It was found that, unless great care was taken, k_p as determined by (4.6) had a fairly large frequency dependence, related to polarization effects in the electrolyte. Appendix A presents in more detail the procedures used to overcome these problems and obtain reasonably accurate values of k_p. The predominantly "ratiometric" character of the whole signal-processing and experimental procedure is illuminated by substituting Eqn. (4.6) into Eqn. (4.5) to obtain the result

$$\sigma_{plasma}(t) = \sigma_{KC\ell}\, \frac{(Q_{real,plasma}(t)/Q_{real,KC\ell})}{(Q_{dummy,plasma}/Q_{dummy,KC\ell})} \quad . \tag{4.7}$$

Chapter 5

INVESTIGATIONS OF FLOW EFFECTS ON INDICATED CONDUCTIVITY

5.1 Description of Experiments

Investigations of flow effects on the time-averaged conductivity indicated by the four-pin probes were carried out using two probes simultaneously, a fixed probe and a mobile probe, both operated with identical but separate electronics. As explained in Section 4.2, the outputs of the analog dividers for each probe were sent through final low-pass filters (whose cutoff frequencies were usually set at around 2 Hz) to accomplish the time averaging, and then to separate channels of an eight-channel analog stripchart recorder. The fixed probe, located in the low-velocity region of the plenum chamber, was employed mainly because many prior experiments had shown that slow, often erratic, and often fairly large changes in the conductivity of the seeded, arc-heated argon flow did occur even for nominally constant flow conditions. The purpose of the fixed probe was thus to monitor these changes in the "background" conductivity which were not due to flow effects, so as to avoid erroneously interpreting variations of indicated conductivity on the mobile probe as being due to flow effects. Thus, the fixed-probe output served as a "normalization factor", and in all the final results of these experiments we plot the quotient, $\sigma_{mobile}/\sigma_{fixed}$, of the indicated conductivities from the two probes at the same instant in time.

The procedure used to study the effects of flow velocity on the indicated conductivity (σ_{ind}) was to translate the mobile probe axially in and out along the centerline of the converging nozzle, thereby varying the flow velocity at the probe tip. The axial position, z, of the probe (from which the velocity was later deduced as described in Appendix C) was monitored continuously by a position transducer whose output was recorded on the eight-channel stripchart.

Similarly, to study the effects of the orientation of the pins and to measure radial profiles of conductivity in the flow, the probe mount was slowly rotated through the angle θ, or translated radially through radial

distance r normal to the flow. The variables r and θ were monitored with position transducers and similarly recorded on the same eight-channel stripchart.

In addition to the indicated conductivities of the two probes and the position variables z, r, and θ, several other signals were simultaneously recorded on the stripchart. These signals included the gas temperature (actually the junction emf of a tungsten thermocouple in the plenum), the arcjet current and voltage drop, and a voltage proportional to the rate of injection of seed (NaK) into the plenum.

5.2 Effects of Flow Velocity on Indicated Conductivity

Figures 5.1 and 5.2 are reproductions of portions of actual stripchart records obtained in the experiments just described. These figures show the output of the axial position transducer and of the fixed and mobile probes, and illustrate that, while the fixed probe output remains fairly constant, the mobile probe output decreases as the velocity increases. In other words, these stripchart records already indicate the existence of a substantial velocity effect on the indicated conductivity. Figs. 5.1 and 5.2 show two different "modes" of data-taking: in Fig. 5.1 the mobile probe was continuously withdrawn and inserted (hence the name "continuous" mode), whereas in Fig. 5.2 the mobile probe was set at several discrete axial stations and data were recorded for at least 30 seconds at each station ("discrete" mode). Because the probes may have some short "transient response time" after a velocity change, during which the probe output is in error, the data obtained in the "discrete" mode may possibly be more accurate than the "continuous" mode data.

After reducing these and other similar stripchart data, employing formula (4.5) to obtain σ_{mobile} and σ_{fixed}, and plotting the quotient of these results vs. u/u_{max}, we obtain the curve shown in Fig. 5.3, in which only "discrete" mode data points were used in sketching in the continuous curve. As can be seen, the indicated conductivity, σ_{mobile}, is reduced by around 50% as the velocity increases over the range of velocities achievable in these experiments (namely from about 10 m/sec to about 100 m/sec). This result, while obtained using a particular size four-pin probe in the "end-on" flow configuration, nevertheless indicates that there

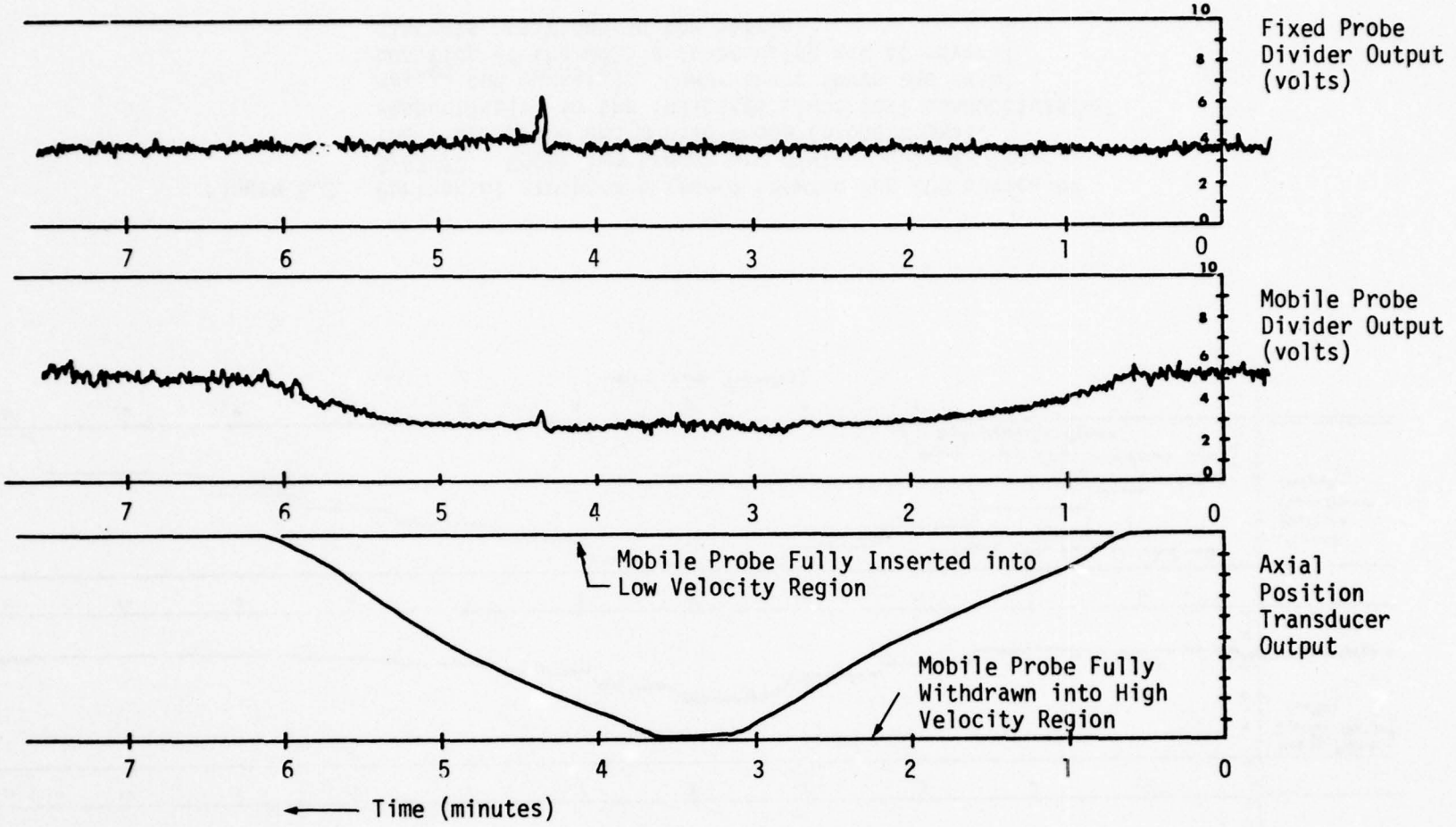


Figure 5.1. Portion of stripchart record showing Run 300 series of 5/27/77. The upper and middle traces are the divider outputs from the fixed probe and mobile probe (proportional, respectively, to the indicated electrical conductivities σ_{fixed} and σ_{mobile}). The lower trace shows the axial position of the mobile probe as it was continuously varied between the low- and high-velocity regions of the nozzle.

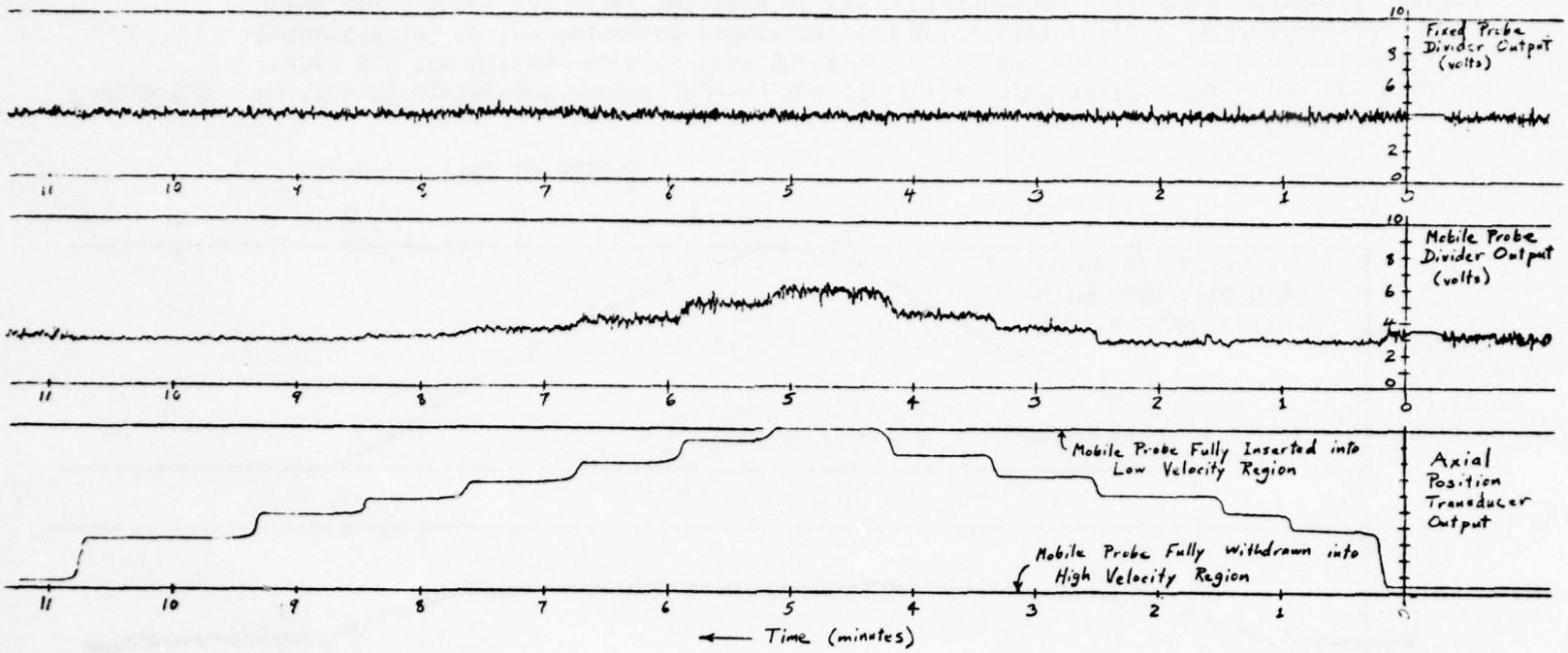


Figure 5.2. Portion of stripchart record showing Run 200 series of 5/27/77. Upper two traces are divider outputs from the fixed probe and mobile probe (proportional, respectively, to the indicated electrical conductivities σ_{fixed} and σ_{mobile}). Lower trace shows the axial position of the mobile probe being set at several discrete positions in the nozzle.

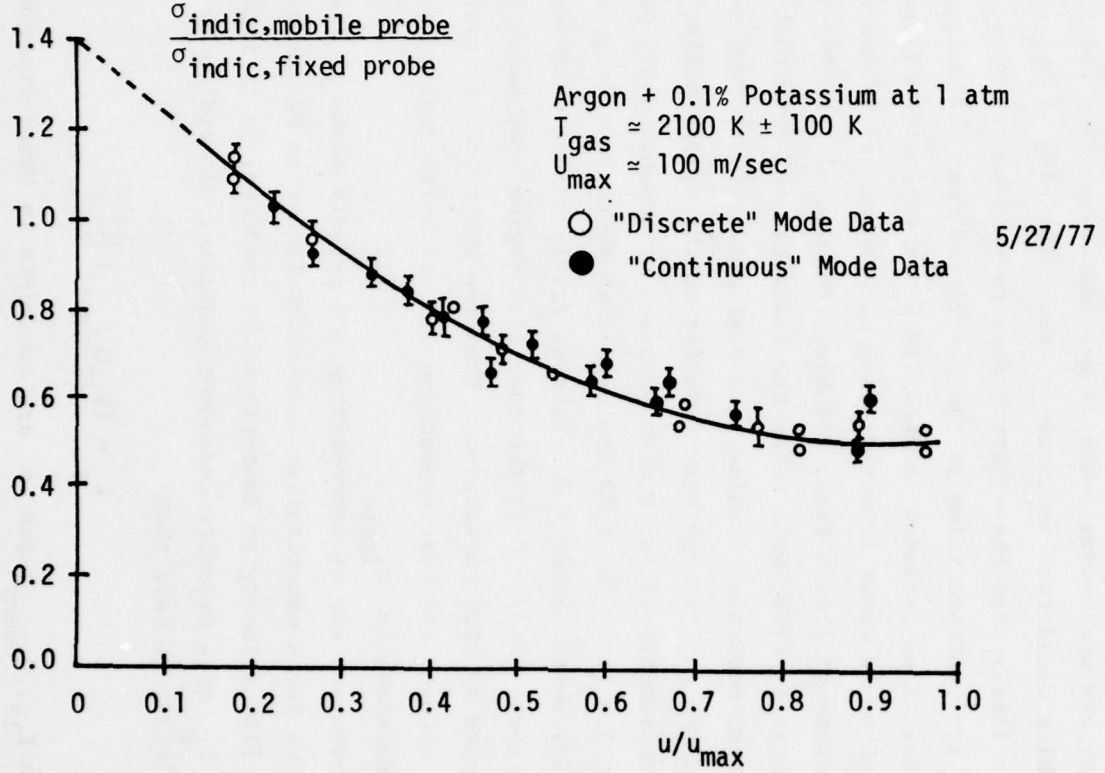


Figure 5.3. Ratio of the indicated conductivity of a mobile 4-pin probe to that of a fixed-position probe, as a function of flow velocity u at the mobile probe tip. The continuous curve was sketched using only the "discrete" mode data. See Figure 5.4 for mobile probe dimensions.

is a significant "flow effect" (vs. a velocity dependence in the indicated conductivity) which must be taken into account when using four-pin probes.

In interpreting the results shown in Fig. 5.3 as evidence of a "flow effect", we have assumed that the local conductivity remains constant in the core flow of the plasma between the upstream and downstream ends of the nozzle. In Appendix F we discuss in more detail this assumption. While there are mechanisms (such as gasdynamics cooling and radiation escape) which would tend to lower σ, the conclusion of Appendix F is that it is likely that the electron density (and hence σ) was partially frozen at its upstream value as the gas flowed down the nozzle in these experiments. Also included in Appendix F are estimates of the conductivity drops which would occur from radiation escape and gasdynamic cooling, even in the absence of frozen flow, and these results all predict less than a 14% conductivity drop, well below the indicated 50% drop that was measured. Still another mechanism leading to a real conductivity drop would be a cooling of the gas through heat transfer to the nozzle walls. However, direct measurements of the radial profiles of conductivity, presented below in Section 5.4 (cf. Fig. 5.8) indicate that there is a large core region in the flow for which $\partial\sigma/\partial r \simeq 0$. This is fairly strong evidence in support of the claim that $\partial T/\partial r = 0$ in the core flow region, and hence that this region is not cooled by heat conduction. Thus the mechanisms of gasdynamic cooling, radiation escape, and heat conduction are not sufficient to explain the observed decrease in σ_{indic}.

A convenient way of interpreting the results shown in Fig. 5.3, and one which allows for a quantitative correction factor to be introduced for the effect of flow velocity on four-pin probe readings, is to regard the probe constant k_p as a velocity-dependent quantity. According to the working equation (4.5), we have that

$$k_p = (R_{12} Q_{dummy}) \frac{\sigma}{Q} \tag{5.1}$$

and, since R_{12}, Q_{dummy}, and σ are constants in these experiments, the decrease in divider output, Q, as velocity increases can be thought of as an increase in the probe constant. (σ may in reality vary by a few percent along the nozzle axis, but for simplicity we assume it to be essentia-ly constant.) The quantity of interest, then, for a given probe, is

the ratio of the values of the probe constant at zero velocity (a quantity measurable to acceptable accuracy in a salt water solution) to that at some non-zero velocity, u. For convenience we introduce the notation

$$f(u) \equiv \frac{k_p(u)}{k_p(u=0)} \tag{5.2}$$

for this ratio, and we shall show how f(u) can be determined from the experimental curve of $\sigma_{indic,mobile}(u)/\sigma_{indic,fixed}(u_{plenum})$ vs. u/u_{max} shown in Fig. 5.3.

By writing Eqn. (5.1) for the mobile probe at some arbitrary velocity u, and dividing by the same equation written for the fixed probe at the particular non-zero but constant velocity u_{plenum} which is present in the plenum at the location of the fixed probe, we obtain the result

$$\frac{k_{p,mobile}(u)}{k_{p,fixed}(u_{plenum})} = \frac{1}{\left(\frac{Q_{mobile}(u)}{R_{12,mobile}Q_{dummy,mobile}}\right)\Big/\left(\frac{Q_{fixed}(u_{plenum})}{R_{12,fixed}Q_{dummy,fixed}}\right)} .$$

Multiplying both sides of this equation by the constant ratio $k_{fixed}(u=0)/k_{mobile}(u=0)$ leads to the result

$$\frac{\left(\frac{k_{p,mobile}(u)}{k_{p,mobile}(u=0)}\right)}{\left(\frac{k_{p,fixed}(u_{plenum})}{k_{p,fixed}(u=0)}\right)} = \frac{f_{mobile}(u)}{f_{fixed}(u_{plenum})}$$

$$= \frac{1}{\left[\frac{k_{p,mobile}(u=0)}{R_{12,mobile}} \frac{Q_{mobile}(u)}{Q_{dummy,mobile}}\right]\Big/\left[\frac{k_{p,fixed}(u=0)}{R_{12,fixed}} \frac{Q_{fixed}(u_{plenum})}{Q_{dummy,fixed}}\right]}$$

in which the terms in square brackets are just σ_{indic}, as calculated from experimental data using Eqn. (4.5). Hence we arrive at the result

$$\frac{f_{mobile}(u)}{f_{fixed}(u_{plenum})} = \frac{1}{\sigma_{indic,mobile}(u) \;/\; \sigma_{indic,fixed}(u_{plenum})} \tag{5.3}$$

in which the right-hand side is the numerical inverse of the curve plotted in Fig. 5.3.

We still do not know the value of the constant $f_{fixed}(u_{plenum})$, but it can be found if we permit ourselves to extrapolate the curve in Fig. 5.3 to $u = 0$. At $u = 0$, we have that $f_{mobile}(u=0) \equiv k_{p,mobile}(u=0)/k_{p,mobile}(u=0) = 1$, and (5.3) thus yields

$$f_{fixed}(u_{plenum}) = \frac{\sigma_{mobile}(u=0)}{\sigma_{fixed}(u_{plenum})} = \begin{pmatrix}\text{vertical intercept of} \\ \text{Fig. 5.3 at } u = 0\end{pmatrix}$$

which has in this case the value $f_{fixed}(u_{plenum}) \simeq 1.4 \pm 0.1$, with the uncertainty being estimated from the uncertainty possible in extrapolating Fig. 5.3 to $u = 0$. With this result we have from (5.3) that

$$f_{mobile}(u) \simeq (1.4 \pm 0.1)\left(\frac{1}{\sigma_{indic,mobile}(u)/\sigma_{indic,fixed}(u_{plenum})}\right)$$

$$= (1.4 \pm 0.1)(\text{Inverse of the curve of Fig. 5.3}) \quad . \qquad (5.4)$$

Using (5.4) together with the experimental curve in Fig. 5.3, the corresponding curve of the probe constant ratio $f_{mobile}(u)$ was calculated as a function of velocity, and is plotted in Fig. 5.4. This curve allows a correction for velocity effects to be made. The conductivity indicated by the four-pin probe is to be calculated from the formula

$$\sigma = \frac{k_p(u=0)}{R_{12}} f(u) \frac{Q}{Q_{dummy}} \quad , \qquad (5.5)$$

or equivalently

$$\sigma = k_p(u=0)\ f(u) \frac{i_{max}}{\delta V_{max}} \quad , \qquad (5.6)$$

in which $k_p(u=0)$ is the value found using stationary electrolytes and $f(u)$ is read from Fig. 5.4.

It should be noted that the curve for $f(u)$ shown in Fig. 5.4 was obtained using only one particular probe, whose dimensions are shown in Fig. 5.4, and this probe was employed in the "end-on" orientation with respect to the flow. Thus, while the present work shows that it is possible to take velocity effects into account for any given probe by performing experiments similar to the ones described in this report, it is not known to

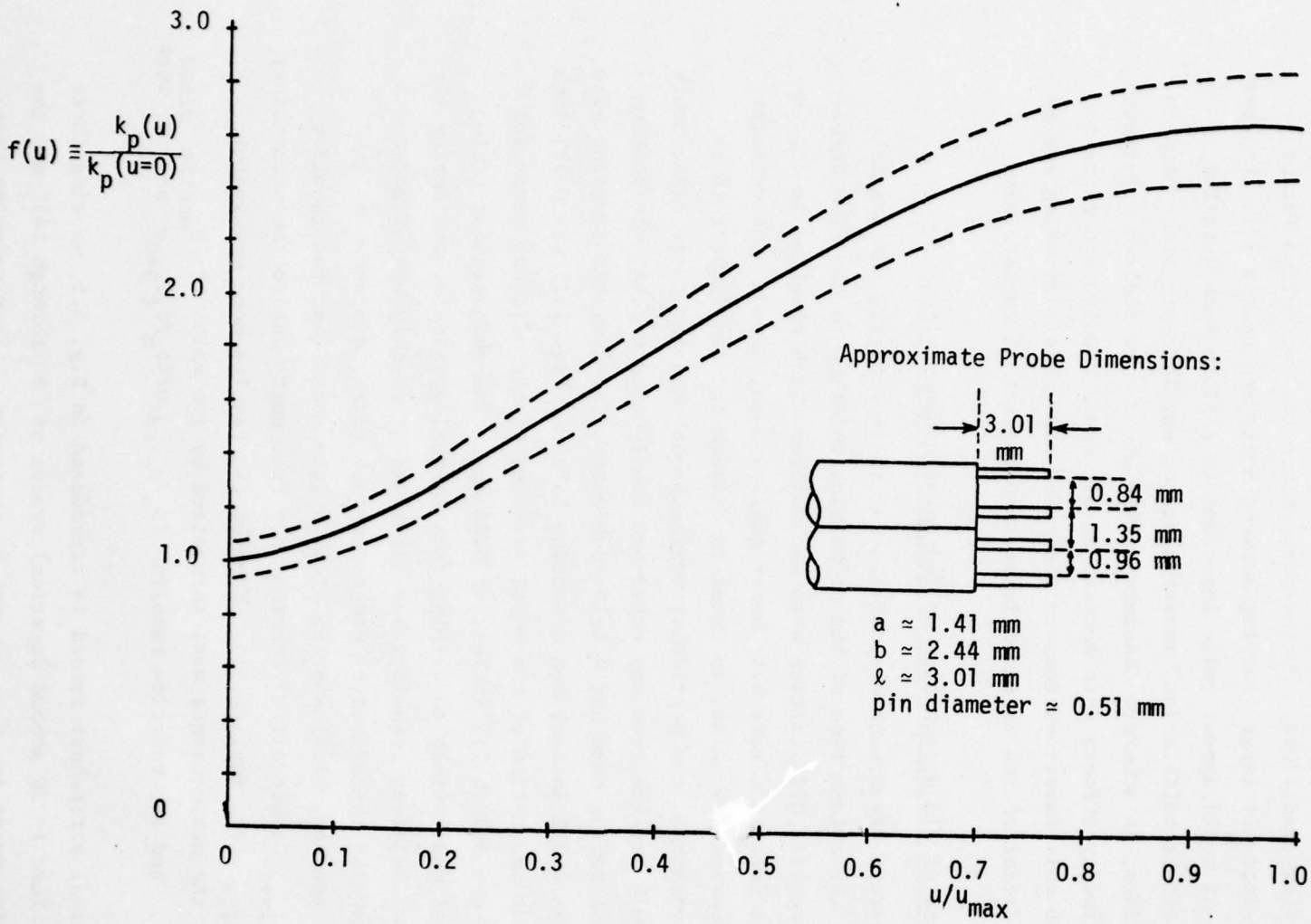


Figure 5.4. f(u) vs. u/u_{max} for the mobile probe used 5/27/77 in "end-on" configuration. The dashed curves represent extremes taking into account the uncertainty in extrapolating Figure 5.3 to u = 0.

what extent the correction factor $f(u)$ may vary with other probe geometries or flow conditions. Furthermore, since the correction factor $f(u)$ is relatively large (varying between unity and nearly 3 in the present work), it would appear quite important to perform such detailed "velocity-effect calibration" measurements on any four-pin probe used in MHD conditions, if accurate absolute values of σ are desired. Failure to take velocity effects into account at all could result, according to the data of this investigation, in indicated conductivities which are as much as a factor of two or three lower than the actual conductivity.

5.3 Effects of Pin Orientation on Indicated Conductivity

A separate experiment was carried out to investigate the possible effects of the orientation of the probe pins relative to the flow direction, and several difficulties were encountered which resulted in considerably less data, and somewhat poorer quality data, than in the velocity effects experiments. Also, in order to disturb the gas flow field as little as possible, the particular mobile probe used for these experiments was made much smaller than any other previously used probes; the double-bore alumina tubing used had a 1/16-inch outer diameter, the tungsten wire diameter was 0.011 inches, and dimension "a" (see Fig. 1.1) was 0.022 inch (so that the separation of the metal surfaces of the adjacent outer and inner pins was only 0.011 inches, or 0.28 mm). The thin ceramic tubing was somewhat susceptible to warping from thermal gradients, and during the test the two adjacent ceramic tubes separated by roughly one diameter, thereby changing the effective probe constant (i.e., distance b increased -- see Eqn. (1.6) and Fig. 1.1). This meant that the quantity $\sigma_{mobile}/\sigma_{fixed}$ could differ considerably from unity due to the uncertainty in $k_{p,mobile}$ (cf. Eqn. (4.5)). To make the results more meaningful, therefore, the measurements were normalized by the value of $\sigma_{mobile}/\sigma_{fixed}$ at $\theta = 0°$, and the relative results $(\sigma_m/\sigma_f)_{\theta\neq 0^o}/(\sigma_m/\sigma_f)_{\theta=0^o}$ vs. θ were plotted.

A typical stripchart record is reproduced in Fig. 5.5, showing three relatively fast (~ 30 second duration) sweeps of θ through $\pm 45°$ and the corresponding drops in σ_{mobile} as θ increases. After reducing these data, plus data from another much slower scan of θ to 30° and back to 0°,

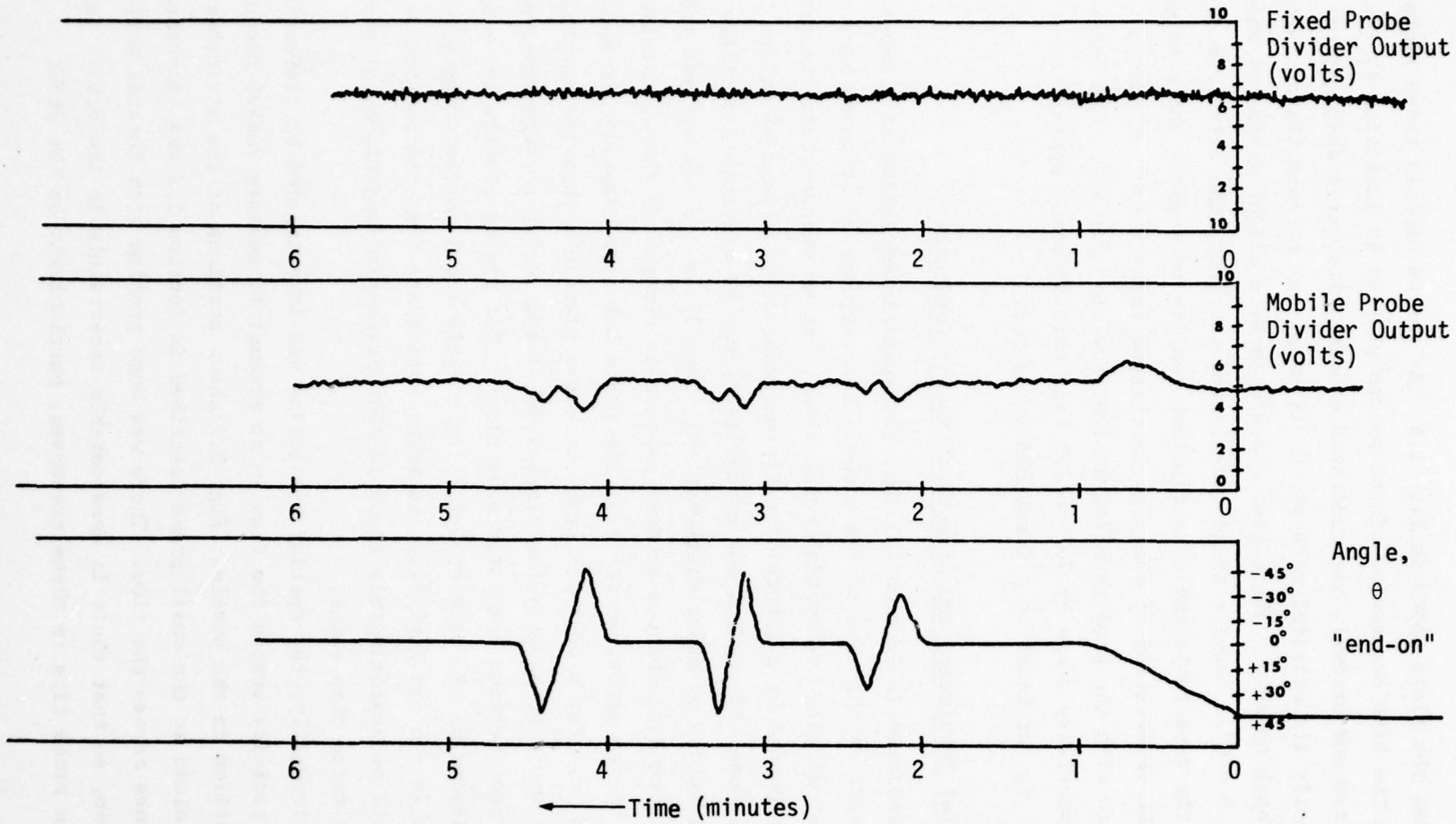


Figure 5.5. Portion of Stripchart Record of 6/1/77, showing effects of variation of the probe orientation angle θ on the indicated conductivity.
Upper trace: Fixed probe output (proportional to $\sigma_{indic\ fixed}$)
Middle trace: Mobile probe output (proportional to $\sigma_{indic\ mobile}$)
Lower trace: Angular orientation transducer output, θ.

we obtained the plots shown in Fig. 5.6. As can be seen in these plots (in which the time sequencing of the points plotted is indicated by the dashed lines and arrows), the indicated conductivity curve does not retrace exactly its original path as θ is swept out to some finite value and then back to zero. There also appears to be a slight asymmetry about the line $\theta = 0°$. Despite these unexplained features, the data seem to be sufficiently repeatable and of sufficient quality to support the conclusion that as the orientation of the pins is changed from $\theta = 0°$ ("end-on" orientation with the pins parallel to the flow) to $\theta = 45°$, the indicated conductivity drops by 20% to 25%, and this decrease appears to be linear in θ, at least to a first approximation.

5.4 Spatial Resolution and Effects of Nearby Conductors

We mentioned in Section 1.3 that the spatial resolution of a four-pin probe depends on the size of the probe. For purposes of defining more precisely what we mean by "spatial resolution", let us suppose that the probe tip is surrounded by a sphere of uniform-conductivity plasma of radius r, and that beyond this radius the conductivity may be different, or there may be conductors or other disturbances. Then if r is the largest radius for which such disturbances produce measurable changes in the conductivity indicated by the probe, we say that the probe has approximately the spatial resolution r. For a four-pin probe it seems plausible that the spatial resolution would be roughly the dimensions of the region through which most of the current between the outer pins flows. For probes constructed such that the dimension ℓ (see Fig. 1.1) is roughly equal to the outer pin separation ($a + b$ in Fig. 1.1), we might anticipate that the spatial resolution would be approximately equal to this outer-pin separation, or perhaps up to twice this value.

Experimentally, the spatial resolution was investigated by traversing the probe radially across the flow in an attempt to measure radial conductivity profiles in the nozzle. Fig. 5.7 shows portions of the stripchart record obtained as the small probe described in Section 5.3 was traversed several times across the flow. There was some problem with thermal warping of the probe, so that there is considerable uncertainty in the actual position of the probe tips in these traverses, particularly as the probe

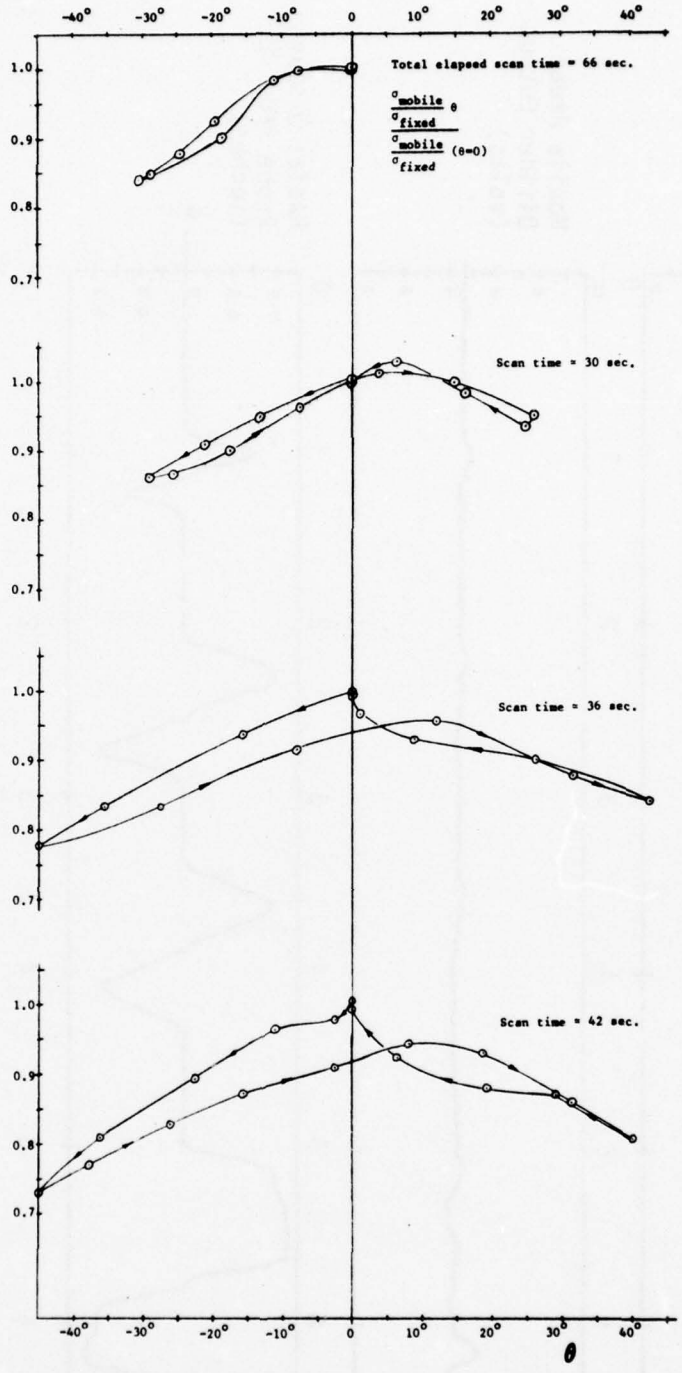


Figure 5.6. Results of θ-scans of 6/1/77 showing variation of indicated conductivity with angle of orientation, θ. The quantity plotted on the ordinate is the ratio

$$\frac{\sigma_{mobile}}{\sigma_{fixed}}(\theta) \Big/ \frac{\sigma_{mobile}}{\sigma_{fixed}}(\theta=0).$$

The top curve shows data from a slow, continuous scan of θ, while the scans in the lower three curves were carried out more rapidly.

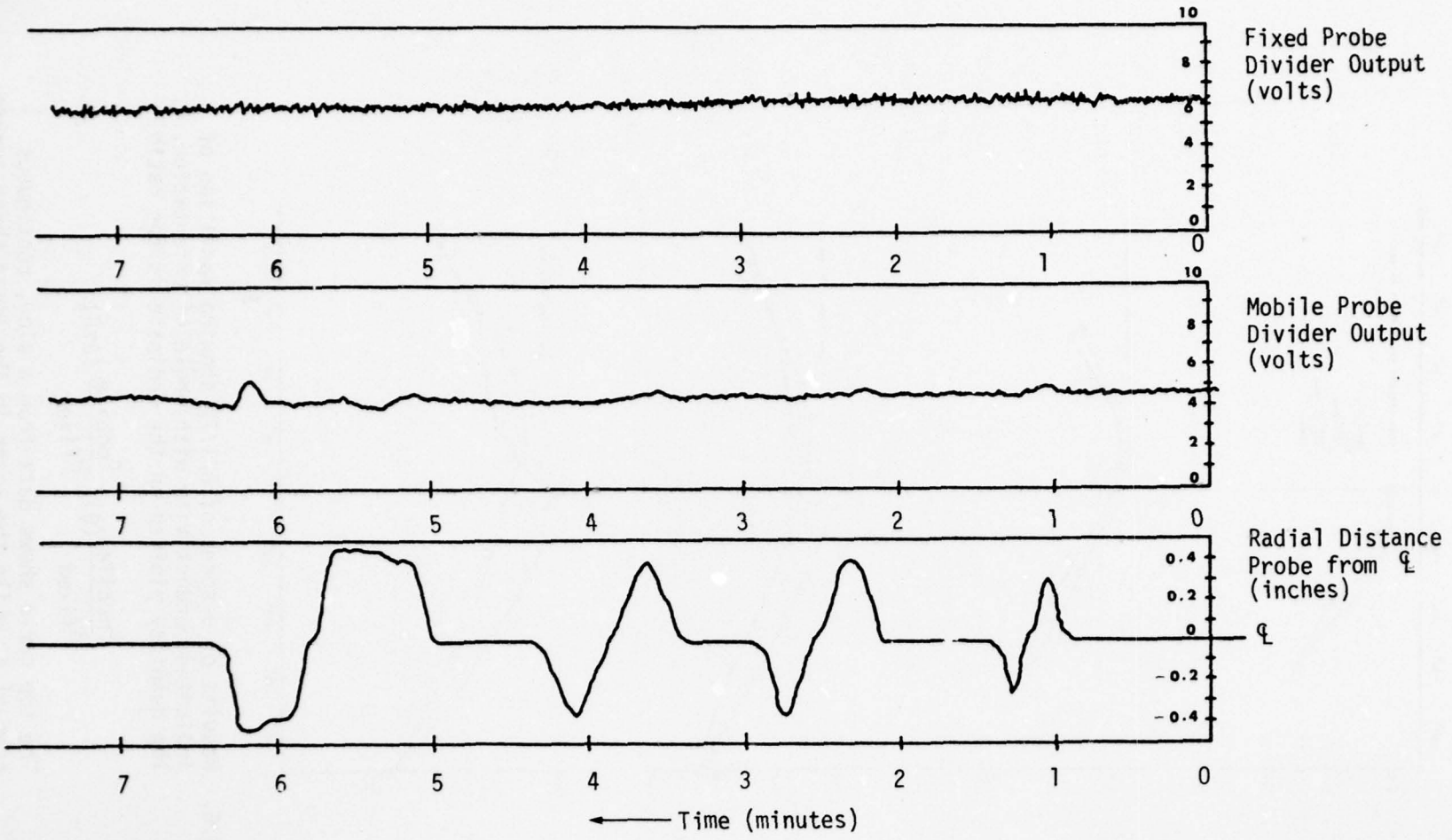


Figure 5.7. Portion of Stripchart of 6/1/77 showing how mobile probe output is only slightly affected by radial transverses of the probe.
Upper trace: fixed probe output
Middle trace: mobile probe output
Lower trace: radial position transducer output

approached the wall where temperature gradients were higher. Nevertheless, the stripchart shows a relatively flat profile, with the indicated conductivity increasing very near the wall.

This effect is seen more clearly in Fig. 5.8, in which the quantity $\sigma(r\neq 0)/\sigma(r=o)$ has been calculated from one of the scans in Fig. 5.7 and plotted vs. r. At distances of about 0.15 ± 0.05 inch from the nozzle wall, the very flat profile of σ_{indic} turns sharply upward, in spite of the fact that the actual local conductivity near the cooler nozzle wall must be decreasing. This effect is thought to be due to a conducting surface layer on the nozzle, and is consistent with the observations of Brown (Ref. [6], p. 176), who found that nearby conducting walls affected the probe current pattern in such a way as to make the indicated conductivity increase. In the present experiments, the conducting layer was probably formed by tungsten carried downstream from the arcjet cathode and reacting with the boron nitride nozzle (such layers have been found to be conducting in previous work at Stanford). Another possible source for a conducting layer would be liquid metal NaK (although the nozzle surface temperature was supposedly kept high enough to avoid NaK condensation, as mentioned in Section 2.2). Some conducting compounds formed by seed deposits from the several preceding tests, which all employed the same nozzle, are another possibility.

If we take as the spatial resolution, r, the distance between the probe and the wall at which the effects of the conducting wall begin to alter σ_{ind} (viz., the figure 0.15 ± .05 inch cited previously), and divide by the separation between the outer probe pins (which was 0.125 ± .03 inch), we obtain the result

$$\frac{\text{spatial resolution, r}}{\text{outer pin separation}} \simeq 1.2 \pm 0.5 \quad ,$$

which is roughly in agreement with our earlier expectation that the spatial resolution of the probe is approximately equal to the outer pin separation.

Some additional modeling of the possible effects of nearby conductors and insulators on the indicated reading of four-pin probes was done using two-dimensional resistance paper ("Teledeltos paper"). The base case was a 34 inch × 34 inch square with insulating boundaries and electrodes painted on with conducting paint (see Fig. 5.9). Successively smaller circles were

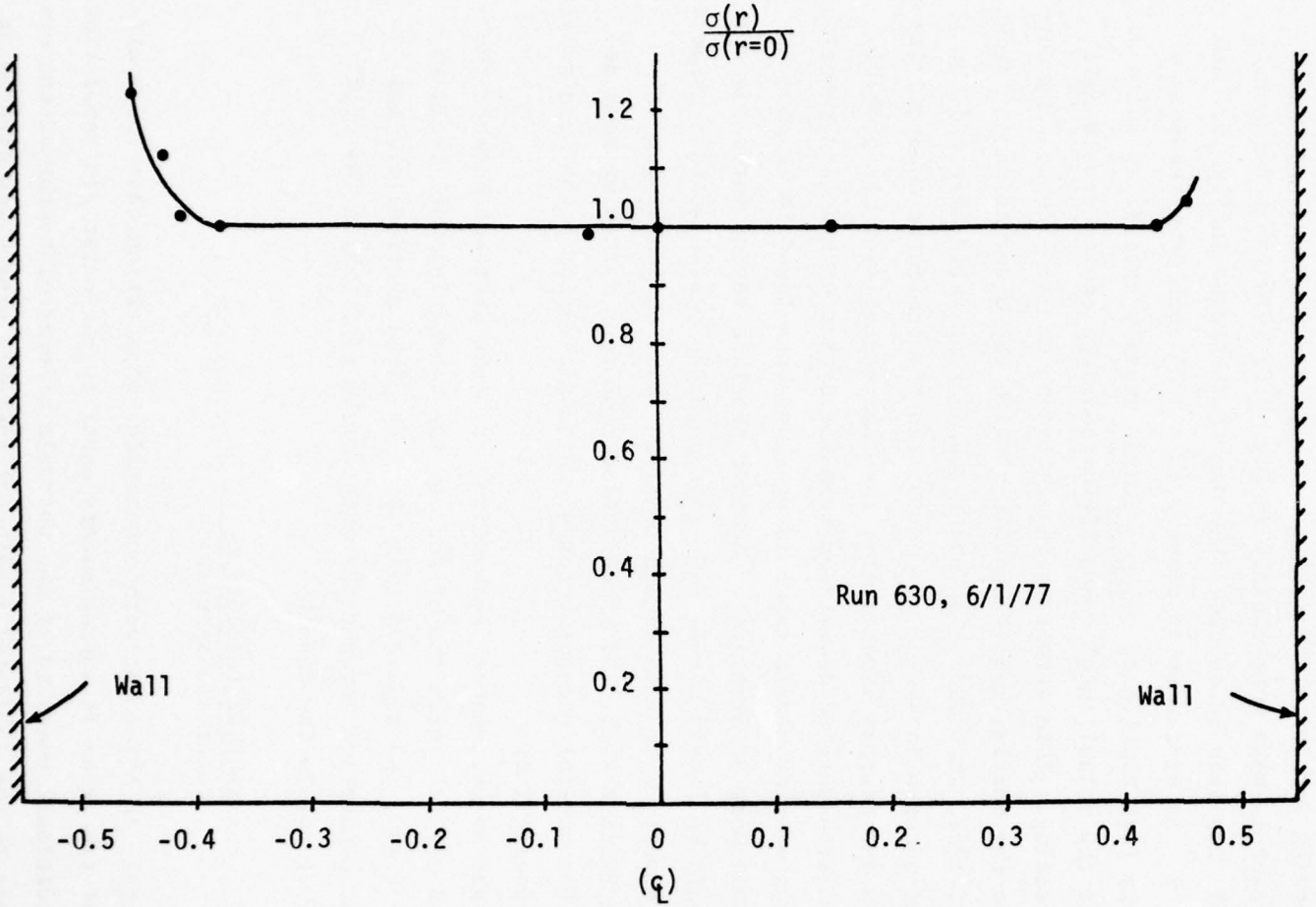
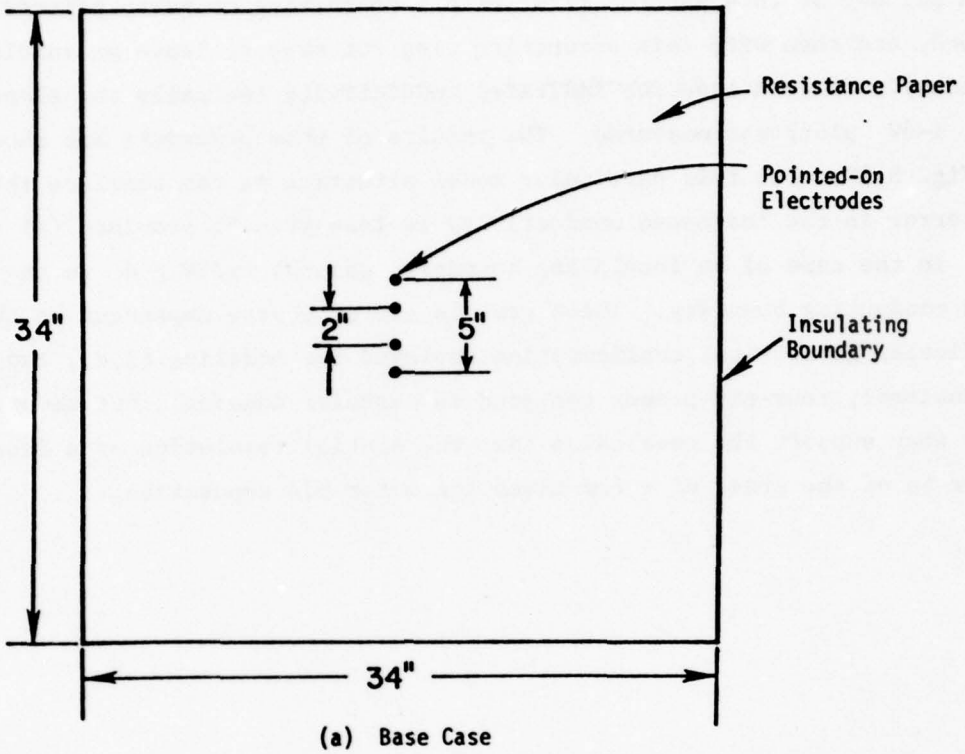
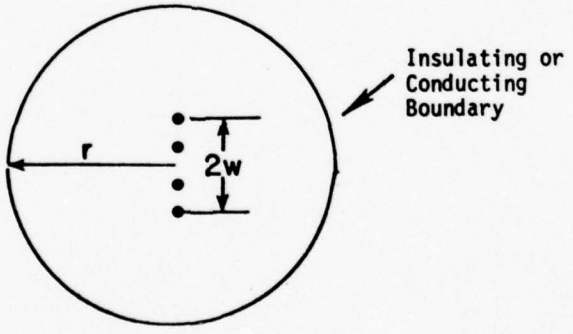


Figure 5.8. Sample radial profile of relative indicated conductivity in the nozzle, as measured by a traversing four-pin probe.



(a) Base Case



(b) Test cases, in which r was varied.

Figure 5.9. Geometry of modelling of the effects of nearby conductors and insulators with two-dimensional resistance paper.

then cut out of this square, first with a conducting boundary painted all around, and then with this conducting ring cut away to leave an insulated boundary. In each case the indicated conductivity (actually the slope of the i-δV plot) was measured. The results of this procedure are shown in Fig. 5.10. For this particular model situation we can conclude that the error in the indicated conductivity is less than 5% provided (a) $r/2W \gtrsim 2$ in the case of an insulating boundary, and (b) $r/2W \gtrsim 4$ in the case of a conducting boundary. These results are of course dependent on the particular geometrical configuration employed for modeling (i.e., two-dimensional, four-pin probes centered in circular domains), but nevertheless they support the conclusion that the spatial resolution of a four-pin probe is of the order of a few times the outer pin separation.

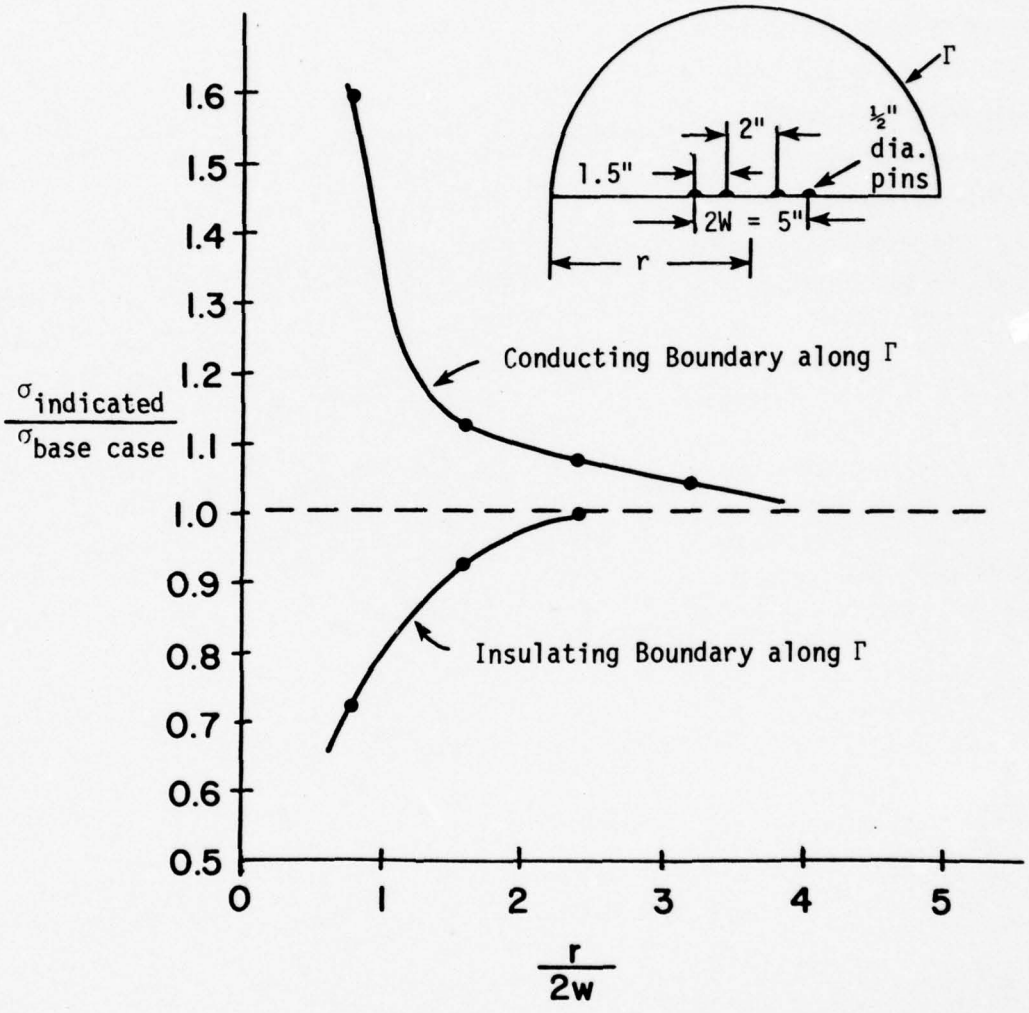


Figure 5.10. Results of two-dimensional resistance paper study of the effects of nearby conducting and insulating boundaries on indicated conductivity from 4-pin probes.

Chapter 6

SAMPLE TIME-RESOLVED CONDUCTIVITY MEASUREMENTS

6.1 Introduction

The purpose of this chapter is to present some sample data taken when the four-pin probe was operated in the time-resolved mode, as discussed in Chapter 4. The data are not interpreted in the present work, but are presented to illustrate the capabilities and type of time-resolved measurements possible with this probe system. Some indication that there were large conductivity fluctuations present in the flow has already been presented in Fig. 4.2, which shows marked changes in the slope of the i-δV characteristics (and hence in σ) during the 1/60th second photographic exposure time, but the data to follow in the next section show the time development of such fluctuations directly, using time-base swept oscilloscope photographs.

6.2 Sample Oscilloscope Photographs

Figure 6.1a shows, in the upper two traces, the waveforms of the amplified i and δV signals as they emerge from the high-pass filters (i.e., at point C in Fig. 4.4). The lower trace shows the voltage between the two outer pins, δV_{outer}. Several features of this photograph are worth commenting upon: (i) Although the applied voltage at the outer pins is sinusoidal (or nearly so), the i and δV signals are clearly distorted into a nonsinusoidal, almost triangular waveform. This effect is not attributable to the signal-processing electronics, since in the corresponding photograph (not included here) of the i and δV signals from the dummy probe (cf. Section 4.3), all the waveforms are sinusoidal. Thus it is suspected that the non-sinusoidal i and δV signals arise from some "real" effect in the plasma. (ii) Despite the difference in waveforms between the δV_{outer} signal on the one hand and the i and δV signals on the other, the i signal does appear to have the same (distorted) waveform as the δV signal, so that the ratio of the amplitudes of these two signals will still be proportional to the slope of the i-δV characteristic,

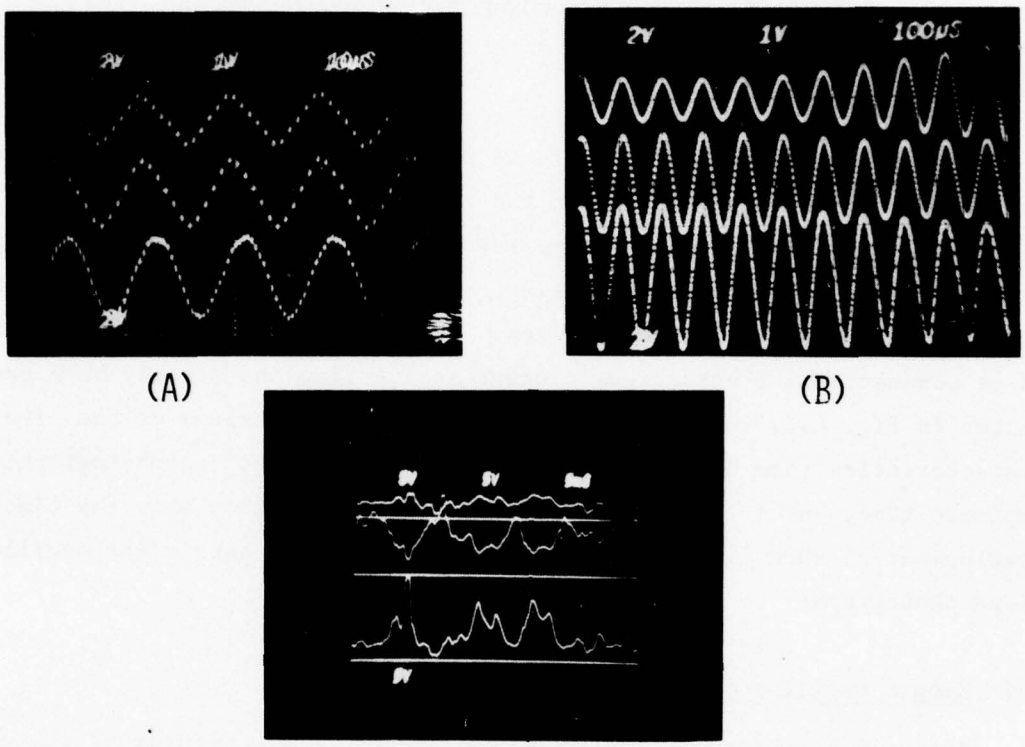


Figure 6.1. Sample Oscilloscope Photographs. (a) and (b), Upper Trace: amplified current signal (2 V/div); Middle Trace: amplified inner pin voltage difference (2 V/div); Lower Trace: outer pin voltage difference (1 V/div).
Photo (a): from mobile probe, Run 90, 3/15/77; sweep speed 10 μsec/div; excitation frequency ≃ 40 kHz;
Photo (b): from fixed probe, Run 130, 2/11/77; sweep speed 100 μsec/div; excitation frequency ≃ 10 kHz (band-pass filter used in place of high-pass filter shown in Figure 4.4);
Photo (c): from fixed probe, Run 410, 3/15/77. Upper Trace (with respect to upper most horizontal baseline, 5-V/div): probe current signal at input to analog divider. Middle Trace (with respect to middle baseline, 5 V/div): inner pin voltage difference signal at input to divider. Lower Trace (with respect to lowest baseline, 5 V/div): analog divider output, proportional to $\sigma(t)$. Sweep speed 5 msec/div in photo (c).

a multiplicative constant, is equal to the plasma's conductivity as a function of time. This photo clearly shows the presence of very large fluctuations in σ in the plenum chamber, where the probe was located. It also gives some idea of the typical time scales of the fluctuations, and demonstrates that the analog divider is working properly.

6.3 Sample Statistical Data on Conductivity Fluctuations

In this section we include some statistical properties of the electrical conductivity fluctuations which were present in the seeded argon flow employed in this research. The procedure used to obtain this quantitative statistical information was first to make analog tape recordings of the processed output signal (proportional to $\sigma(t)$) from each of the four-pin probes (as described in detail in Section 4.2), and then, subsequent to the experiment, to perform numerical computations on these recorded data. The computations were accomplished by first sending the recorded probe output (proportional to $\sigma(t)$) into a Preston GMAD-1 Analog-to-Digital Conversion System, and then using this digital data as input for various statistical programs executed by an HP-2100 minicomputer. The computed results included the following quantities: The mean conductivity, $\overline{\sigma}$; the rms value of the conductivity fluctuations, $\sigma_{rms} = \left[\Sigma(\sigma(t)-\overline{\sigma})^2\right]^{\frac{1}{2}}$; the spectral density function (or "frequency spectrum"); the probability density function (all of these for recordings from individual probes at specific points in the flow); and the cross-correlation coefficient between the outputs of two probes in different locations. In each case the proportionality constant between the conductivity $\sigma(t)$ and the recorded probe output voltage $Q(t)$ was corrected for the effect of velocity according to the procedure described in the preceding chapter (cf. Eqn. (5.5)). This procedure assumes that the velocity-effect correction factor, determined from time-averaged data, remains valid for fast time-resolved measurements also.

Figure 6.2 is a plot of the ratio of σ_{rms} to $\overline{\sigma}$ vs. velocity. This figure indicates that the flow velocity (or alternatively the axial position in the converging nozzle) does not appreciably affect the relative conductivity fluctuation level. In fact, the absolute value of σ_{rms} itself is quite constant for these data, since the corrected mean

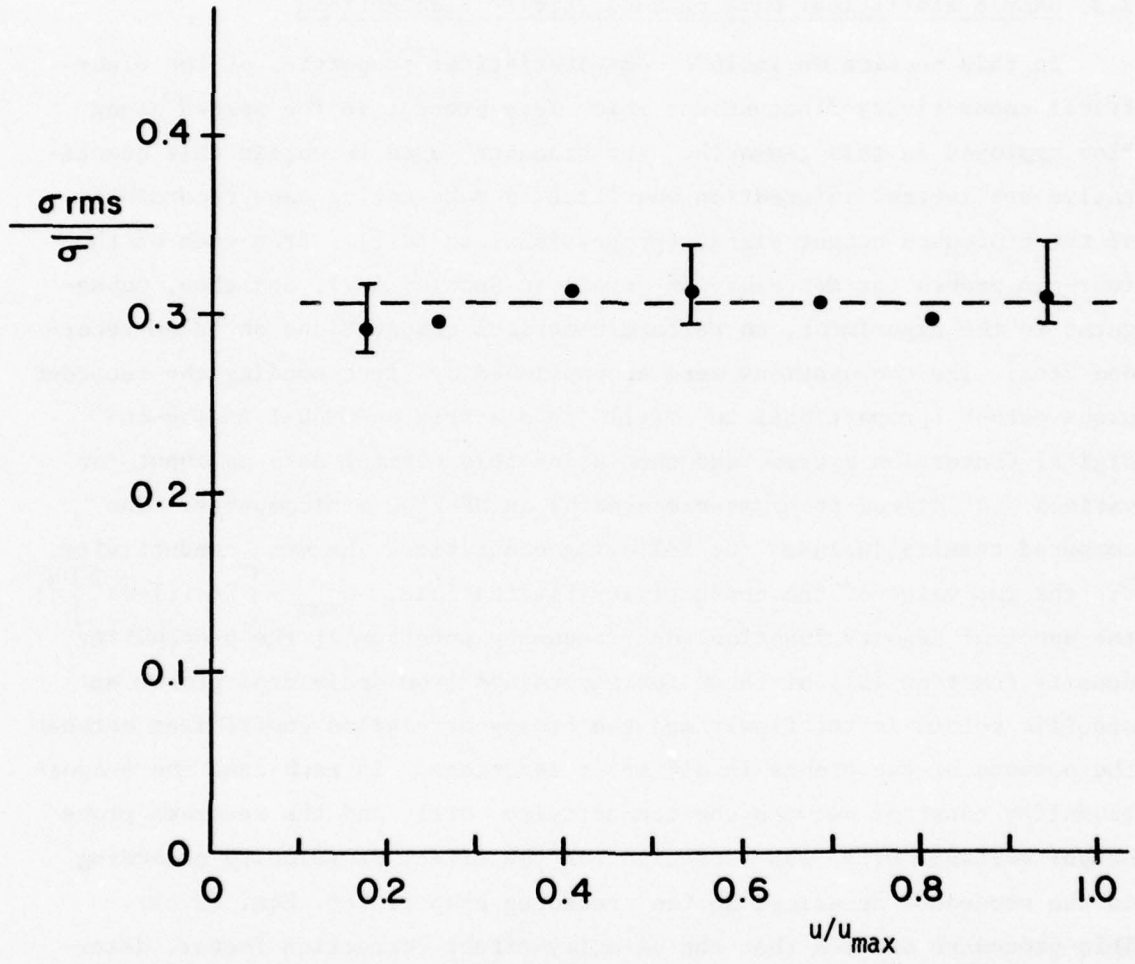


Figure 6.2. Ratio of rms conductivity fluctuations to mean conductivity in arcjet exit nozzle vs. u/u_{max}, from time-resolved 4-pin probe data.

as we require for the signal-processing system to yield an output which is truly proportional to σ. (iii) There is some phase shift between δV_{outer} and the i and δV signals. This is due to the signal-processing components which shift the phase of i and δV by the same amount relative to that of δV_{outer}; the same phase shift occurs when the dummy probe is used. This phase shift causes no difficulties so long as it is the same for both the i and δV signals, as indeed seems to be the case in Fig. 6.1a.

Figure 6.1b displays similar signals as Fig. 6.1a, but from a different test and using a different probe and slightly modified signal-processing components. In particular, in place of the high-pass filter shown in Fig. 4.4, a "high-Q" band-pass filter, tuned to the source excitation frequency, was used. This configuration worked well, but gave the somewhat misleading impression that the i and δV signals were sinusoidal, as was the excitation waveform. In fact, as seen in Fig. 6.1a, this is not the case. The reason for the "sinusoidal-looking" waveforms in Fig. 6.1b is that the band-pass filters attenuate any high-frequency Fourier components of the input waveform, and it is just these higher frequency components which give the waveforms of Fig. 6.1a their "sawtooth" character.

The main reason for including Fig. 6.1b in this report is to illustrate the "slow" changes in the amplitudes (or modulation) of the higher-frequency "carrier" signals, i and δV. This effect is clearly seen in the waveforms of Fig. 6.1b; the modulation is caused by relatively much slower fluctuations in the plasma conductivity which occurred during the one millisecond in which the oscilloscope trace swept across the screen. The same effect is to be expected in Fig. 6.1a, but does not show up so clearly due to the much faster sweep speed employed.

The sample traces shown in Fig. 6.1c are included to convey a visual impression of typical fluctuations in the rectified probe current i, inner pin potential difference δV, and conductivity. The upper trace is the "completely processed" current signal (appearing at point "F" in Fig. 4.4) which is sent to the numerator input terminal of the analog divider; the middle trace is the correspondingly processed δV signal which goes to the denominator input. The lower trace is the divider output, which, aside from

conductivity $\bar{\sigma} \simeq 11.5$ mho/m only varied by less than 10% among the points plotted in Fig. 6.2. One possible explanation which would be consistent with these results is that the regions of nonuniformity in the plasma are simply convected downstream with little diffusion or mixing during the approximately 3 millisecond residence time in the nozzle. If appreciable mixing of the nonuniformities did occur, making the plasma more uniform near the end of the nozzle (i.e., in the high-velocity region), one would expect the ratio $\sigma_{rms}/\bar{\sigma}$ to decrease. The fact that σ_{rms}, computed using the velocity-effect correction factor $f(u)$, does not increase as the gas flows down the nozzle tends to support the interpretation and use of $f(u)$ and the assumption that while $f(u)$ was calculated from time-averaged data it is valid for time-resolved measurements also.

Figure 6.3 shows semi-log plots of the power spectral density function (see, for example, Reference [9]), $G_\sigma(f)$, defined as

$$G_\sigma(f) = \lim_{\Delta f \to o} \frac{1}{\Delta f} \frac{1}{T} \int_o^T [\sigma(t,f,\Delta f) - \bar{\sigma}]^2 \, dt \quad .$$

This quantity represents the Fourier spectrum of the mean square conductivity fluctuation. It is clear from these plots that the dominant contribution to the conductivity fluctuations occurs at frequencies below about 200 Hz, and that there is negligible contribution from frequencies over 2 kHz. The plot shown for the case where the mobile probe was located in the high-velocity region near the nozzle exit lies above the corresponding plot for the low-velocity region. This behavior is generally consistent with the interpretation that the nonuniform regions of fluid are convected downstream past the probes, and that as the fluid moves faster the same nonuniformities give rise to a higher-frequency component in the probe reading. There seems also to be an "extra" very low-frequency component in the signal from the probe when near the exit. This additional low-frequency noise showed up on the eight-channel stripchart as well, and may be due to the close proximity of shear layers and low-frequency vortex-shedding effects at the nozzle exit, whose influence could easily be felt in the subsonic flow at the location of the probe, which was approximately 0.5 cm upstream from the exit plane.

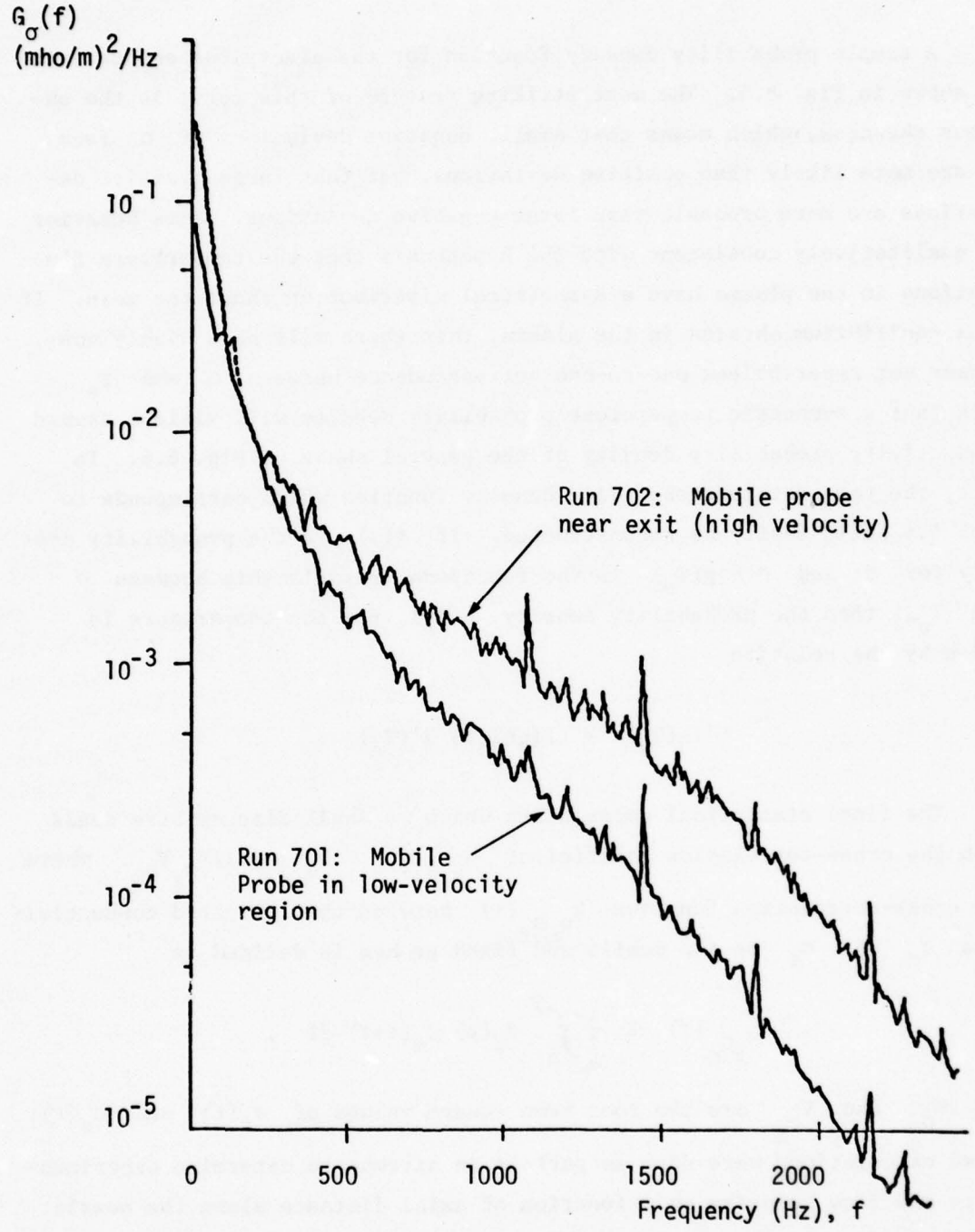


Figure 6.3. Log of spectral density function of conductivity fluctuations vs. frequency from data of 5/27/77.

A sample probability density function for the electrical conductivity is shown in Fig. 6.4. The most striking feature of this curve is the obvious skewness, which means that small, negative deviations of σ from $\bar{\sigma}$ are more likely than positive deviations, but that large positive deviations are more probable than large negative deviations. This behavior is qualitatively consistent with the hypothesis that the temperature fluctuations in the plasma have a symmetrical distribution about the mean. If Saha equilibrium obtains in the plasma, then there will be a highly nonlinear but nevertheless one-to-one correspondence between σ and T_e such that a symmetric temperature probability density will yield a skewed conductivity probability density of the general shape of Fig. 6.4. In fact, the temperature probability density function which corresponds to Fig. 6.4 could easily be reconstructed. If $f(\sigma)$ is the probability density for σ and $\sigma = g(T_e)$ is the functional relationship between σ and T_e, then the probability density $h(T_e)$ for the temperature is given by the relation

$$h(T_e) = f[g(T_e)]\, g'(T_e) \quad .$$

The final statistical calculation which we shall discuss here deals with the cross-correlation coefficient $\rho_{\sigma_m\sigma_f}(\tau) \equiv R_{\sigma_m\sigma_f}(\tau)/V_{\sigma_f} V_{\sigma_m}$, where the cross-correlation function $R_{\sigma_m\sigma_f}(\tau)$ between the indicated conductivities σ_m and σ_f of the mobile and fixed probes is defined as

$$R_{\sigma_f\sigma_m}(\tau) \equiv \frac{1}{T}\int_o^T \sigma_f(t)\, \sigma_m(t+\tau)\, dt \quad ,$$

and V_{σ_f} and V_{σ_m} are the root mean square values of $\sigma_f(t)$ and $\sigma_m(t)$. These calculations were done as part of an attempt to determine experimentally the flow velocity as a function of axial distance along the nozzle. The basic idea of this technique was as follows: With the fixed and mobile probes separated by some known distance, S, the output signals from both probes were simultaneously recorded on the same multi-channel analog tape for a suitable time period (e.g., 30 seconds). From these data the cross-correlation coefficient $\rho_{\sigma_m\sigma_f}(\tau)$ was computed. Assuming that any fluctuations seen by the upstream fixed probe are essentially convected downstream

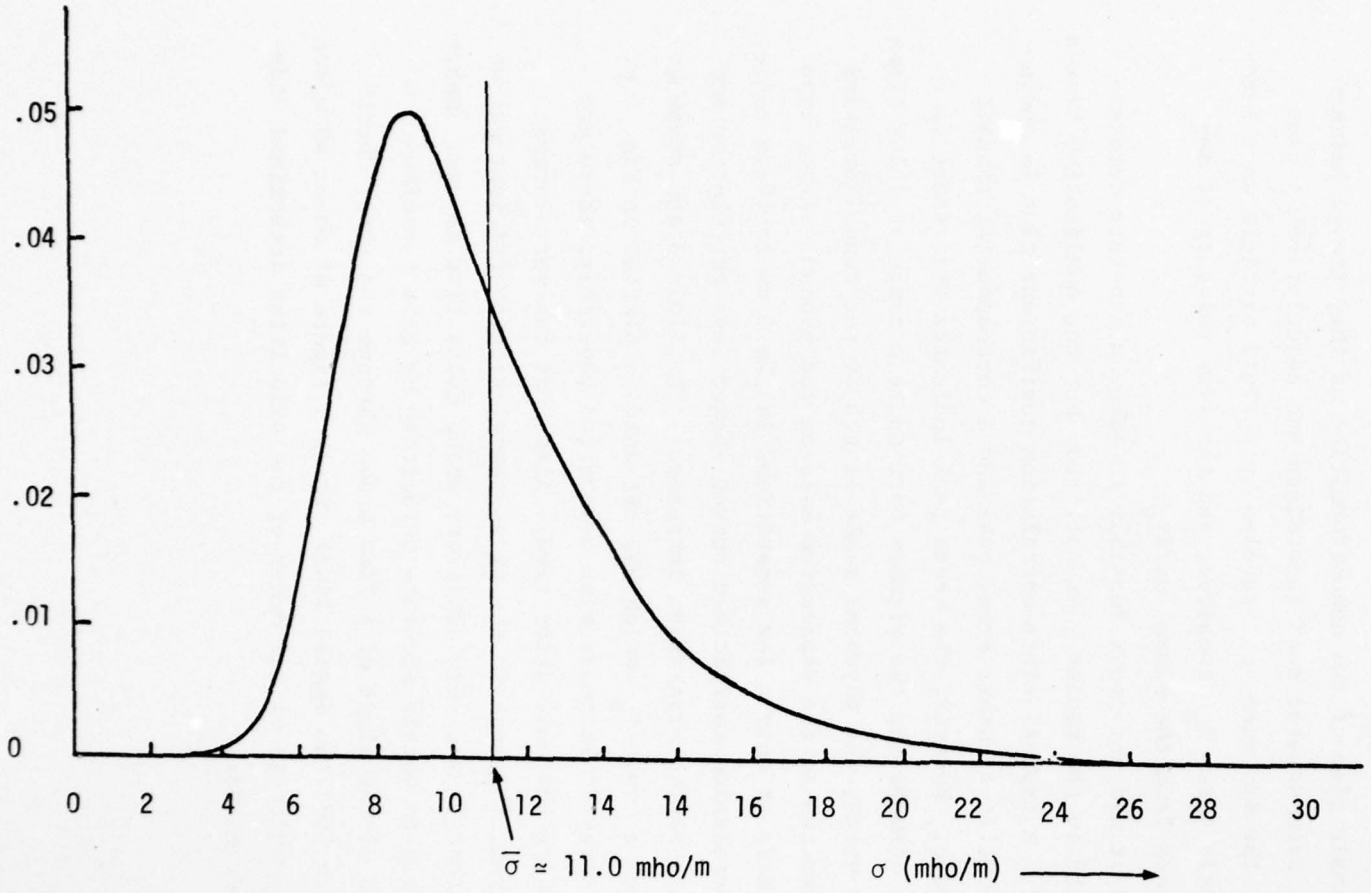


Figure 6.4. Probability density function for electrical conductivity, mobile probe in high velocity region run 102, 5/27/77, $u/u_{max} \simeq 0.94$.

and seen at a slightly later time by the mobile probe, there should be a peak in the function $\rho_{\sigma_m \sigma_f}(\tau)$ for some delay time τ_s, which is equal to the transit time of the nonuniformities as they travel between the two probes. From several such recordings and calculations a plot could be made of the distance s traveled by a fluid particle as a function of the transit time τ_s required, and the flow velocity at any location determined from the slope $ds/d\tau_s$.

In practice it did not prove feasible to make an accurate determination of velocity in the manner just outlined, but the qualitative trends were as expected. A typical cross-correlation coefficient plot is shown in Fig. 6.5. There is a rather broad peak and a corresponding transit time $\tau_s \approx 1.5$ msec. However, the broad peak indicates that there is a high correlation between the two signals over quite a range of delay times τ, or, in other words, the physical scale length of the nonuniformities must be large compared to the separation between the probes. Also, tape recordings were made at only a few separations in the 5 cm to 10 cm range, and the cross-correlation coefficient curves showed less correlation and even broader peaks as the separation increased. The limited and somewhat uncertain data on s vs. τ_s which was obtained is plotted in Fig. 6.6. While the delay times do increase with separation generally, there are three points showing the same delay time. Also, for the very largest separation employed, the peak in the cross-correlation coefficient was so broad and noisy that it was very arbitrary which delay time to use. Hence it was not possible to obtain accurate velocities by this technique. A rough calculation of the slope of a line drawn through the three "best" points in Fig. 6.6 (see the dashed line) yields a figure of about 40 m/sec for the velocity, which is of the order of the velocities determined independently by other means.

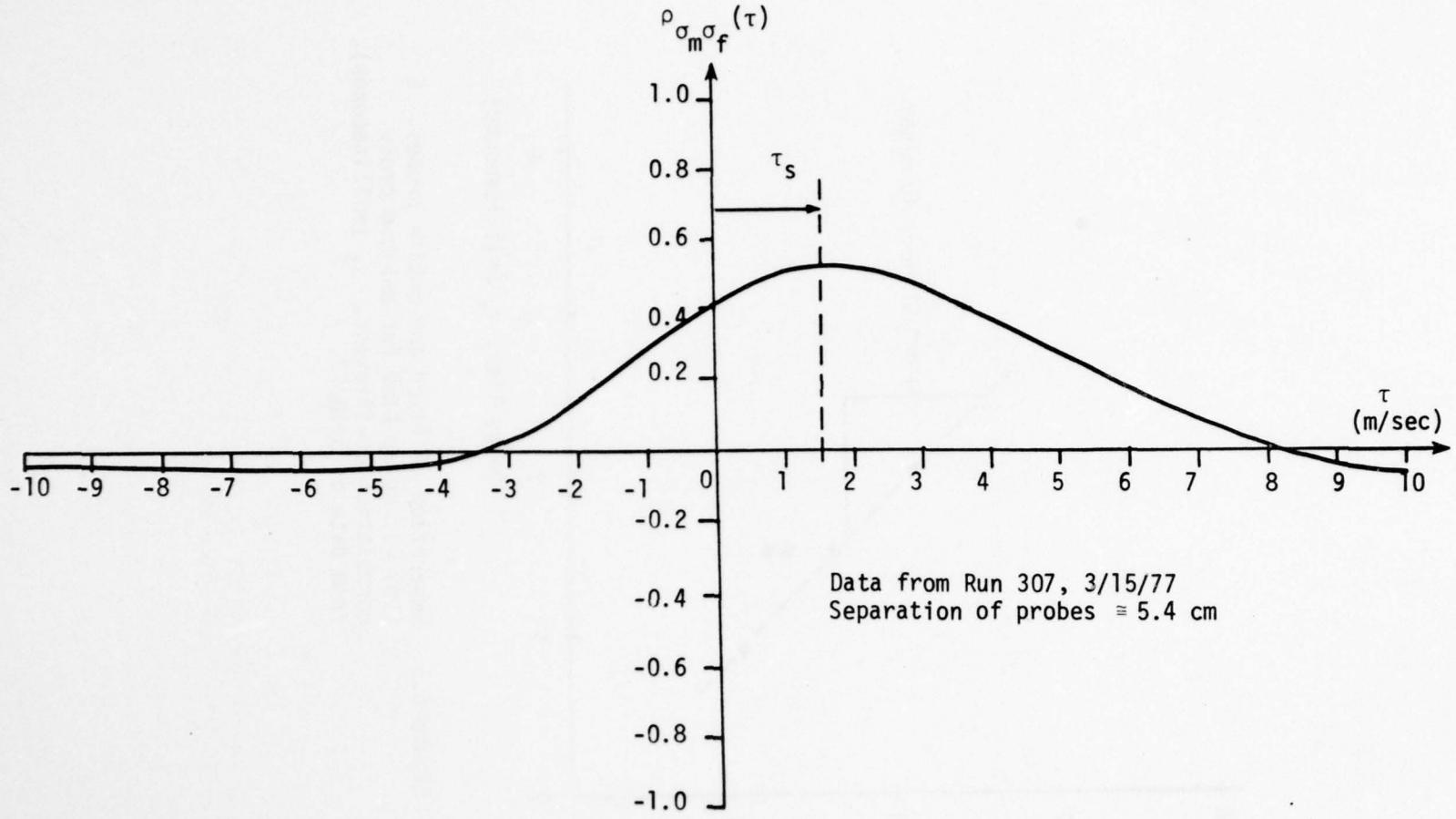


Figure 6.5. Computed cross correlation coefficient between fixed and mobile probe conductivity signals, vs. delay time. Data was passed through low pass filters with cutoff frequency 200 hZ before computing.

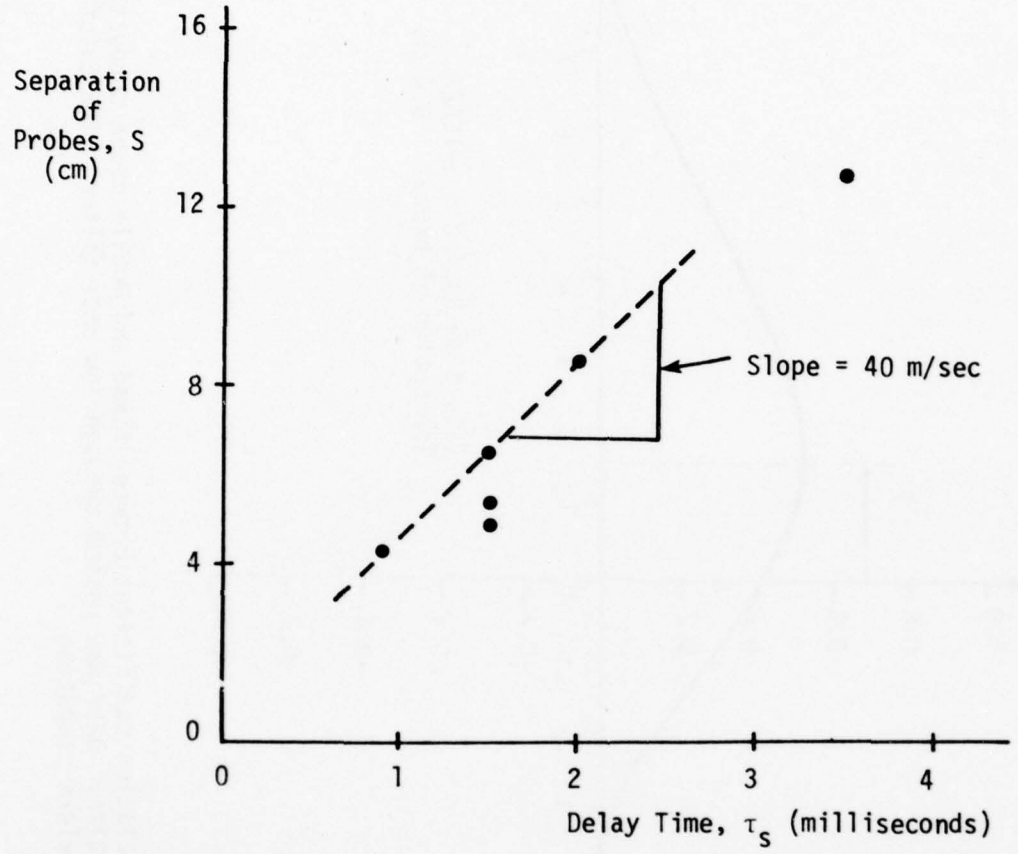


Figure 6.6. Separation of fixed and mobile probes, S (cm) vs. delay time for maximum cross correlation coefficient, τ_s (milliseconds), from data of 3/15/77.

Chapter 7

SUMMARY AND CONCLUSIONS

This report describes an experimental study of four-pin probes as a diagnostic technique for measuring the electrical conductivity of flowing MHD plasmas. Emphasis has been placed on achieving temporal and spatial resolution and on investigating the accuracy of such probes in the presence of possible flow effects.

After a brief account of the theory of operation of four-pin probes, the actual construction of the probes and the relevant features of the arcjet facility used to generate a flowing seeded argon test plasma were described. This was followed by the results of experimental investigations of the i-δV characteristics of the probes, in which the linearity of the characteristics was demonstrated and the existence of a non-zero, fluctuating inner pin voltage difference, δV_{offset}, was discovered. The presence of this δV_{offset} guided the choice, for subsequent experiments, of a.c. probe excitation (at frequencies in the audio range well above the highest fluctuation frequencies present in the flowing plasma) and the development of the final electronic signal-processing system. This system was finally employed in experiments to determine how the indicated conductivity readings from four-pin probes changed with the flow velocity over the pins and with the orientation of the pins with respect to the flow. These experiments also included some analog tape recordings of time-resolved conductivity fluctuations, from which various statistical properties were later deduced.

The major conclusions which we have drawn about four-pin probes as a result of this research are as follows:

- The i-δV characteristics of the probes used remained linear if the amplitude of the a.c. voltage applied to the outer pins was kept below about 1 volt. This criterion seemed to be a more useful rule of thumb for ensuring linearity than some criterion based on the current density at the outer pin surfaces, which varied with probe geometry but was usually less than approximately 0.2 amps/cm^2.

- Even when no current passes between the outer electrodes, a finite and fluctuating voltage difference, δV_{offset}, appears between the inner pins. This fact requires that the probe not be operated with d.c. current if erroneous results are to be avoided.

- When excited at frequencies well above the highest frequency of the naturally occurring conductivity fluctuations in the flow, the four-pin probe system described in this report appears to yield reliable and accurate time-resolved data on conductivity fluctuations. That is, all statistical parameters characterizing the fluctuations are accurate, except possibly the mean value, $\overline{\sigma}$.

- As discussed in Appendix A, the probe constant k_p could only be determined to a precision of approximately 5% to 10% by the method of immersion in KCℓ solutions. This fact limits the probe's absolute accuracy even in the absence of flow effects.

- For a fixed, "end-on" probe orientation, there was a significant decrease in the probe's indicated conductivity as the velocity increased (cf. Fig. 5.3). One way of interpreting these results is in terms of a *velocity-dependent correction* factor to the probe constant (cf. Fig. 5.4). Based on the present measurements, it seems that failure to account for this velocity effect could result in an inferred conductivity as much as two or three times lower than the actual conductivity.

- There is also an effect of the probe pin orientation relative to the flow direction, which manifests itself, for a fixed flow velocity, as a decrease in the indicated conductivity as the pins are rotated from the "end-on" configuration towards a sidewise orientation (cf. Fig. 5.6).

- The following comments can be made regarding the suitability of four-pin probes as a practical diagnostic for MHD work in general. For relative, time-resolved conductivity fluctuations measurements, such probes would seem to be very useful. (No experiments were performed to assess the effect of a magnetic field on four-pin probes, though this would probably complicate matters considerably. Also, materials problems would have to be overcome in the case of higher-temperature, oxygen-bearing, possibly slag-laden combustion flows.) For absolute conductivity measurements (either time-resolved or averaged), relatively large flow effects would appear to limit the accuracy of four-pin probes from a practical standpoint.

Using a particular-sized and -oriented probe, we have found that the flow effects can be compensated for by a suitable, empirically based correction factor. To expect good absolute accuracy from any other probe, of different size, differently oriented, and in different flow conditions would seem to require that flow-effect calibration experiments be carried out on that particular probe also. While this is of course always possible, in practical cases it may not always be feasible or worthwhile.

Appendix A

EXPERIMENTAL DETERMINATION OF PROBE CONSTANT

In this appendix we present some detailed experimental procedures which were found to be necessary in order to obtain reasonably accurate measurements of the probe constants, k_p, for the four-pin probes used in the research reported here. The actual electronics setup used, plus the measurement and data reduction procedures for determining k_p have already been presented in Section 4.4. The material in this appendix, on the other hand, relates mainly to problems arising from the use of a liquid electrolyte (aqueous solutions of KCl) as a calibration medium.

It was immediately apparent from preliminary attempts to calibrate probes in KCl solutions that d.c. excitation of the probe was highly unsuccessful due to gas bubble formation on the electrodes and to the large and unsteady local concentration gradients set up in the electrolyte around the probe pins. Thus, while it was clear that a.c. excitation was required, it was not known at what frequency the probe should be excited. When k_p was measured (as described in Section 4.4) over a range of frequencies, different results were obtained. A variation of about 30% was measured in k_p over the frequency range 100 Hz to 50 kHz, for one particular probe (see Figure A-1).

Further investigation into the electrochemistry of electrolyte solutions revealed that similar problems had been encountered by the original chemical researchers attempting to measure the electrical conductivity of electrolytes to high accuracy. Most of the observed frequency dependence at low frequencies was attributed to the effects of polarization of the electrolyte (such as electrolysis, causing gas bubble deposits which change the effective area of the electrodes), while at higher frequencies (roughly, above 10 kHz) errors due to the capacitative effects of ionic sheaths around the electrodes begin to become appreciable. The standard frequency range for electrolytic conductivity work was in the range of several hundred hertz to several kilohertz. The standard reference for reduction of polarization errors is a classical series of papers in the American Chemical Society Journal (listed in reference [13]) describing the research done by Grinnell Jones and coworkers at Harvard University in the early 1930's.

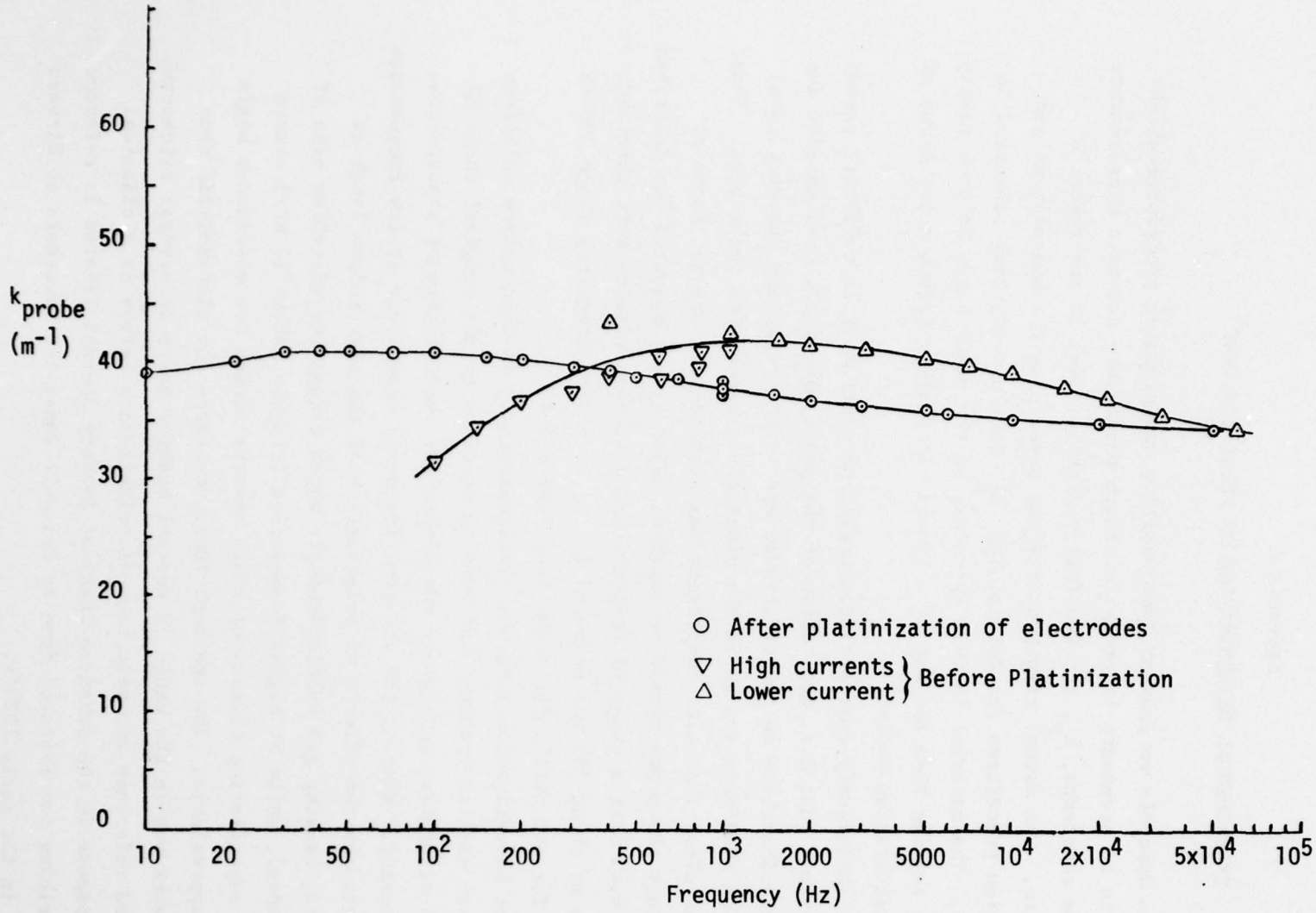


Figure A-1. Probe constant measured in 1 N KCL solution of mobile probe used in test of 3/15/77, before and after platinization of the electrodes, as a function of excitation frequency.

According to [13], polarization errors can be greatly reduced or eliminated by making the electrodes inert and electrochemically reversible, and the standard technique for achieving this is to electroplate the electrodes with very finely divided black platinum particles--a process invented by Kohlrausch in 1897, called platinization. Following the prescription in [13], all four of the probe electrodes were platinized by passing a total charge of at least 1.7 coulombs per cm^2 of electrode area (at current levels about 10 ma) through each electrode while immersed in a platinizing solution of 0.025 Normal hydrochloric acid, 0.3% by weight platinum chloride, and 0.025% by weight lead acetate (The actual solution contained 1 gram $PtCl_4$, 333 cm^3 H_2O, 0.255 cm^3 HCl, and 0.083 gm lead acetate). After platinization, the black-coated pins were very carefully washed in distilled water, and then immersed in the standard 1 Normal KCl solution (prepared by diluting 74.555 gm KCl weighed in air to 1 liter total volume with distilled water); the conductivity of this electrolyte is given as a function of temperature in reference [14].

In addition to platinization of the electrodes, several other more routine precautions were taken. For each measurement of k_p, a beaker of "fresh" KCl solution, taken from the same carefully prepared, sealed reserve supply, was used, and the beaker was sealed off to avoid evaporation of H_2O after the probe was immersed in the solution. An accurate mercury-in-glass thermometer with $0.1^{\circ}C$ graduations was used to monitor the solution temperature. While making the electrical measurements, current was allowed to flow only long enough (typically about 2 seconds) to achieve (and read on a digital voltmeter) a steady divider output voltage, and for all measurements the current density was held to the same value ($\simeq$ 0.2 amps/cm^2 at pin surfaces) by changing the amplitude of the applied a.c. excitation voltage as required.

With platinization (and the above precautions heeded), the measured values of k_p showed a less severe frequency dependence than was obtained without platinizing the electrodes. A comparison of the measured frequency dependence of k_p for one particular probe, before and after platinization, is shown in Figure A-1. The variation of k_p with frequency was never successfully eliminated entirely on any of the probes used, and there was some variability of the severity of the frequency dependence from probe to probe. Generally

the value of k_p at 1 kHz was used to reduce the experimental data on plasma conductivity, but the estimated uncertainty in this value could be as much as 5% to 10%, depending on the probe. The curves of k_p versus frequency for the particular fixed and mobile probes used in the most successful experiments (upon which the important results of Figure 5.3 are based) are shown below in Figure A-2. There was about a 6% reduction relative to the pre-test value in k_p of the mobile probe after it had been used in the experiment, perhaps reflecting some small dimensional changes.

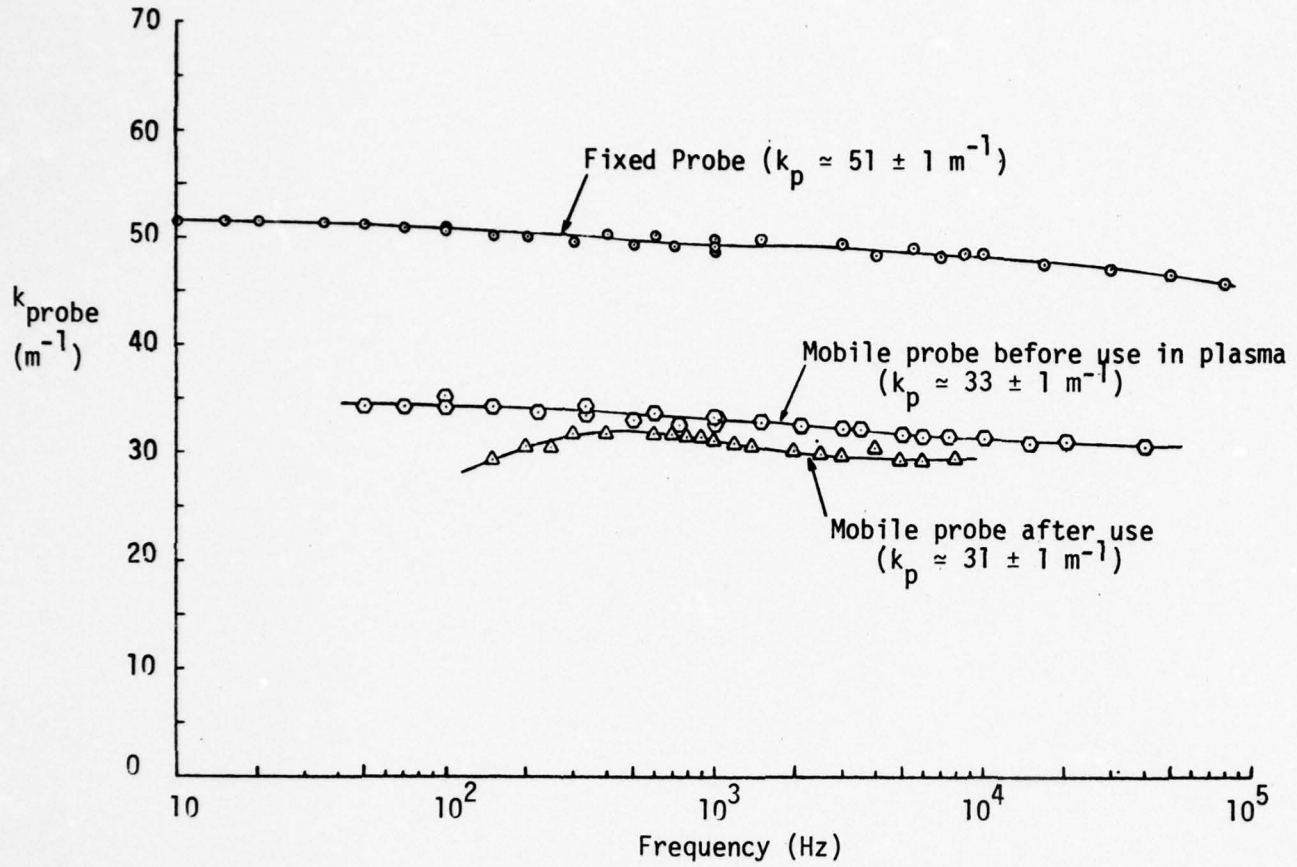


Figure A-2. Probe constants k_p (m^{-1}) as measured in 1 N KCL solution, for the fixed probe (upper curve) and for the mobile probe, before and after use on 5/27/77 (lower curves), as a function of excitation frequency. Probe pins were platinized in each case before measuring k_p.

Appendix B

REDUCTION OF CONDUCTIVITY FLUCTUATIONS INTRODUCED BY ARCJET POWER SOURCE

In the early experiments using four-pin probes in the arcjet facility, oscilloscope photographs of the inner pin voltage difference vs. time showed a repeatable, characteristic pattern of very sharp peaks at a frequency close to 360 Hz. These fluctuations were interpreted as indicating the presence of sharply peaked electrical conductivity fluctuations. It was hypothesized that these σ fluctuations were due to 360 Hz temperature fluctuations probably caused by the "ripple" component of the current supplied to the arcjet by the laboratory's d.c. power supply. This appendix describes how these fluctuations were greatly reduced by employing the large water-cooled MHD magnet as a inductor in series with the arcjet.

The d.c. power source consists of twelve arc welder power supplies (A.O. Smith Co., Model 10,000A) connected as shown in Figure B-1a. The basic wiring diagram for each of these individual units is given in Figure B-1b. This system produces a three-phase, full-wave rectified output voltage waveform whose shape is approximately that obtained by linearly superimposing three full-wave rectified sinusoidal waveforms shifted in phase from each other by 120^{o}, which yields a d.c. output with a 360 Hz "ripple" component whose amplitude is several percent of the d.c. value.

The original connection of this power supply to the arcjet is diagramed in Figure B-2. As can be seen by examination of Figure B-2 and the circuit diagrams of Figure B-1, the current which passes through the arcjet negotiates the complete circuit without encountering resistive or inductive curcuit elements which would tend to impede current fluctuations. Furthermore, the V-I characteristics of a heavy, high-pressure d.c. arc such as exists in the arcjet are almost completely flat (cf. Reference [12], p.365); that is, the voltage drop is determined by the gap length, the gas composition and the gas flow rate through the arc, and is essentially independent of the current level, once the arc has been struck. This fact means that the arc itself will not offer any resistance to fluctuations in the current. Consequently the current through the arcjet will follow the fluctuating emf of the power supply units and will

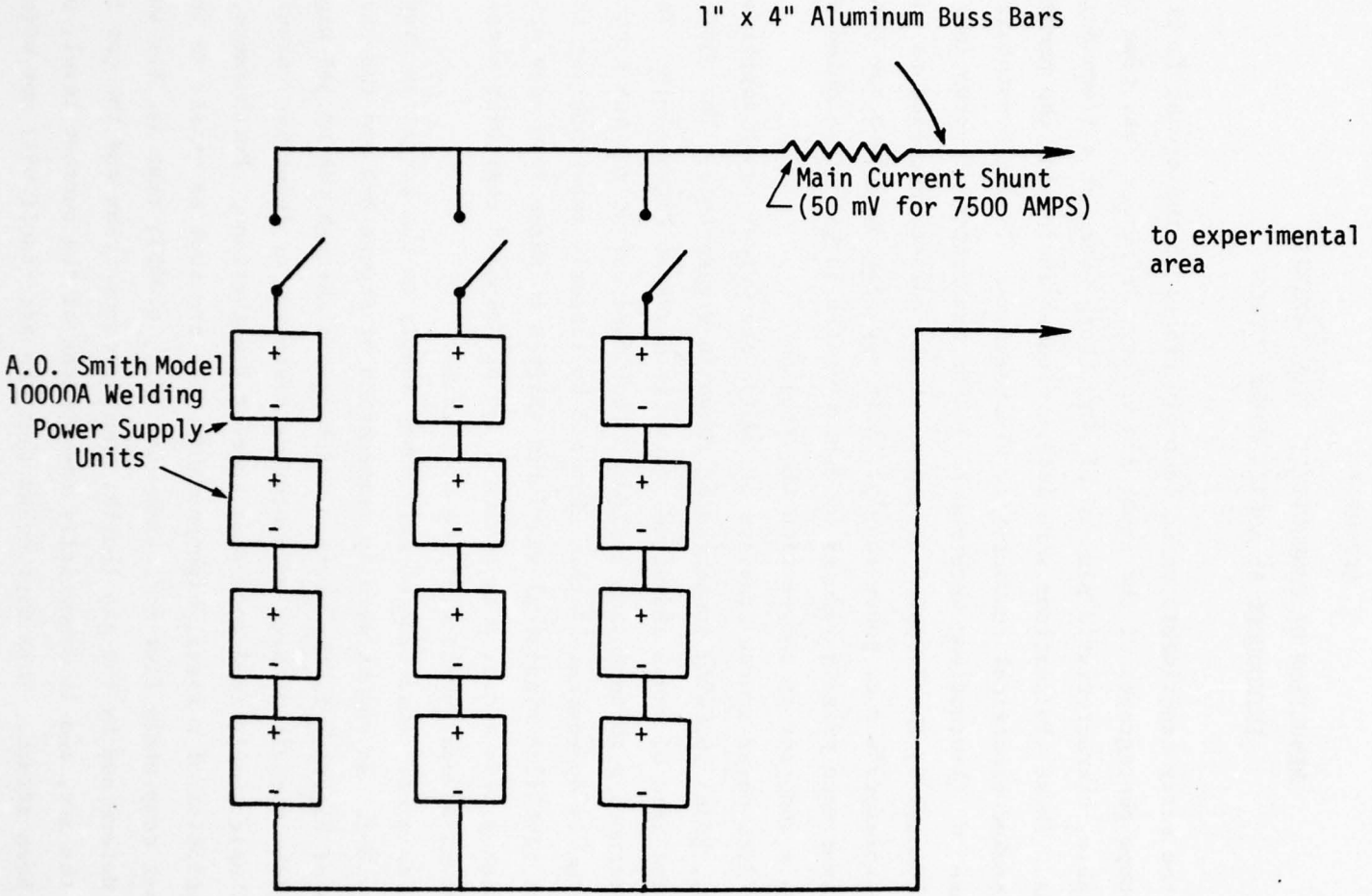


Figure B-1a. Configuration of dc welding power supplies constituting the laboratory d.c. power source.

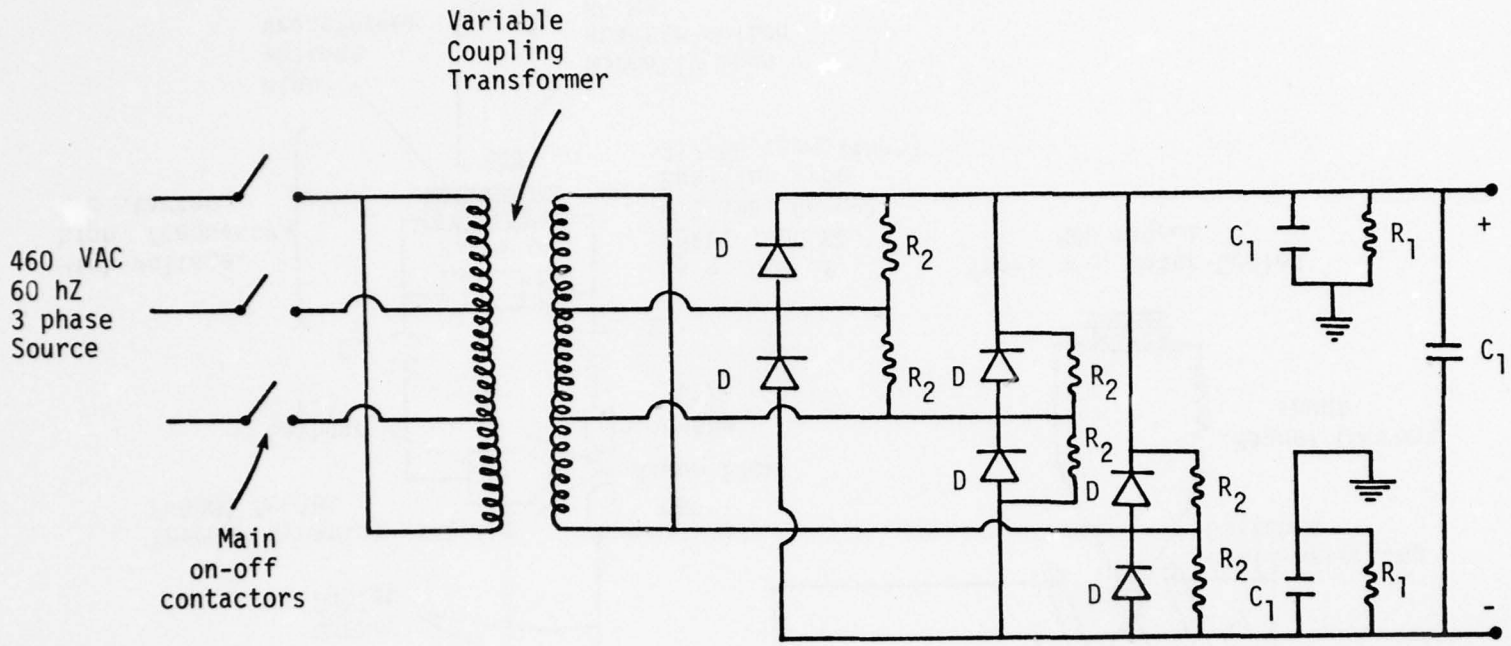


Figure B-1b. Circuit diagram for A.O. Smith Co. Model 10000A Welding Power Supply (80 VDC at open circuit).

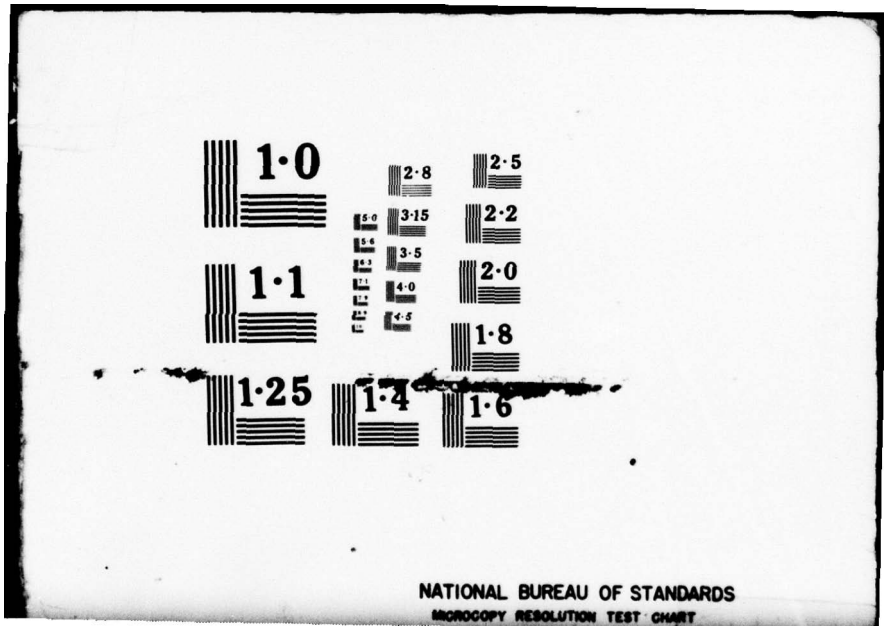
D = Silicon Rectifier 250 A., 300 PIV
C_1 = 5 μf, 400 WVDC
R_1 = 10 KΩ, 5 watt
R_2 = 75 Ω, 10 watt

AD-A055 392 STANFORD UNIV CALIF HIGH TEMPERATURE GASDYNAMICS LAB F/G 20/9
MEASUREMENTS OF ELECTRICAL CONDUCTIVITY OF MHD PLASMAS WITH FOU--ETC(U)
FEB 78 N L HOWER F44620-76-C-0024
UNCLASSIFIED HIGL-108 AFOSR-TR-78-0847 NL

2 OF 2
ADA
055392



END
DATE
FILMED
8-78
DDC


1·0
1·1
1·25
2·8
3·15
3·5
4·0
4·5
5·0
2·5
2·2
2·0
1·8
1·4
1·6
NATIONAL BUREAU OF STANDARDS
MICROCOPY RESOLUTION TEST CHART

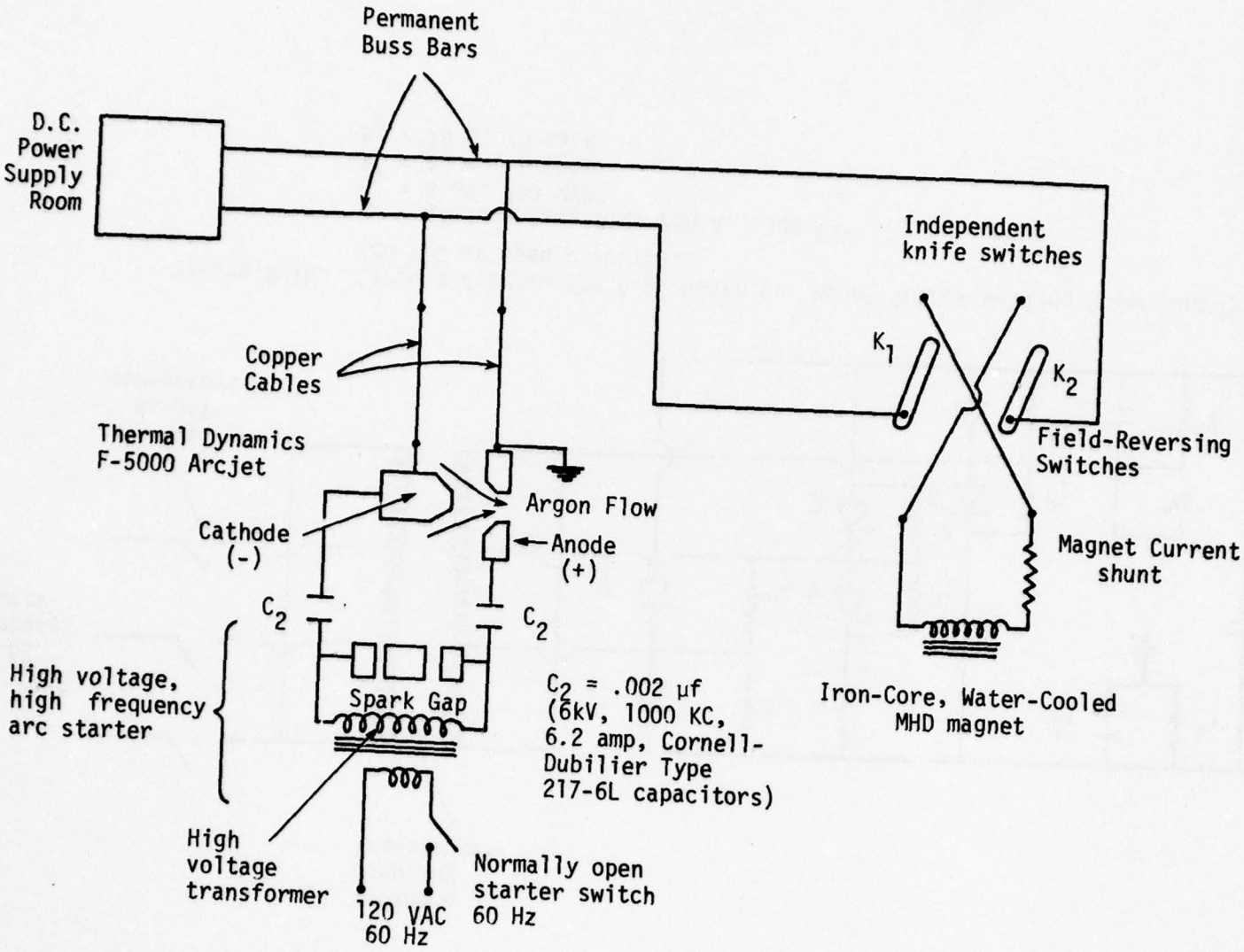


Figure B-2. Connection of Arcjet to DC supply used in original experiments. The knife switches K_1 and K_2 are kept open during operation of the arcjet.

have a fluctuating component at 360 Hz which is several percent of the mean current; this current fluctuation would produce a small 360 Hz gas temperature fluctuation, which would lead to a significant 360 Hz conductivity fluctuation.

The obvious solution to this problem was to place a large inductor, one capable of carrying the full arcjet current (of the order of 10^3 amperes), in series with the arcjet. The inductive impedance ωL would then hopefully be large enough to satisfactorily attenuate the current fluctuations. Fortunately, such an inductor was readily available in the laboratory in the form of a large 2.7 tesla iron-core, water-cooled electromagnet used for MHD experiments.

The inductance L of this magnet was measured using the simple setup shown in Figure B-3. The time response $V(t)$ of the voltage across the known resistor R was recorded on an oscilloscope after closing switch S. Since

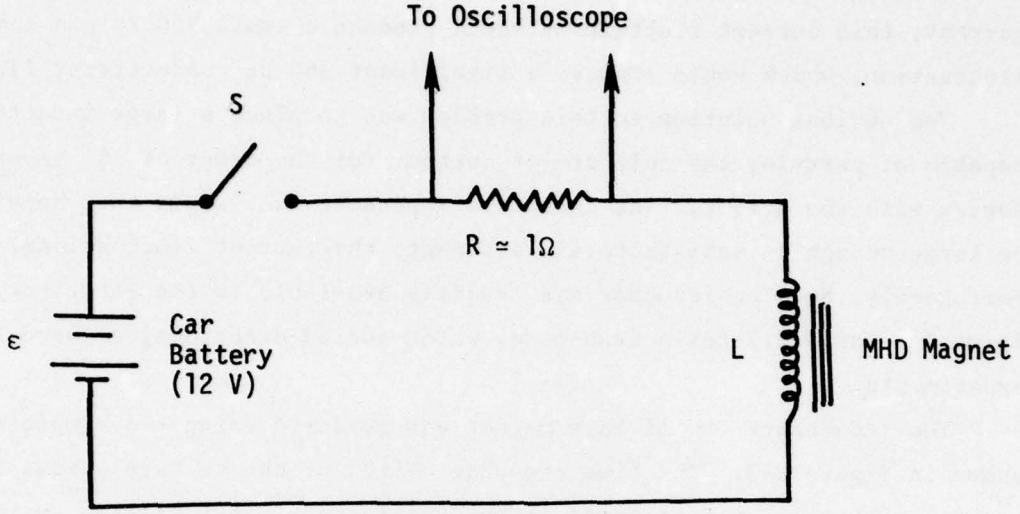
$$V(t) = Vo\left(1 - e^{-\frac{R}{L}t}\right),$$

a plot of

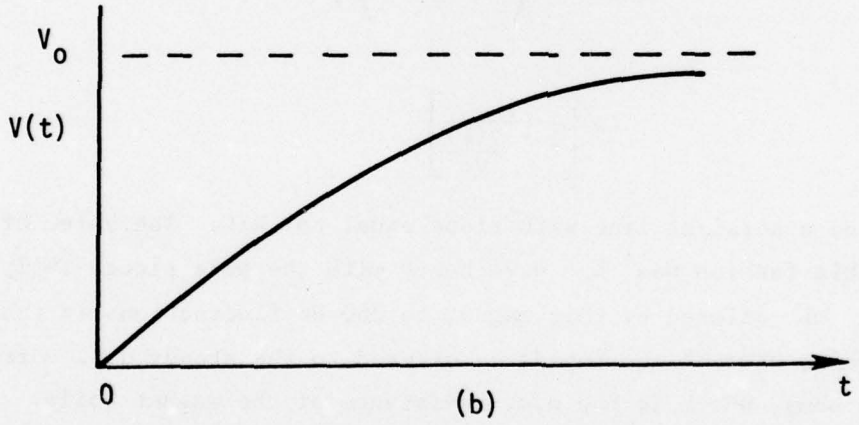
$$\ln\left[\frac{1}{1 - \frac{V(t)}{Vo}}\right]$$

vs. t will be a straight line with slope equal to R/L. The value of L obtained in this fashion was $L \simeq 0.74$ henry with the pole pieces fully closed. The impedance ωL offered by this magnet to 360 Hz fluctuations is thus about 1675 ohms, whereas the impedance offered to the steady d.c. current is only 0.214 ohms, which is the d.c. resistance of the magnet coils.

The magnet (as an inductor) was connected in series with the arcjet as shown in Figure B-4. The diode shown in this figure is a Motorola type MR1269FL silicon power rectifier capable of carrying the full arcjet current in the forward direction. In the event of a sudden extinguishing of the arc for whatever reason, this diode protects the magnet coils from internal arcing due to high $L\,di/dt$ voltages by allowing the stored current to smoothly decay to zero; the stored energy is then dissipated in the ohmic resistance of the water-cooled magnet coils.



(a)



(b)

Figure B-3. (a) Setup for measuring L of MHD magnet, (b) approximate time response of voltage across R.

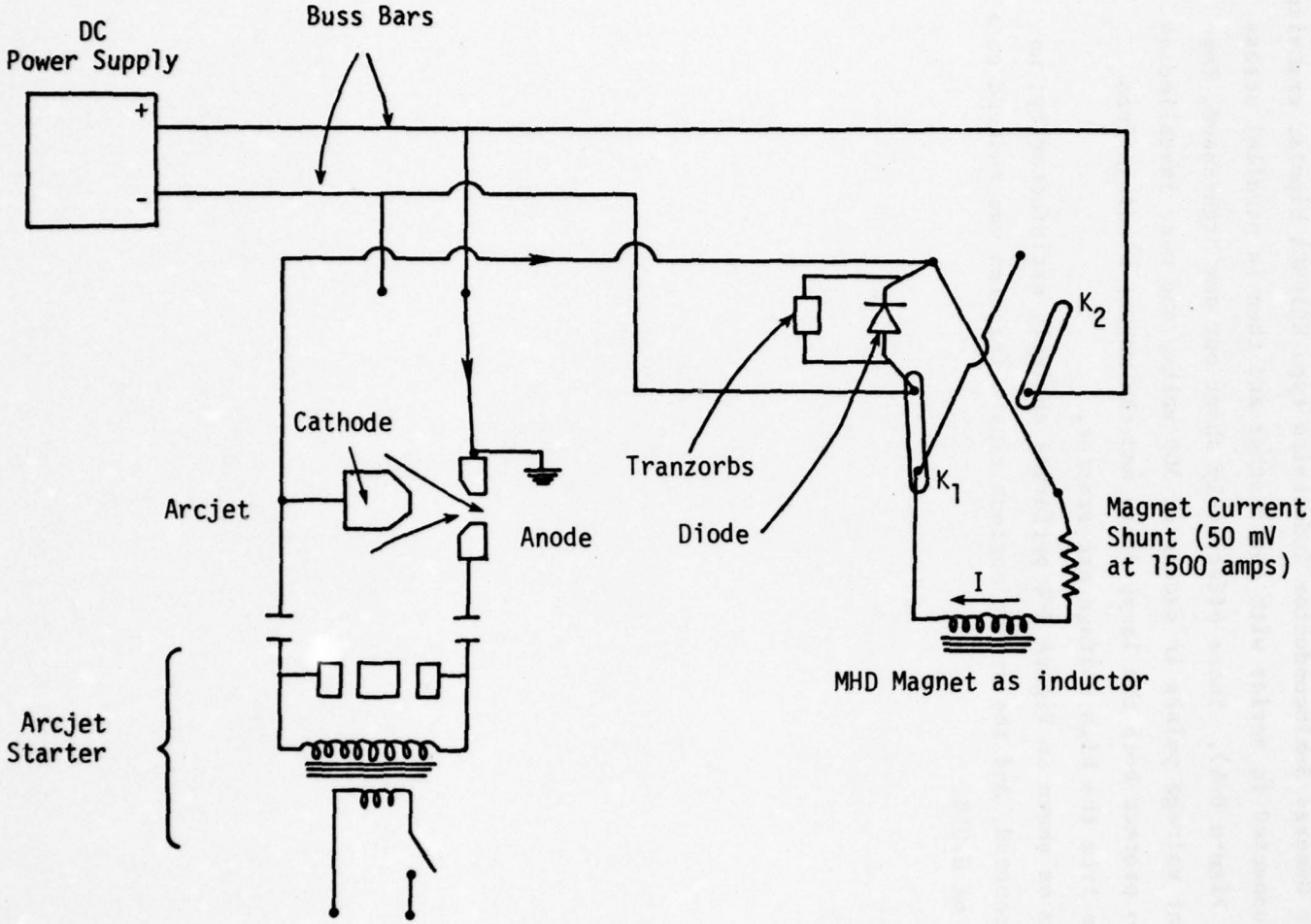


Figure B-4. Connection of MHD magnet in series with the arcjet as an inductor to reduce current fluctuations introduced by the laboratory d.c. supply system.

In addition to the large diode, there are five small "Transzorbs" (trade name for General Seminconductor Industries type KE100CA bipolar transient suppressors) connected in series with one another and then in parallel across the diode (cf. Figure B-4). These effectively short out any high-speed, low-energy transient voltage pulses in excess of 500 volts, and were installed as a precaution to protect both the large diode and the magnet windings from possible damage from the high voltage arc starter.

The system as shown in Figure B-4 performed entirely satisfactorily; no malfunctions occurred, and the arcjet current ripple fraction was reduced to a measured value of 0.01%.

Appendix C

DETERMINATION OF THE FLOW VELOCITY ALONG THE NOZZLE AXIS

The nozzle employed in these experiments was machined from a solid cylinder of boron nitride, and the actual contour was chosen somewhat arbitrarily at the time of machining to provide a smooth, slowly converging shape. Figure C-1 is an approximately correctly proportioned sketch showing the geometrical details of the flow path in the vicinity of the nozzle. The maximum mean velocity, U_{max}, occurs at the minimum-area section at the exit, and is given approximately by the formula

$$U_{max} \simeq \frac{R \dot{m} T}{\hat{M}\left(\frac{\pi d_{min}^2}{4}\right)P} , \qquad (C-1)$$

where R is the universal gas constant, $\hat{M}$ the molecular weight of the gas, $\dot{m}$ the mass flow rate, P the pressure, d_{min} the minimum diameter of the nozzle, and T the gas temperature. For argon at one atmosphere pressure and 2200°K (a typical estimated gas temperature in these experiments), and with $\dot{m} = 0.03$ lbm/sec and $d_{min} \simeq 1.1$ inch (used in all experiments), formula (C-1) yields a value $U_{max} \simeq 100$ m/sec. This value leads to a Mach number less than about 0.1, which means that for purposes of determining the flow velocities along the nozzle axis, negligible error is made by assuming the flow to be incompressible. The remainder of this appendix describes briefly the three methods used to estimate $U(z)/U_{max}$ as a function of the distance z along the axis from the exit plane. The resulting three curves of $U(z)/U_{max}$ vs. z are shown superimposed in Figure C-2.

The first and simplest method was to make the approximation that the flow (in addition to being inviscid and incompressible) was strictly one-dimensional, in which case we obtain from the continuity condition the result

$$U(z)/U_{max} = \left(d_{min}/d(z)\right)^2 . \qquad (C-2)$$

The diameter $d(z)$ was carefully measured as a function of z by mounting the nozzle on the table of a vertical milling machine and tracing the contour

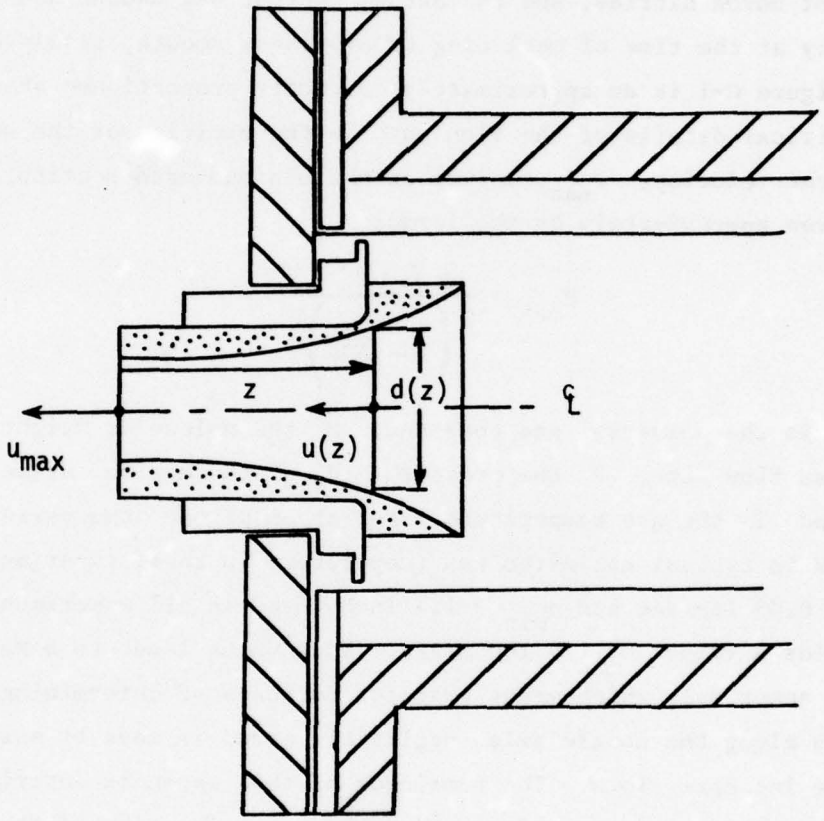


Figure C-1. Sketch defining geometrical variables in the vicinity of the nozzle.

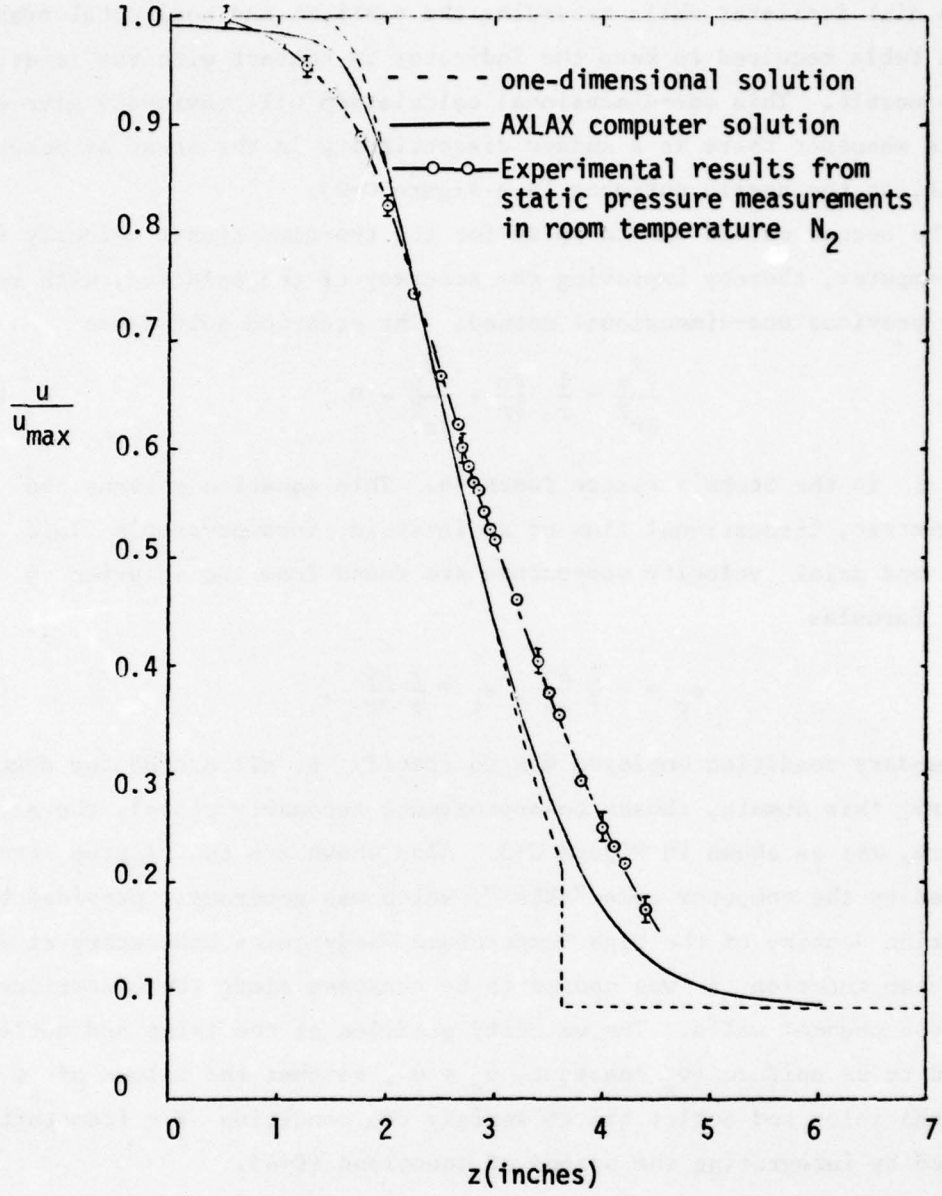


Figure C-2. Centerline velocity ratio u/u_{max} vs. axial distance, z, into nozzle from the exit plane, as determined by three methods.

with a dial indicator while recording the vertical and horizontal translations of the table required to keep the indicator in contact with the inner surface of the nozzle. This one-dimensional calculation will obviously give erroneous results whenever there is a sudden discontinuity in the area, as occurs, for example, at the nozzle entrance (see Figure C-2).

The second method was to solve for the two-dimensional velocity field on a computer, thereby improving the accuracy of the solution, with respect to the previous one-dimensional method. The equation solved was

$$\frac{\partial^2 \psi}{\partial r^2} - \frac{1}{r} \frac{\partial \psi}{\partial r} + \frac{\partial^2 \psi}{\partial z^2} = 0 \ , \qquad \text{(C-3)}$$

where ψ is the Stoke's stream function. This equation governs the axisymmetric, irrotational flow of an inviscid, incompressible fluid. The radial and axial velocity components are found from the solution ψ according to the formulas

$$v_r = - \frac{1}{r} \frac{\partial \psi}{\partial z} \ , \ v_z = \frac{1}{r} \frac{\partial \psi}{\partial r} \ . \qquad \text{(C-4)}$$

The boundary condition employed was to specify ψ all around the domain boundary; this domain, chosen to approximate resonably closely the actual flow geometry, was as shown in Figure C-3. Also shown are the plotted streamlines obtained by the computer code "AXLAX", which was generously provided by Mr. Marion Jenkins of the High Temperature Gasdynamics Laboratory at Stanford. The stream function ψ was chosen to be constant along the centerline and along the channel walls. The velocity profiles at the inlet and outlet were assumed to be uniform (v_z constant, $v_r = 0$), so that the values of ψ specified along the inlet and outlet had to satisfy the condition Ψ = (constant) r^2, obtained by integrating the second of equations (C-4).

As seen from Figure C-2, the results of the two-dimensional numerical solution are in fairly close agreement with the one-dimensional results except near the ends of the nozzle, where the former results appear more realistic. The main limitations of the numerical method are its failure to account for visous effects, compressibility effects, the presence of swirl (non-zero v_θ), the possibly non-uniform inlet and exit velocity profiles, and the lack of complete geometrical identity between the actual flow region and the domain used for the numerical solution.

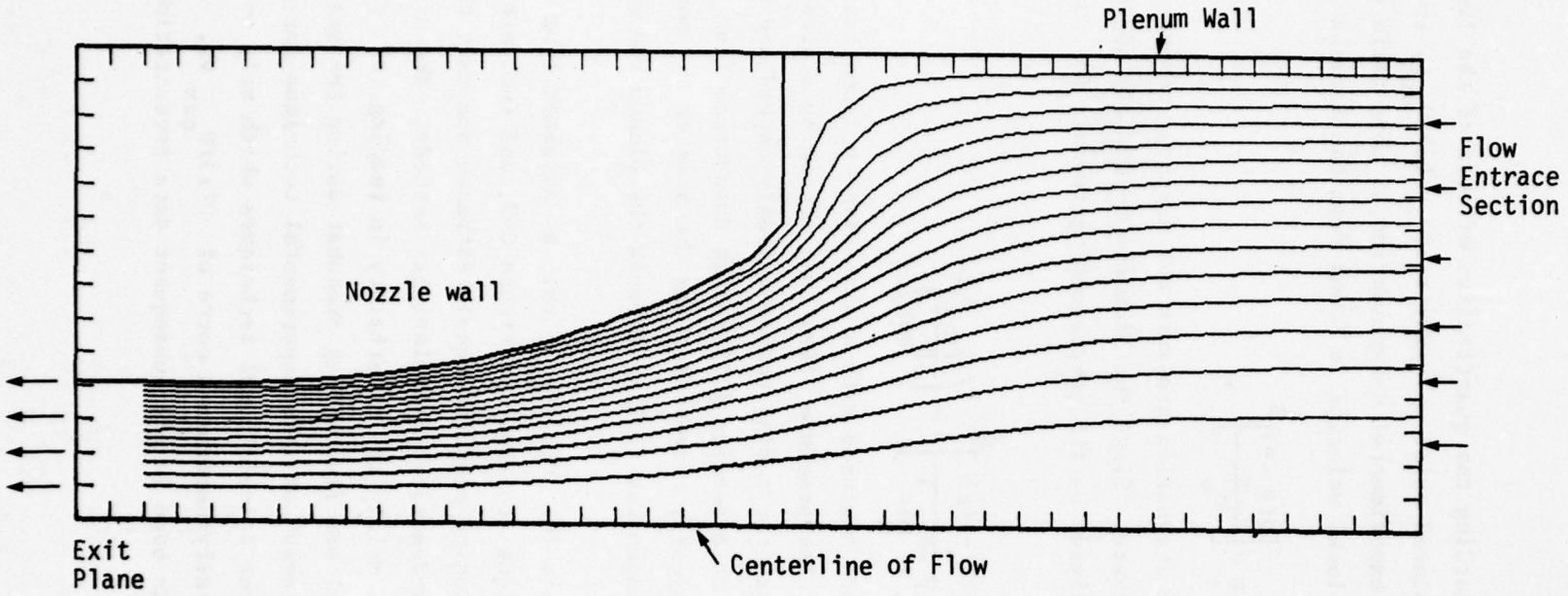


Figure C-3. Domain used in AXLAX computer calculations showing streamlines obtained using uniform velocity profiles at entry and exit.

Due to uncertainty regarding the quantitative effects of the limitations just mentioned on the calculated axial velocity ratio $U(z)/U_{max}$, it was decided to obtain a direct experimental determination of this ratio using a Pitot pressure probe. The local velocity is found from the formula

$$U = \left[\frac{2(P_o - P)}{\rho_o}\right]^{\frac{1}{2}},$$

where P_o and ρ_o are the stagnation pressure and density, respectively, and P is the local static pressure. Since the flow can be closely approximated as incompressible, we may divide by the corresponding formula for U_{max} to obtain

$$\frac{U(z)}{U_{max}} = \left[\frac{(P_o - P(z)}{P_o - P_{min})}\right]^{\frac{1}{2}} = \left(\frac{\Delta P(z)}{\Delta P_{max}}\right)^{\frac{1}{2}} \qquad \text{(C-5)}$$

The pressure differences were measured with a sensitive inclined manometer set up as shown in Figure C-4. The pressure $P(z)$ was sensed by a probe constructed from 3/32-inch diameter tubing hemispherically capped and drilled with four 0.020 inch holes at a section 1.25 inches downstream from the capped end. This probe was mechanically traversed along the axis of the nozzle while room temperature nitrogen was flowing through the plenum and nozzle with a maximum Mach number of 0.1.

The experimental results for $U(z)/U_{max}$ vs. z obtained from this static pressure measurement technique are shown on Figure C-2, and indicate a slightly more gradually-changing velocity near the nozzle entrance and exit than is predicted by the previously-described calculational methods. The error bars shown in Figure C-2 reflect mainly the uncertainty in reading ΔP from the manometer, whose fluid level was fluctuating somewhat during the measurements. Due to the relative "directness" of this experimental technique for determining $U(z)/U_{max}$, as opposed to the calculational techniques which rely on many assumptions, the experimentally-determined curve of $U(z)/U_{max}$ vs. z was deemed more accurate and was used in all subsequent data presentations.

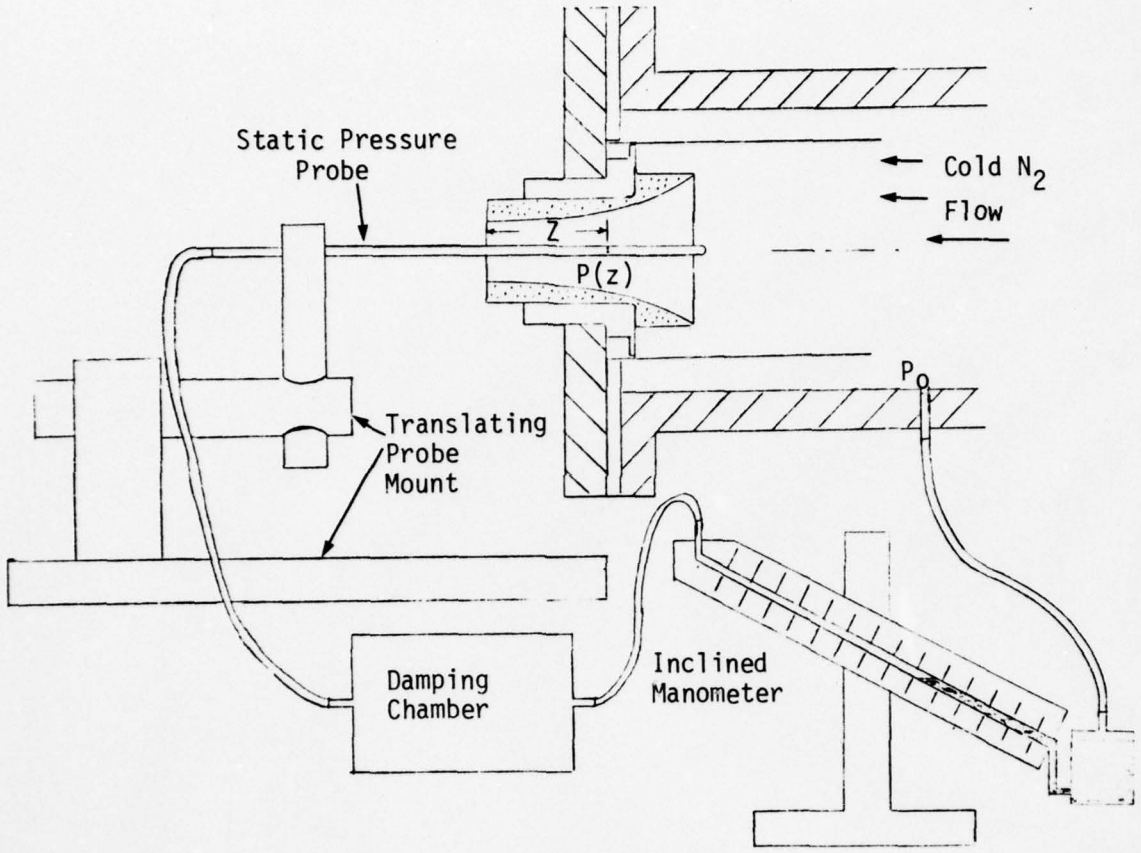


Figure C-4. Experimental setup for determining $u(z)u_{max}$ along nozzle axis.

Appendix D

DETAILS OF FOUR-PIN PROBE EXCITATION AND SIGNAL PROCESSING CIRCUITRY

This appendix consists of a set of wiring and circuit diagrams for the probe excitation circuitry and for the signal conditioning equipment employed.

The probe excitation circuitry consisted of two units: a floating function generator(constructed from a kit, shown in Figure D-2) to provide a low-power excitation voltage, and a floating power amplifier (shown in Figure D-1) designed to amplify the excitation signal supplied by the function generator to power levels sufficient to drive reasonably large currents between the outer probe pins. This combination of equipment permitted exciting the probes over the frequency range 0.1 Hz to around 100 kHz.

A single unit (the "signal conditioning unit") was constructed to accomplish most of the signal processing which is indicated in block form in Figure 4.4 and 4.6. After this signal conditioning unit was constructed, several additional commercial differential amplifiers and electronic filters were acquired, and these were used, together with several of the circuits in the existing signal conditioning unit, to form the final electronics setup used in the experiments. This final setup is shown schematically in Figure D-3.

Figure D-4 shows the chassis wiring of the signal conditioning unit itself. The remaining figures, D-5 through D-10, are detailed circuit diagrams of the individual units (differential amplifier, low-pass filter, precision linear rectifier, fixed- and variable-gain amplifier, and polarity inverter) which are contained within the signal conditioning unit. The analog divider is mounted in this unit also, but since it is a commercially available device (Analog Devices, Inc., Model 436B, Two-Quadrant Divider), no circuit diagram is included here.

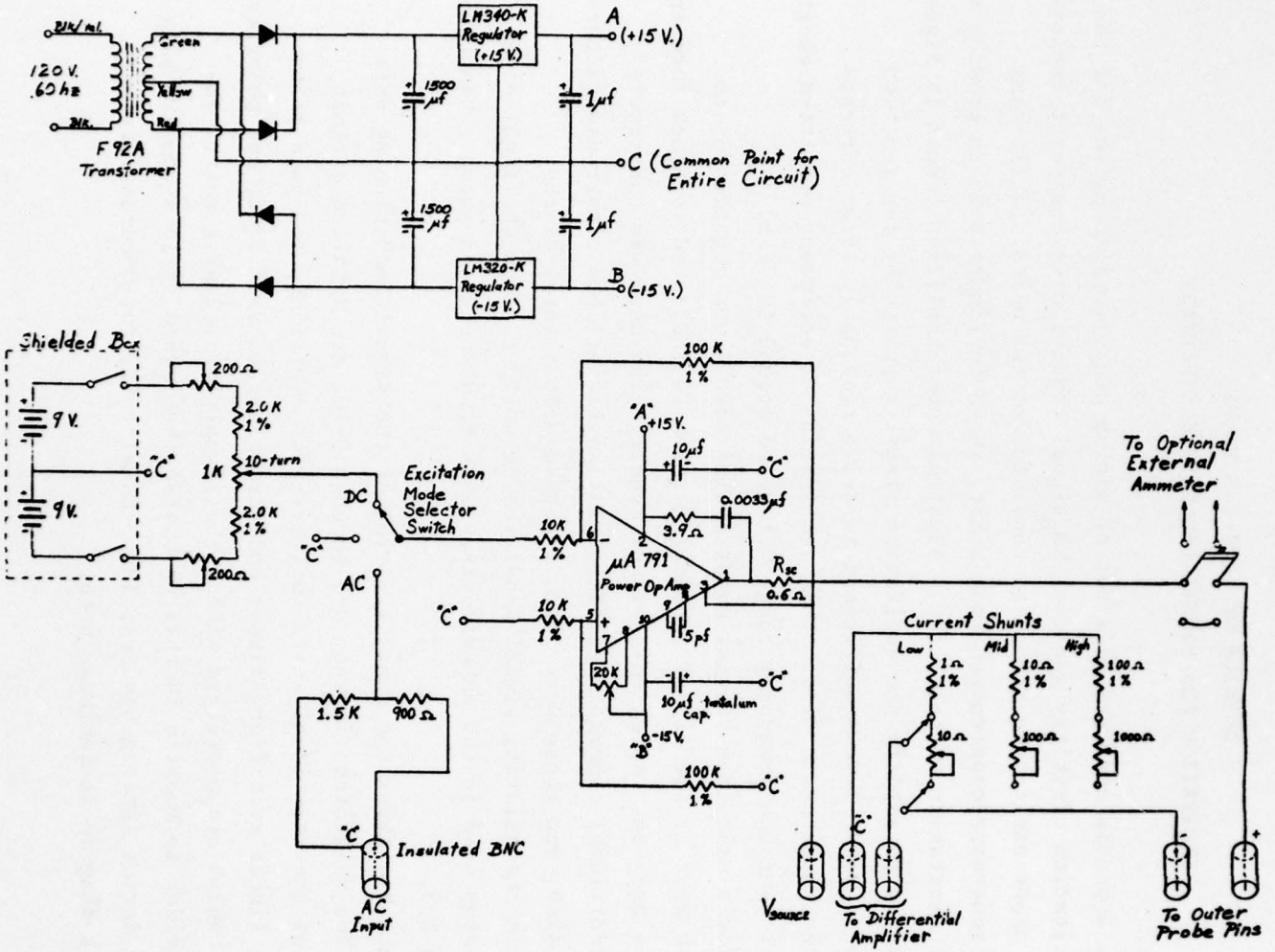


Figure D-1. Floating Power Amplifier used to excite four-pin probes.

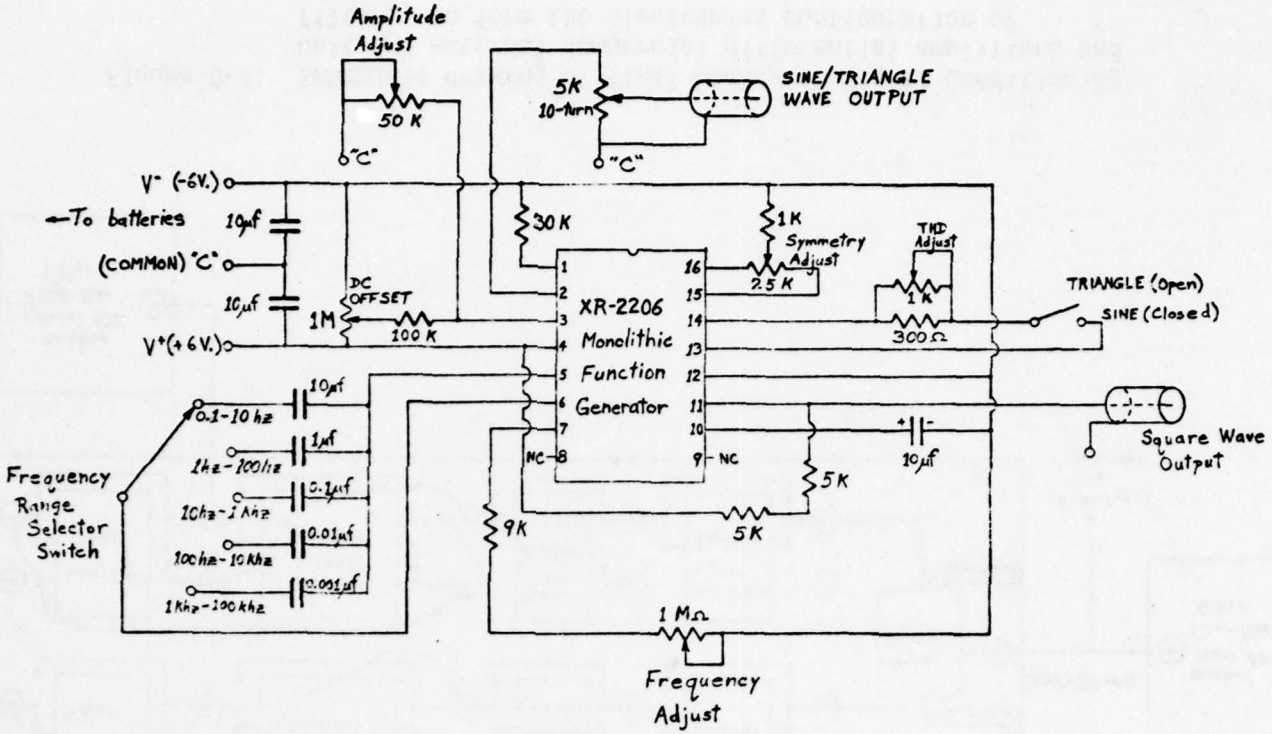


Figure D-2. Floating Signal Generator for providing probe excitation waveform to power amplifier. Constructed, with minor modifications, from XR-2206K Function Generator Kit, available from Exar Integrated Systems, Inc., 750 Palomar avenue, Sunnyvale, CA 94086.

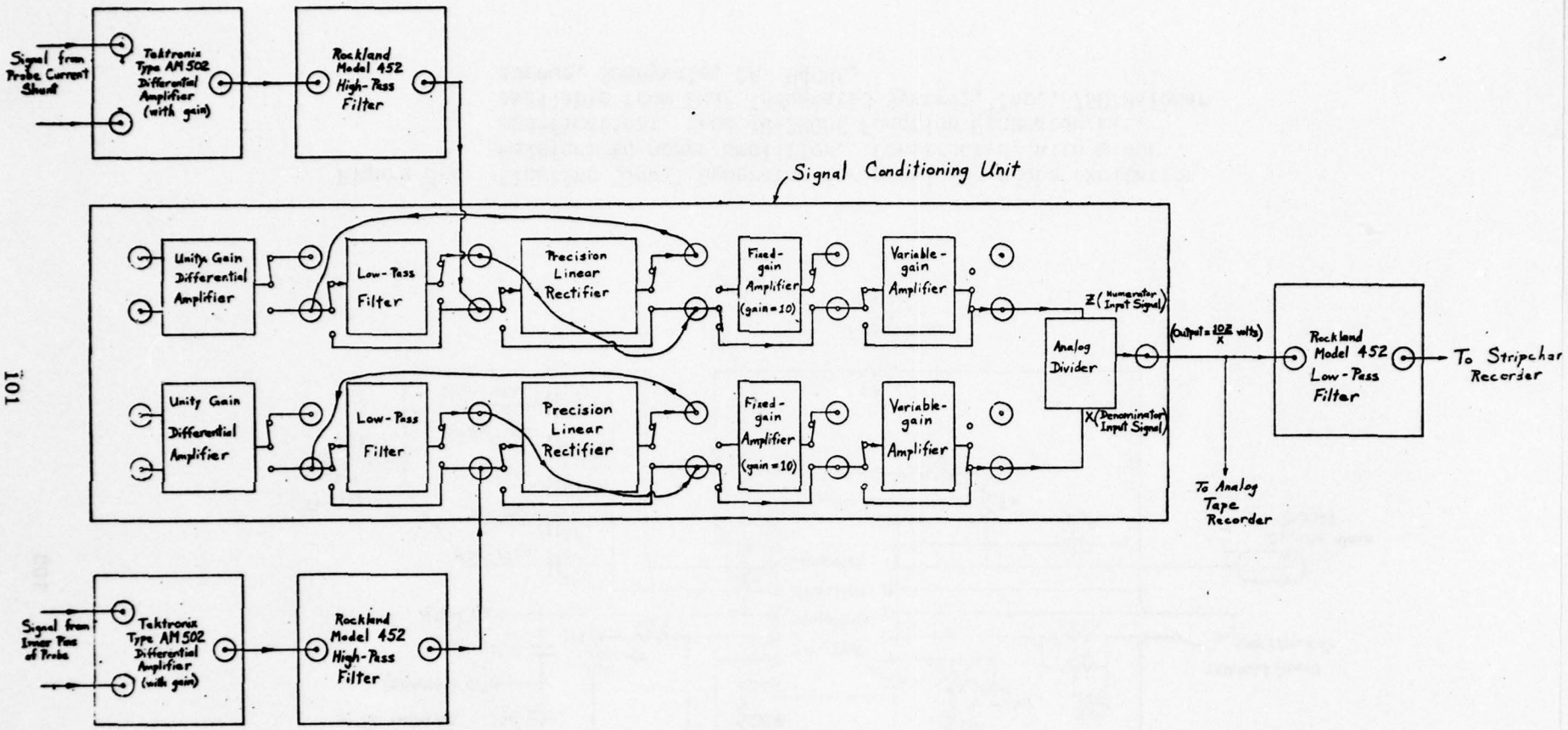


Figure D-3. Schematic drawing of final hookup of Signal Conditioning Unit and external commercial differential amplifiers and filters, to form the electronics configuration of Figure 4.4.

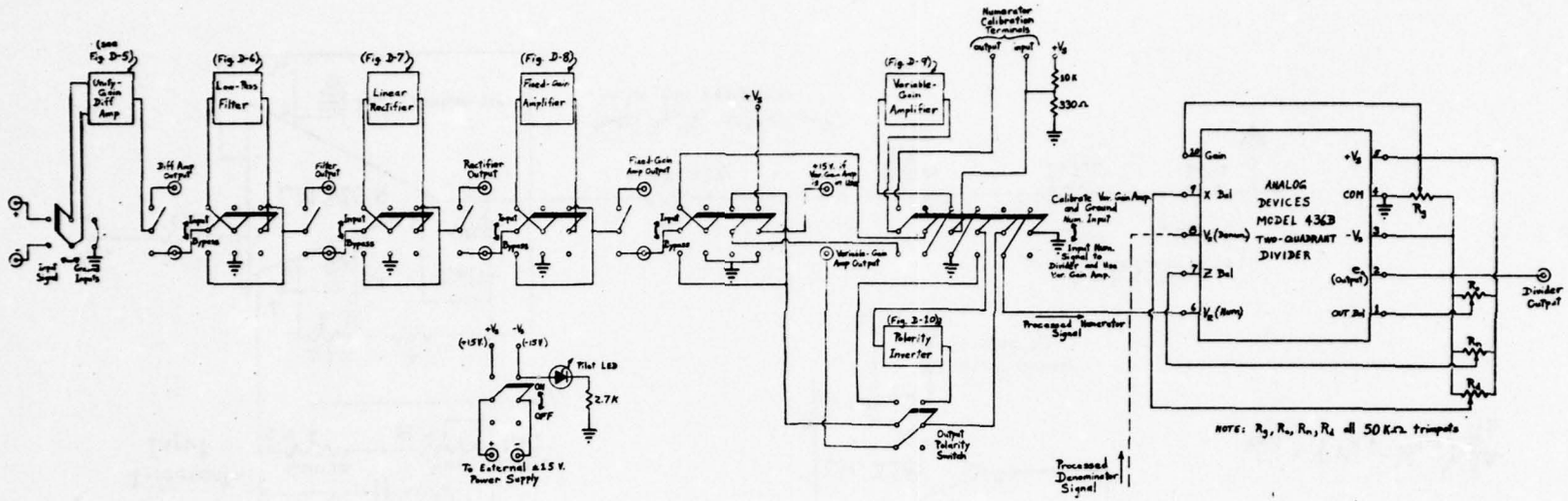


Figure D-4. Chassis Wiring Diagram of Signal Conditioning Unit. The figure shows only the wiring of the numerator signal processing chain; the denominator signal processing chain wiring is identical.

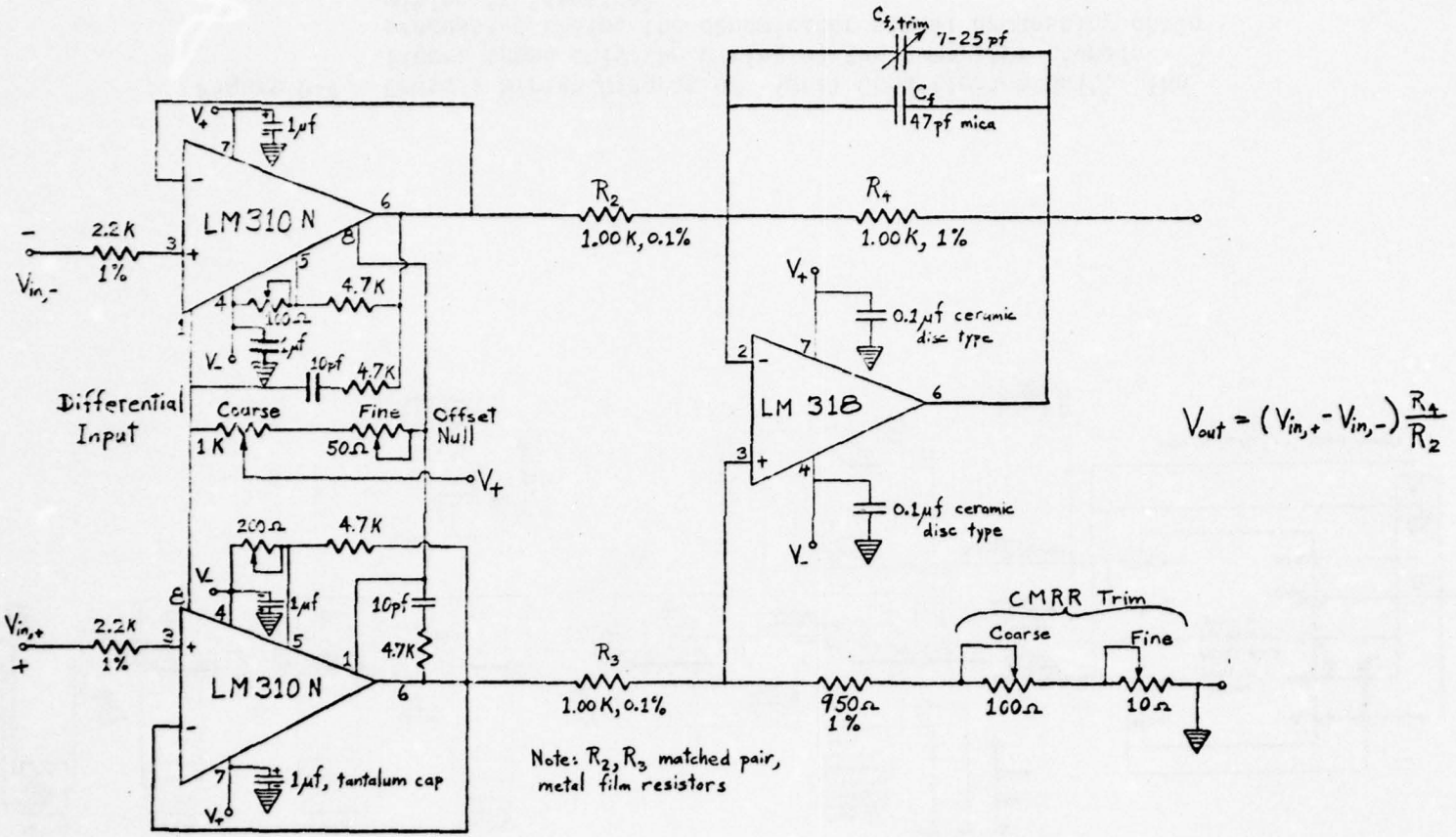


Figure D-5. High Input Impedance Unity-Gain Differential Amplifier Circuit. Nominal specifications: bandwidth ≈ Mhz, CMRR ≈ 50,000 at 10 Hz, common mode range ≈ ± 11 volts, input impedance ≈ 10^{12} ohms, output impedance ≈ 1 ohm, output swing ≈ ± 10 volts.

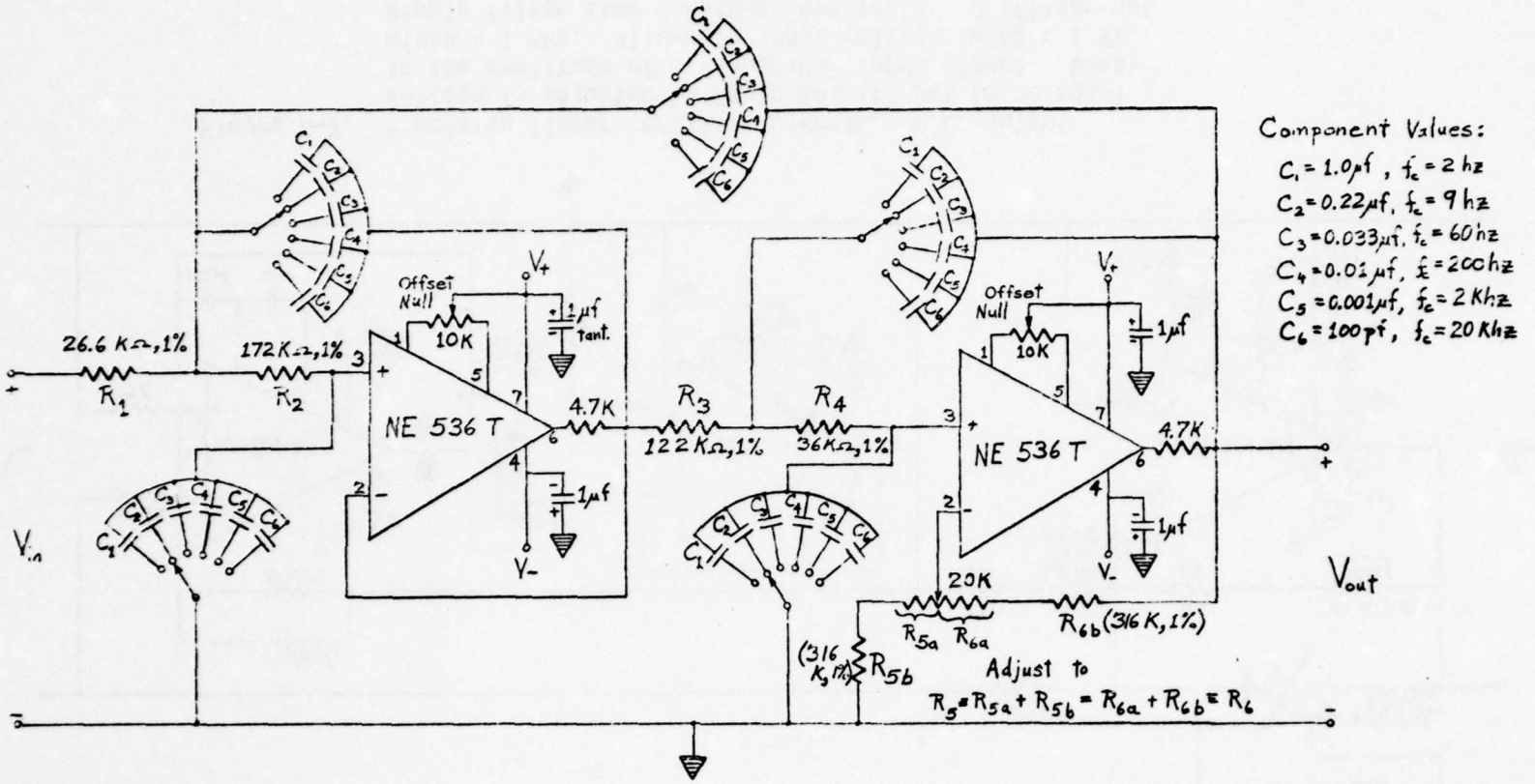


Figure D-6. Low-Pass Filter Circuit. Filter type is multiple feedback fourth-order, with Butterworth (-80 db/decade rolloff) response. f_c = -3 db cutoff frequency. Gain = $1 + R_6/R_5$ (=2.0 for values shown).

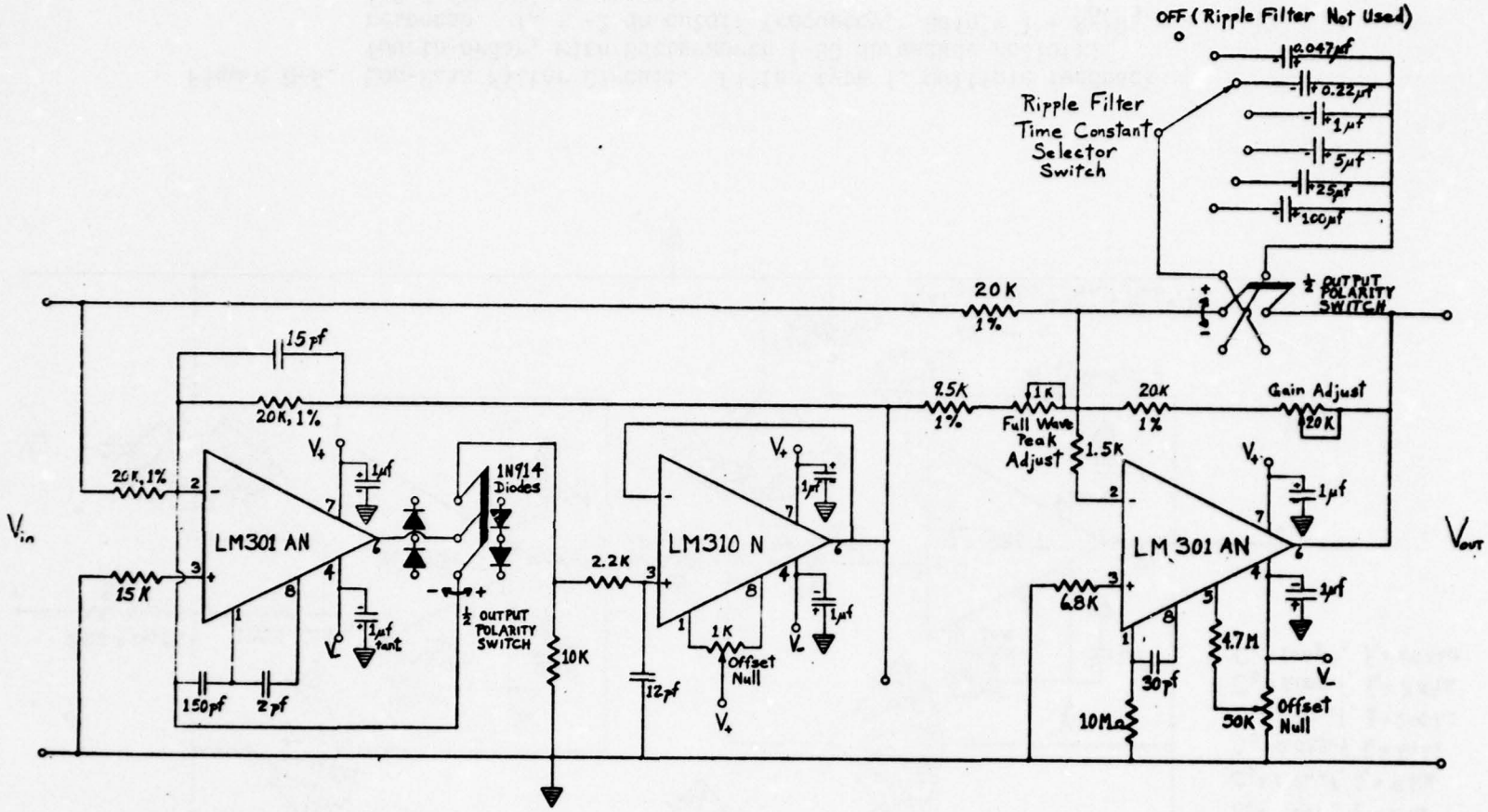


Figure D-7. Precision linear rectifier circuit. D.C. output voltage is adjusted by "gain adjust" pot to be equal to the amplitude of a sinusoidal input signal. Bandwidth ≈ 1 Mhz. Allowable input voltage swing ≈ ± 9V. Ripple filter time constants available: 0 (filter not used--in this case output is full wave rectified waveform), 1 msec, 5 msec, 20 msec, 100 msec, 0.5 sec, and 2 sec.

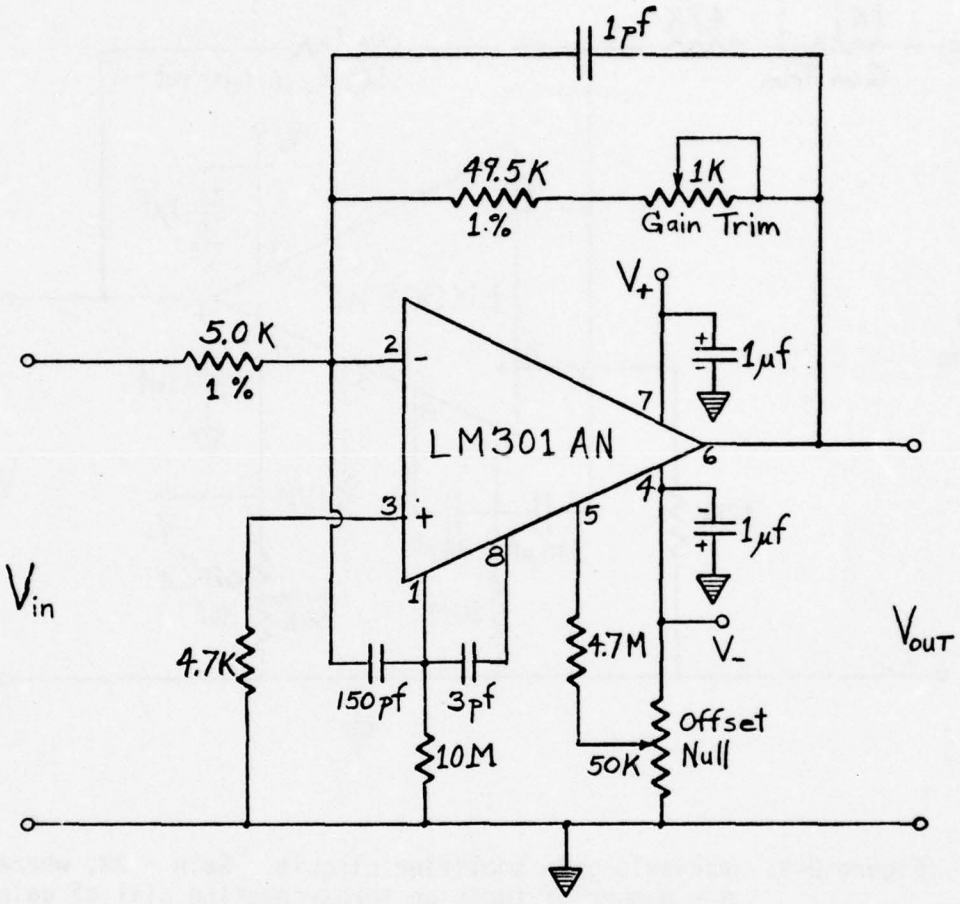


Figure D-8. Fixed-gain amplifier circuit. Gain = 10.0, D.C. to 100 Khz, output voltage swing = ± 14V.

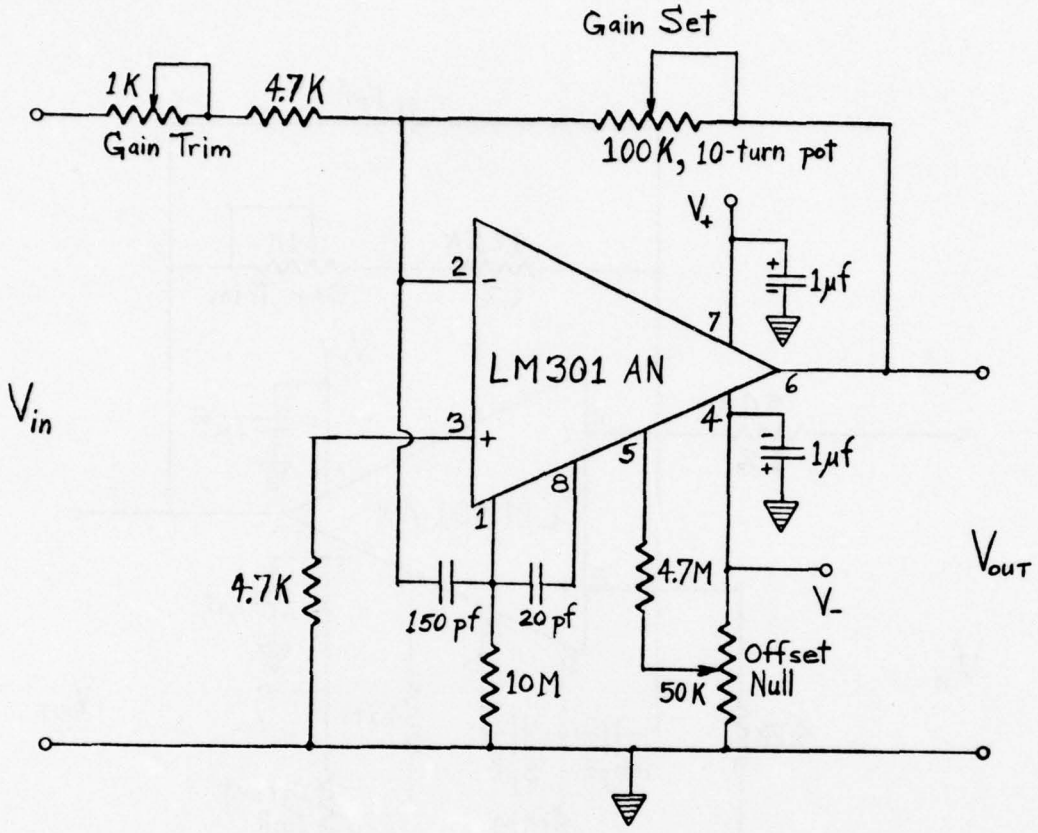


Figure D-9. Variable-gain amplifier circuit. Gain = 2N, where N = number of turns on turns-counting dial of gain set potentiometer (gain variable from 0.1 to 20), bandwidth D.C. to approximately 3 Khz.

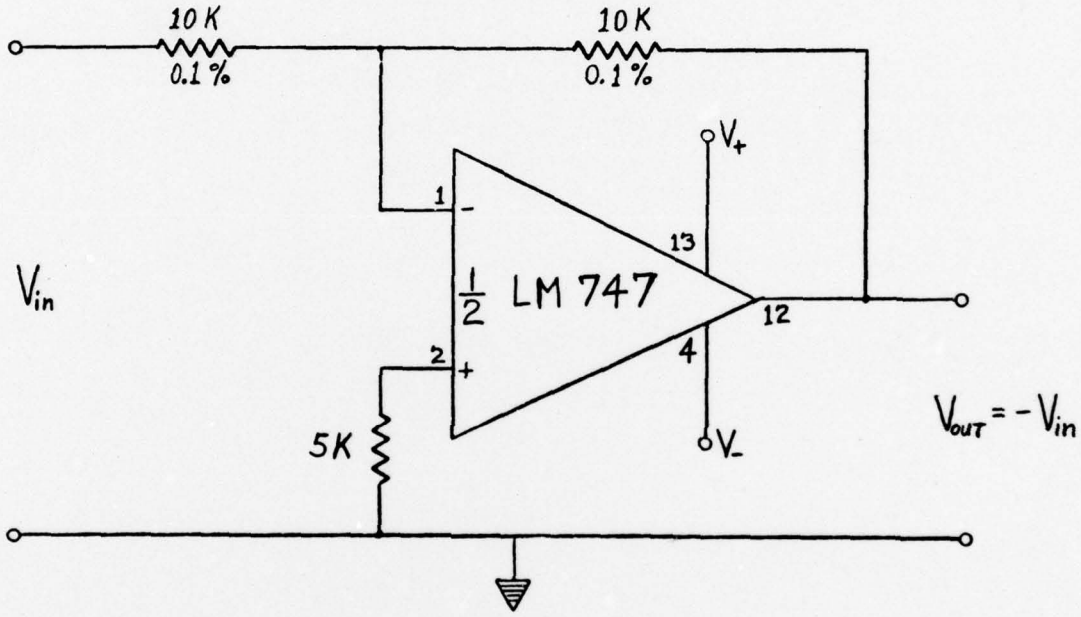


Figure D-10. Polarity inverter circuit (inverting amplifier with unity gain).

Appendix E

PRESERVATION OF LOW-FREQUENCY CONDUCTIVITY FLUCTUATIONS

The argument to be presented here is intended to demonstrate that the variations in slope of i-δV characteristics such as these presented in Figure 4.2, obtained as explained in Section 4.1 with the high-pass filter setup of Figure 4.1, are in fact directly proportional to the electrical conductivity fluctuations, even though the latter may occur at frequencies far below the cutoff frequencies of the filters.

To begin with, we return to the analysis of Section 1.3 and write down expressions for the instantaneous current $i(t)$ and inner pin voltage difference $\delta V_{inner}(t)$. Referring to the notation in Figure 1.2 and applying Kirchoff's law around the complete circuit, we obtain

$$V_{applied} - i R_{sh} - \Delta V_{WF,3} + \Delta V_{sheath,3} - k_{31}\rho i$$

$$-k_{24}\rho i - \Delta V_{sheath,4} + \Delta V_{WF,4} = 0 \quad ,$$

which, upon rearrangement, may be written

$$i(t) = \frac{V_{applied}(t) - \Delta V_{anode-cathode}(t)}{R_{sh} + k_{tot}\,\rho(t)} \quad . \qquad \text{(E-1)}$$

In equation (E-1) $\rho(t)$ is the plasma's resistivity, and $\Delta V_{anode-cathode}$ and k_{tot} are defined as follows:

$$\Delta V_{anode-cathode} \equiv (\Delta V_{WF,3} - \Delta V_{WF,4}) - (\Delta V_{sheath,3} - \Delta V_{sheath,4}) \qquad \text{(E-2)}$$

and

$$k_{tot} \equiv k_{31} + k_p + k_{24}. \qquad \text{(E-3)}$$

Here k_{tot} is constant in time (since it is a function of the geometry of the probe), but $\Delta V_{anode-cathode}$ is a time-varying quantity analagous to δV_{offset}. In addition to (E-1) we have directly from equation (1.3) that

$$\delta V_{inner} = k_p \rho\, i + \delta V_{offset},$$

which becomes, after substitition of the result (E-1) for i,

$$\delta V_{inner}(t) = \delta V_{offset}(t) + k_p \rho(t)\left[\frac{V_{applied}(t) - \Delta V_{anode-cathode}(t)}{R_{sh} + k_{tot} \rho(t)}\right]. \quad \text{(E-4)}$$

Now we consider the outcome of passing the i and δV_{inner} signals given by (E-1) and (E-4) through the high-pass filters shown in Figure 4.1. The transfer function of these filters is represented schematically in Figure E-1, in which the relative magnitudes of the relevant frequencies is indicated on the frequency axis. From this figure we see that only the "fast-varying" signals whose frequencies are close to f_s (typically 20 kHz) or greater will be transmitted by the filter. Keeping in mind that the quantities $\Delta V_{anode-cathode}(t)$, $\delta V_{offset}(t)$ and $\rho(t)$ are "slowly-varying," at least relative to $V_{applied}(t)$, we can assert (and could demonstrate more formally using Fourier series) that the output signals will contain only those terms in which $V_{applied}(t)$ is a factor, i.e.,

$$i(t)_{filtered} = \frac{V_{applied}(t)}{R_{sh} + k_{tot}\rho(t)} , \quad \text{(E-5)}$$

and

$$\delta V_{\substack{inner \\ filtered}}(t) = k_p \rho(t) \left[\frac{V_{applied}(t)}{R_{sh} + k_{tot}\rho(t)}\right] . \quad \text{(E-6)}$$

Substituting (E-5) into (E-6), and replacing the resistivity $\rho(t)$ by the inverse of the conductivity $\sigma(t)^{-1}$, we obtain

$$i_{filtered}(t) = \frac{\sigma(t)}{k_p} \delta V_{inner,filtered}(t) , \quad \text{(E-7)}$$

which shows, as asserted above, that the fluctuating slope of the i-δV characteristics (obtained after high-pass filtering as in Figure 4.1) is proportional to $\sigma(t)$.

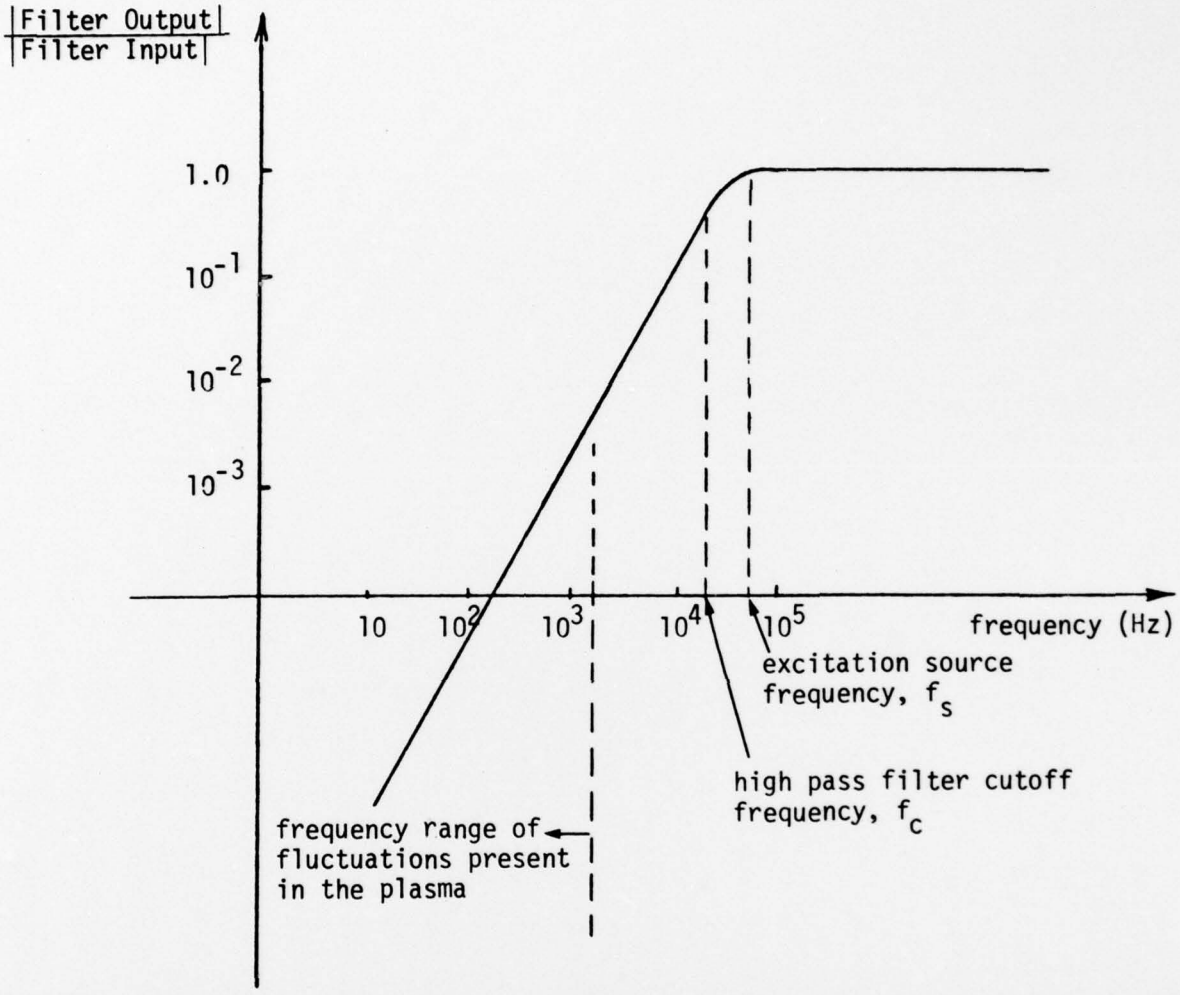


Figure E-1. Approximate transfer function of high pass filters used in 4-pin probe signal processing.

Appendix F

ESTIMATION OF POSSIBLE DECREASES IN CONDUCTIVITY ALONG THE NOZZLE

One of the major experimental results of the present research was a measured decrease of around 50% in the electrical conductivity indicated by a mobile 4-pin probe as the probe was moved along the axis of the subsonic nozzle from the upstream, low-velocity region (Station 1) to the downstream, high-velocity region (Station 2). We discuss in this appendix to what extent the "true" local conductivity may have changed between these two stations due to naturally occurring processes in the plasma.

To begin the discussion, we review the known facts about the state of the gas at station 1 (in the plenum region). During the experiment which yielded the results of Figure 5.3, the tungsten-rhenium thermocouple in the plenum core indicated a junction temperature of about 1700 K. Using various estimates of the radiation correction to this thermocouple reading, we arrive at the result that the heavy gas temperature Tg lies approximately in the range of 1900 K to 2100 K. The electrical conductivity indicated by both the fixed plenum probe and the mobile probe at the low-velocity station 1 was 13 ± 1 mho/m. From calculations of electron transport properties by Brown (specifically, Appendix 2.4 of Reference 6) we can then infer that $N_e \simeq 4.3 \times 10^{12}$ cm^{-3} and the collision frequency $\bar{\nu}_{eH}$ is approximately 9.3×10^{9} sec^{-1} ($\bar{\nu}_{eH}$ is insensitive to T_e over the range 1400 K to 2200 K).

We now wish to know by how much σ (or N_e, which is directly proportional to σ in our case) might change as the gas flows down the nozzle. In general, this is a difficult problem. To the extent that the electron gas is only weakly coupled to the heavy particle gas, one could in principle answer this question by solving simultaneously suitable forms of the electron energy equation and the electron continuity equation, which constitute a pair of coupled, first-order differential equations for N_e and T_e as functions of time. We do not propose such a calculation here. Rather, we ask what would be the possible limiting cases if such detailed calculations were carried out.

One possible limiting case (which we label "Case A") would be that in which local thermodynamic equilibrium (i.e. $T_e = T_g$) is maintained throughout the flow. In this case we would need to examine mechanism leading to decreases in T_g, and then relate the magnitudes of such decreases ΔT to changes

$$\frac{\Delta N_e}{N_e} = \frac{\Delta\sigma}{\sigma}$$

in N_e and σ via the Saha equilibrium relationship between N_e and T_e.

Another possibility (which we call "Case B") would be that Saha equilibrium is maintained (in the sense that N_e and T_e would be related through the Saha equation) at each point in the flow, but that $T_e \neq T_g$ (in fact T_e would be less than T_g for our experimental conditions). In this case it would be necessary to examine mechanisms leading to decreases in T_e, such as radiation escape from the plasma, and to compute the corresponding changes in σ from the Saha equation. It is easy to show that the relationship between the relative fractional changes in σ and T_e in either of these two cases is

$$\frac{d\sigma}{\sigma} = \frac{dN_e}{Ne} = \left(\frac{3}{4} + \frac{\epsilon_i}{2kT}\right)\frac{dT}{T} \quad , \qquad \text{(F-1)}$$

where ϵ_i is the seed ionization potential and T is either T_e or T_g, whichever is applicable.

At the other extreme ("Case C") lies the possibility that the electron density (and hence the conductivity) is essentially frozen at its initial value. This condition could occur if the electron-ion recombination time (τ_{recomb}) were much greater than the flow time of the plasma down the nozzle. In this case, any changes in T_g or T_e which might be simultaneously taking place would be irrelevant as far as estimating changes in σ is concerned, since σ would be essentially constant down the nozzle.

We consider first this latter possibility. The time required for a fluid element to flow from station 1 to station 2 in these experiments was determined from the relation

$$\tau_{flow} = \frac{1}{U_{max}} \int_1^2 \left(\frac{U}{U_{max}}\right)^{-1} dz.$$

Using Figure C-2 to provide the measured profile of U/U_{max} as a function of z, and carrying out the integration graphically, we obtained $\tau_{flow} \simeq 1.37 \times 10^{-3}$ sec.

To estimate $\tau_{recomb.}$ we write the rate of change of N_e due to electron-ion recombination as

$$\frac{dN_e}{dt} = -\alpha N_e^2 \ , \qquad \text{(F-2)}$$

and for the recombination coefficient α we may employ the Hinnov and Hirschberg formula (see Reference [8], Chapter IX, Section 4)

$$\alpha = 3.4 \times 10^{-22} N_e \left(\frac{T_e}{1000}\right)^{-9/2} \ cm^3/sec. \qquad \text{(F-3)}$$

Here N_e is expressed in cm^{-3} and T_e in ^oK. Substituting (F-3) into (F-2) leads to a differential equation which may be integrated between $t=0$ and $t=\tau$ if we assume T_e to remain constant or change slowly. The result is

$$\frac{1}{2}\left[\frac{1}{N_e^2(\tau)} - \frac{1}{N_e^2(0)}\right] = 3.4 \times 10^{-22} \left(\frac{T_e}{1000}\right)^{-9/2} \tau \ . \qquad \text{(F-4)}$$

If we somewhat arbitrarily define a characteristic recombination time τ_{recomb} as the time necessary for N_e to decrease to one half of its initial value, we obtain from (F-4) that

$$\tau_{recomb} = \frac{3}{2} \frac{\left(\frac{T_e}{1000}\right)^{9/2}}{\left[3.4 \times 10^{-22}\right] N_e^2(0)} \ . \qquad \text{(F-5)}$$

The initial N_e was (as previously noted) 4.3×10^{12} cm^{-3}. There was no direct measure of T_e, so we use the value $T_e \simeq 1650$ K, arrived at as explained below in a calculation taking radiation escape into account. Substituting these values of N_e and T_e into (F-5) yields the result

$$\tau_{recomb} \simeq 2.27 \times 10^{-3} \text{ sec.}$$

Comparing the two characteristic times we find that $\tau_{recomb}/\tau_{flow} \simeq 1.66$, or roughly that $\tau_{recomb} \geqslant \tau_{flow}$. If it had turned out that $\tau_{recomb} >> \tau_{flow}$, one would be assured of frozen flow (Case C), while if we had found $\tau_{recomb} << \tau_{flow}$, we could confidently assume equilibrium conditions (Case A or Case B) to hold. What seems likely, therefore, is that N_e (and σ) is partially frozen--decreasing somewhat as the gas travels down the nozzle, but less than it would decrease if equilibrium were maintained. The estimates of conductivity changes which are made below assuming either of the equilibrium situations, Case A and Case B, may thus be regarded as upper bounds on the actual decrease in σ.

Before proceeding to such calculations, we remark that the notion that the conductivity may have been frozen, at least partially, appears to be supported by the experimental evidence of Cool and Zukoski [15]. Under similar experimental conditions (relatively slowly moving, potassium-seeded argon heated to 2000 K in an arcjet) they observed (see especially their Figure 4) that for low applied current densities the conductivity leveled off at a value approximately corresponding to the equilibrium conductivity at the gas temperature. They also concluded that for $J \gtrsim 0.3$ amp/cm^2 the approximate "steady state" form of the electron energy equation,

$$\sigma E^2 = J^2/\sigma = \dot{\Omega} + \dot{R} \quad , \tag{F-6}$$

combined with the Saha equation at the electron temperature, offers an accurate way of predicting the electrical conductivity. For low values of J, however, (F-6) appears (when compared to the data of Cool and Zukoski) to overestimate the effect of radiation in the electron energy balance. This result would be in accord with the notion that a frozen electron density was being observed as $J \to 0$, in which event the use of the Saha equation would not be justified.

We now proceed to Case B. In the present experiments $J = 0$, so that the approximate energy balance equation

$$-\dot{\Omega} = \sum_h \frac{2m_e}{m_h} \bar{\nu}_{eh} N_e \frac{3}{2} k\left(T_g - T_e\right) = \dot{R} \tag{F-7}$$

may be used to estimate the change in T_e between the two stations as a result of radiation escape. The calculation procedure is summarized in what follows. Since N_e is uniquely determined as a function of T_e by the Saha equation (which we are now assuming to be applicable), and since T_g changes only very slightly down the nozzle (a fact which will be shown to be true later), we may treat T_g as a constant and conclude that the left-hand side of (F-7) is a function only of T_e, and may be displayed graphically as such. The right-hand side, $\dot{R}$, which represents the radiated energy lost from the gas per second per unit volume, may be estimated using the results of McGregor [11] for resonance radiation escape from potassium-seeded argon. From page 148 of [11],

$$\dot{R} = \dot{R}' + n_1 \dot{R}'' \quad , \tag{F-8}$$

where n_1 is the ground level number density of potassium atoms and $\dot{R}'$ and $\dot{R}''$ are coefficients calculated by McGregor and tabulated in Table A.2 of [11]. In order to "enter" this table, the input parameters T_e, N_e, and β must be specified. Since we are assuming Saha equilibrium holds, N_e is determined once T_e is specified. Here β is the radiation escape parameter whose definition and calculation are presented in Appendix H of [11], which gives the formula

$$\beta(4P\text{-}4S) = (1.374 \times 10^{-2}) \left(\frac{T_e}{1000}\right)^{1/4} \left(\frac{10^{-3}}{n_k/n_A}\right)^{1/2} \left(\frac{0.5}{r(cm)}\right)^{1/2} \quad . \tag{F-9}$$

Here r is the radius of the radiating plasma, which is assumed to be a uniform, infinitely long cylinder.

The procedure for determining T_e at, say, station 1 is thus as follows: First one picks a gas temperature T_g and plots a graph of the left-hand side $(-\dot{\Omega})$ of (F-7) as a function of T_e. Then, using the nozzle radius r_1 at station 1 in formula (F-9), one computes the escape parameter β_1 at station 1. Next, using this β_1 and some assumed value for T_e (and the corresponding "Saha" value of N_e); one enters McGregor's Table A.2 (liberally interpolating as necessary) and finds $\dot{R}'$ and $\dot{R}''$, and finally computes $\dot{R}$ from (F-8). This process is repeated for several more

assumed values of T_e until enough points are obtained to plot $\dot{R} = \dot{R}(T_e, r_1)$ as a function of T_e on the same graph on which $-\dot{\Omega}$ is plotted. The abscissa of the point of intersection of the two resulting curves then is the value of T_e which satisfies the energy balance relation (F-7) at station 1. When this process was carried out using $T_g = 2000$ K and the remaining parameters appropriate to our plasma conditions, the value $T_{e,1} \simeq 1646 \pm 2$ K was obtained. Then the entire process was repeated, changing only the radius r to be that at station 2, with the result that $T_{e,2} \simeq 1632 \pm 2$ K. Substituting $\Delta T_e = T_{e,1} - T_{e,2} \simeq 14$ K for dT_e into (F-1), and using the value $T_e \simeq 1640$ K, we obtain a maximum percentage reduction in σ of $d\sigma/\sigma \simeq 14\%$, considerably less than the observed 50% drop in indicated conductivity.

Finally we consider Case A, in which it is to be assumed that $T_e = T_g$ all along the nozzle. One mechanism leading to a decrease in T_g is the gasdynamic cooling which occurs as the thermal energy of the gas is shifted to directed kinetic energy as the flow accelerates. The estimate of the magnitude of this effect is based on the well-known formula (see, for example, Reference 10) for the radio of the stagnation temperature, T_o, to the static temperature T in the adiabatic flow of a perfect gas

$$\frac{T_o}{T} = 1 + \frac{k-1}{2} M^2 \qquad \text{(F-10)}$$

where $k = c_p/c_v$ and M is the Mach number. Using $k = 5/3$ for argon, plus the maximum Mach number M=0.095 obtained in these experiments, we obtain from (F-10) the result that

$$\frac{T_o - T}{T_o} = \frac{\Delta T}{T_o} \simeq 0.003,$$

which when substituted into (F-1) together with $T_g = 2000$ K yields $d\sigma/\sigma \simeq 4\%$, again well below the observed decrease in indicated conductivity. The fact that $\Delta T \cong 0.003\ T_o \simeq 6$ K justifies our assumption in the previous paragraph that T_g is essentially constant down the nozzle.

Still another possible mechanism for lowering T_g is radiation escape, since the random thermal energy of the gas must ultimately be the source of this energy. We may estimate the gas temperature drop which would be caused

by such a process by equating the internal energy drop per second in a thin slab of gas at some location z to the energy loss rate by radiation from that slab:

$$\dot{m}de = \dot{R}\, A(z)\, dz \quad .$$

Here $\dot{m}$ is the mass flow rate of argon, e is the internal energy per unit mass, and $A(z)$ is the cross-sectional area of the nozzle at axial position z. Writing $de = (3/2\ k/m_A)\ dT_g$; where k is Boltzmann's constant and m_A the atomic mass of argon, and integrating from $z = 0$ to $z = L$ (the length of the nozzle) yields

$$T_g\ (0) - T_g(L) = \Delta T_g = \frac{\dot{R}\ m_A}{\dot{m}\ \frac{3}{2}k} \int_o^L A(z)\ dz \ .$$

By defining an averaged cross-sectional area $\bar{A}$ such that

$$\bar{A}\ L = \int_o^L A(z)\ dz \ ,$$

the previous result becomes

$$\Delta T_g = \frac{\dot{R}\ m_A\ \bar{A}\ L}{\dot{m}\ \frac{3}{2}\ k} \quad . \qquad \text{(F-11)}$$

Using McGregor's results as described above to estimate $\dot{R}$, and inserting appropriate estimates of $\bar{A}$, L, $\dot{m}$ in (F-11), we have found that for the temperature ranges of our experiments, ΔT_g from equation (F-11) is less than 2 K. The conductivity drop caused by this mechanism is therefore also negligible.

References

1. Hower, N. L., and M. Mitchner, "Nonlinear Calculations of the Effective Conductivity of Inhomogeneous MHD Generator Plasmas," Sixth International Conference on Magnetohydrodynamic Electrical Power Generation, Washington, D. C., June 1975, Vol. IV, pp. 217-236. (This material also appears, with some additional results, in Interim Scientific Report on Nonequilibrium Phenomena in Flowing Plasmas and at High Magnetic Fields, April 1975, prepared for Air Force Office of Scientific Research, submitted by R. H. Eustis, C. H. Kruger, M. Mitchner, R. K. Hanson, High-Temperature Gasdynamics Laboratory, Mechanical Engineering Department, Stanford University.)
2. Self, S. A., and C. H. Kruger, "Diagnostic Methods in Combustion MHD Flows," AIAA Paper No. 76-310, AIAA 9th Fluid and Plasma Dynamics Conference, San Diego, CA., July, 1976.
3. Vendell, E. W., "Free Jet Electrical Conductivity Profiles of a Seeded MHD Combustion Plasma," 15th Symposium on Engineering Aspects of MHD, Philadelphia, May 1976, pp. IX.5.1-IX.5.6.
4. Gaponov, I. M., L. P. Poberezhsky, and Yu. G. Chernov, "Study of the Electric Conductivity of Plasma of Combustion Products with Seeding in the U-02-MHD Generator Channel and on a Laboratory Installation," Combustion and Flame 23, 29 (1974).
5. Clements, R. M., "Some Measurements of Ion Current to a Spherical Probe in an Atmospheric Pressure Combustion MHD Plasma," Combustion and Flame 25, 393 (1975).
6. Brown, Robert T., "Electron Temperature and Number Density Measurements in a Nonequilibrium Plasma Boundary Layer," SU-IPR Report No. 350, Institute for Plasma Research, Stanford University, January, 1970.
7. Kurz, J. L., "Experimental Electrode Current Distributions in MHD Channels," SUIPR Report No. 230, Institute for Plasma Research, Stanfore University, April 1968.
8. Mitchner, M., and C. H. Kruger, Partially Ionized Gases, John Wiley and Sons, 1973.
9. Bendat, J. S., and A. G. Piersol, Random Data: Analysis and Measurement Procedures, John Wiley and Sons, 1971.

References

10. Shapirio, Ascher H., The Dynamics and Thermodynamics of Compressible Fluid Flow, The Ronald Press Co., New York, 1953, p. 80.
11. McGregor, Douglas David, "Electronic Non-equilibrium in a Supersonic Expansion of Ionized Gas," SU-IPR Report No. 474, Institute for Plasma Research, Stanford University, July 1972.
12. Cobine, James Dillon, Gaseous Conductors: Theory and Engineering Applications, Dover Publications, Inc., New York, 1958.
13. Jones, Grinnell and Dorothy M. Bollinger, "The Measurement of the Conductance of Electrolytes. VII on Platinization," American Chemical Society Journal, 57, p. 280 (1935).
14. Handbook of Chemistry and Physics, 43rd edition (1961-62), Chemical Rubber Publishing Co., Cleveland, p. 2644.
15. Cool, T.A. and E. E. Zukoski, "Recombination, Ionization, and Non-equilibrium Electrical Conductivity in Seeded Plasmas," Physics of Fluids, 9, No. 4 (1966), p. 780.